Structure and dynamics of liquid helium systems and their interaction with atomic dopants and free electrons

David Mateo Valderrama

Structure and dynamics of liquid helium systems and their interaction with atomic dopants and free electrons

by

David Mateo Valderrama

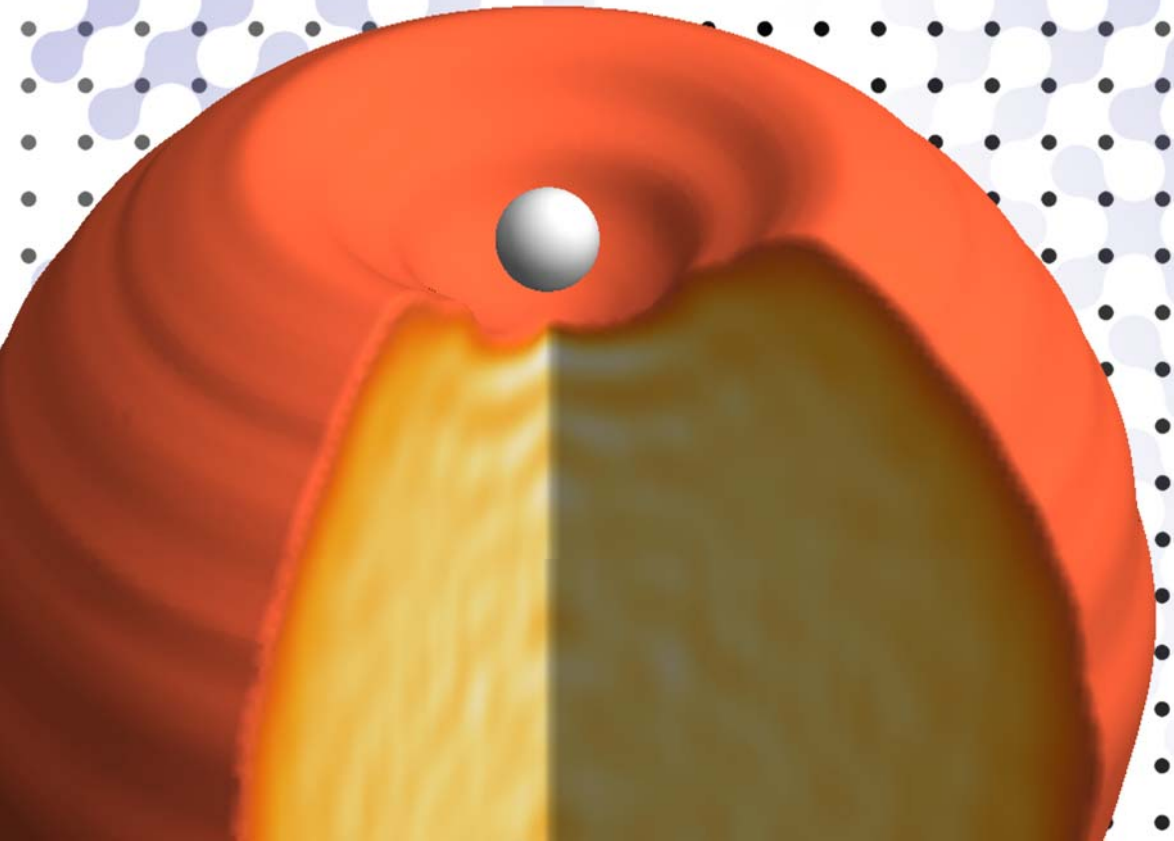

Structure and dynamics of liquid helium systems and their interaction with atomic dopants and free electrons

by

David Mateo Valderrama

Supervisor: Dr. Manuel Barranco Gómez
Tutor: Dr. Martí Pi Pericay

Thesis submitted for the degree of Doctor of Philosophy under the Physics PhD program at the University of Barcelona.
March 2013

Tesis presentada para obtener el grado de Doctor en el programa de doctorado de Física de la Universidad de Barcelona.
Marzo de 2013

Resumen

Contexto

El helio es la única sustancia que permanece líquida a temperatura cero. Esta curiosa característica es una clara manifestación macroscópica de la naturaleza cuántica de la materia. El helio es el segundo elemento más ligero y su estructura de capa cerrada es responsable de la débil atracción entre átomos de He. Estas dos propiedades son la causa de que el helio tenga una energía de punto cero suficientemente grande como para evitar la solidificación, incluso a temperatura estrictamente cero. La energía del punto cero –también conocida como movimiento del punto cero– es la energía asociada a la localización de la distribución de probabilidad de un sistema. La existencia de esta energía es una predicción de la mecánica cuántica sin equivalente clásico que desempeña el papel de energía cinética incluso cuando no hay "movimiento" en el sentido clásico. La naturaleza cuántica del He se manifiesta no solo impidiendo su solidificación sino también causando una transición de segundo orden cuando la temperatura se reduce por debajo de los 2.18 grados Kelvin de un estado líquido normal (He I) a un estado *superfluido* (He II); un nuevo estado de la materia en el que la ausencia de viscosidad permite al helio fluir libremente (sin disipación) cuando se desplaza a velocidades por debajo de cierto valor límite.[1]

El helio aparece tanto en forma de líquido homogéneo como en forma de gotas. Las gotas pueden estar formadas por cualquiera de los dos isótopos estables del helio, ^{3}He y ^{4}He, o de una mezcla de ambos. A bajas temperaturas, una gota mixta de ^{3}He–^{4}He es un agregado estructurado con ^{4}He en su núcleo y ^{3}He en su capa externa. Una propiedad interesante de estas gotas es que pueden ser dopadas con impurezas de forma relativamente fácil. El estudio espectroscópico de estas impurezas permite analizar el entorno de helio que las rodea. [2–7] Dependiendo de la impureza, ésta se situará bien en el centro de la gota, en la superficie, o en la interficie ^{3}He–^{4}He.[8] La estructura de gotas de ^{3}He, ^{4}He y, en menor medida, ^{3}He–^{4}He alrededor de impurezas atómicas o electrones libres ha sido estudiada tanto a nivel teórico como experimental.

La dinámica de estos sistemas se ha resistido a una exploración teórica durante muchos años. Uno podría argumentar que, dado los pocos experimentos llevados a cabo sobre la respuesta del helio en la escala del picosegundo, una descripción precisa de la dinámica es una cuestión puramente académica de poca relevancia para la comunidad

experimental. Sin embargo, diversos experimentos como por ejemplo la observación de la desaparición de burbujas electrónicas excitadas[9] por el Prof. Maris o la medición de la velocidad de desorción de átomos de Ag dentro de gotas[10] del Prof. Drabbels muestran que una descripción teórica completa y precisa del proceso dinámico que subyace a estas experiencias es fundamental para comprender los resultados.

Resultados

En esta tesis se presenta una colección de cuatro artículos publicados y un manuscrito aún no publicado, todos ellos en el campo de la física de bajas temperaturas y fluidos cuánticos. Cada uno de ellos reporta un paso adelante en la descripción teórica de los sistemas de helio por medio de la teoría del funcional de la densidad.

Los primeros dos artículos [11, 12] están clasificados como "estructura" ya que tratan cuestiones relacionadas con la descripción del estado fundamental de complejos de helio dopados con impurezas atómicas. En ellos hemos calculado la estructura y determinado su efecto sobre el espectro de absorción dipolar del Na en agregados de ^{3}He–^{4}He y del Mg en el líquido homogéneo e isotópicamente mezclado. Para el caso de Na en gotas se ha encontrado que, a pesar de necesitar una gran cantidad de ^{3}He para que la capa exterior de la gota sature, el espectro de la impureza es muy insensible a la composición isotópica y rápidamente satura al valor que toma en las gotas de ^{3}He puras. Para Mg en el líquido mezclado, la presencia de ^{3}He induce cambios en el espectro mucho más pequeños que su anchura característica, por lo que se ha encontrado que el efecto general de la composición isotópica de la mezcla en la espectroscopía es mínima.

Hemos explorado también los límites del funcional de la densidad para un número pequeño de átomos de helio interactuando con una molécula lineal de sulfuro de carbonilo (OCS). Para ello hemos implementado un esquema de Kohn-Sham para el ^{3}He y hemos obtenido la estructura de agregados OCS@^{3}He$_N$ para un número de átomos N hasta 40. Hemos comparado los resultados de los agregados de ^{4}He con el mismo número de átomos y hemos encontrado que la alta anisotropía de la molécula de OCS magnifica los efectos de las diferentes estadísticas de cada isótopo. Nuestra estimación de los momentos de inercia de estos agregados es consistente con la interpretación de los datos experimentales[13] que sugieren una estructura de 11 átomos de helio rotando solidariamente con la molécula de OCS.

Los siguientes tres trabajos [10, 14, 15], clasificados como "dinámica", describen la evolución temporal de ciertos procesos de interés experimental en los sistemas de helio. Mientras que las publicaciones sobre la estructura completan una línea de trabajo bien establecida, las de esta sección abren un nuevo frente de exploración teórica sobre los procesos dinámicos con resolución de picosegundos. En ellos se presenta un procedimiento eficiente para describirlos cuantitativamente mediante una teoría del funcional de la densidad dependiente del tiempo (TDDFT, por sus siglas en inglés) para el helio, acoplado a la dinámica adecuada para la impureza. Cuál es la dinámica "adecuada"

depende de las propiedades de la impureza: para la burbuja electrónica 1P se puede utilizar una descripción puramente mecanocuántica del electrón en una aproximación adiabática, mientras que para la burbuja 2P la aproximación adiabática no es aplicable y se deben acoplar las evoluciones en tiempo real del helio y del electrón. Para una impureza masiva como la Ag una descripción clásica de su movimiento es suficiente, pero el efecto de spin-órbita es lo suficientemente importante como para que el estado electrónico del átomo deba tenerse en cuenta en la dinámica como un grado de libertad cuantizado.

En el caso de las burbujas electrónicas, hemos relacionado la desaparición de las burbujas 1P a altas presiones con la existencia de un camino de relajación no-radiativo que causa la rotura de la burbuja en dos mitades casi esféricas tras haber transcurrido unos 20 picosegundos desde su excitación. Hemos sido capaces de establecer esta relación gracias a que nuestro cálculo predice la "fisión" de la burbuja solo para presiones superiores a 1 bar, que es el mismo umbral observado experimentalmente para la desaparición de las burbujas 1P. [9] Teniendo en cuenta que aumentar la presión en 1 bar aumenta la densidad de saturación del líquido en poco más de un 1 %, la exactitud de este resultado indica que TDDFT contiene la física relevante para describir este tipo de procesos y tiene capacidad de predicción cuantitativa. También hemos encontrado un marcado cambio en el comportamiento del espectro de absorción con resolución temporal de la burbuja 1P dependiendo de si ésta fisiona o no, es decir, dependiendo de la presión del líquido. La observación experimental de este cambio y su determinación podría completar la información obtenida en los experimentos de cavitación y fotoconductividad.

En el caso de la desorción de un átomo de plata tras su fotoexcitación en el interior de una gota de He, nuestros cálculos dinámicos predicen un rango de velocidades para la impureza consistente con la distribución de velocidades experimental. Esta velocidad es el resultado de cuánta energía transfiere la impureza a la gota, lo cual depende de los modos de excitación disponibles para dicha transferencia. Nuestra descripción del líquido solo permite excitaciones colectivas tales como ondas de densidad u oscilaciones de superficie, por lo que la compatibilidad de nuestros resultados con los datos experimentales se puede tomar como una evidencia indirecta de la superfluidez de las nanogotas de helio. Adicionalmente hemos descartado la nucleación vórtices como un posible canal de transferencia de energía en gotas nanoscópicas al no haberlos generado en nuestros cálculos.

Contents

Chapter 1

Introduction

Helium first revealed itself in 1868 as a bright yellow line coming from the Sun. As the unworldly substance it seemed to be, it was named after the Greek word for Sun, *helios*. Fourteen years later its presence on Earth was unraveled by analyzing the spectral lines of the lava on Mount Vesuvius. Before the turn of the century, helium would be captured and isolated for study in several laboratories around Europe. In 1908, Heike Kamerlingh Onnes achieved the liquefaction of helium by cooling it below four degrees Kelvin, but helium would always defy solidification under normal pressure.[16] This seemingly innocent realization marks the start for an exhaustive research which would reveal a new state of matter and surprising new phenomenology in the field of low temperature physics.

Helium is the only substance which remains liquid at zero temperature. This striking feature is a clear and indisputable macroscopic manifestation of the quantum nature of matter. Helium is the second lightest element and its closed shell structure is responsible for the extremely small attraction between He atoms. These two properties cause the helium to have a zero point energy large enough to keep it from solidifying even at strictly zero temperature. The zero point energy –also known as zero point motion– is the energy associated with the localization of the probability distribution of a system on a finite region of space. The existence of this energy is a prediction of Quantum Mechanics with no classical equivalent, and plays the role of a kinetic energy present even when there is no "motion" in the classical sense. The quantum nature of He does not only prevents it from solidifying but also causes a second order phase transition when the temperature is reduced below 2.18 Kelvin from normal liquid state (He I) to a *superfluid* state (He II); a new state of matter in which the absence of viscosity allows it to flow freely (with no dissipation) at velocities below a certain limit.[1]

The superfluid state is a highly correlated state where particle excitations are suppressed in favor of delocalized collective excitations. It is associated with Bose-Einstein condensation, a manifestation of the bosonic nature of helium's most abundant isotope, ^{4}He. Helium has a second stable isotope, ^{3}He, which has spin 1/2 and therefore follows fermionic statistics. The different statistics have a critical effect on the macroscopic

properties of the liquid. For example, for ^{3}He one needs to go to much lower temperatures, below 2.6 mK, to find its superfluid state. This state is associated with the condensation of ^{3}He atom pairs, similar to the Cooper pairing of electrons in a superconducting state.[17] Because ^{3}He and ^{4}He are practically identical in all properties but statistics, a thorough comparison of these two substances is particularly interesting to understand the role quantum statistics plays in the behavior of many-body systems.

Helium can appear both as a bulk liquid and as droplets. At low temperatures, a mixed ^{3}He-^{4}He drop is a structured cluster with ^{4}He in its core and ^{3}He in its outer shell. One attractive feature of these drops is that they can be doped with impurities with relative ease for spectroscopic probing of the helium environment.[2–7] Depending on the impurity it will either go to the center of the drop, reside at its surface, or sink down to the ^{3}He–^{4}He interface.[8] The structure of ^{3}He, ^{4}He and, to a lesser extend, ^{3}He–^{4}He mixed droplets and liquids around atomic impurities or free electrons has been studied both in the experimental and theoretical fronts.

The dynamics of these systems, on the other hand, have proven elusive for many years. One may naively argue that, because few experiments are carried out to study the response of helium at the picosecond scale, an accurate dynamical description of helium systems is a purely academic issue of little relevance to the experimental community. However, many experiments such as Prof. Maris' observation of disappearing excited 1P electron bubbles[9] or Prof. Drabbels' measurement of the desorption velocity of Ag atoms inside drops[10] have shown that a complete and accurate theoretical description of the dynamical processes underlying these experiments is fundamental to understand them.

The publications presented in this thesis are split in two chapters: Chapter 2 addresses some problems on the structure of drops and the mixed liquid. The differences between ^{3}He and ^{4}He are studied through the dipole absorption spectrum of Na and Mg impurities and through their effect on the moment of inertia of solvated carbonyl sulfide molecules. Chapter 3 presents the development of an accurate and consistent framework to address time-dependent problems in helium liquids and clusters of some thousand atoms. This methodology is used to help interpret the experiments by Profs. Maris and Drabbels commented above.

1.1 Theoretical description of helium systems

A good theoretical description is essential to fully understand the experimental evidence. Any potential description must take into account the key role of quantum mechanics and the strong He–He correlations.

There are several approaches to a theoretical exploration of the properties of many-body systems. One possibility is to solve numerically the N-body Schrödinger equation by *Quantum Monte Carlo* simulation techniques.[18, 19] These techniques partially

alleviate the prohibitive scaling of computational cost with the number of particles that solving the Schrödinger equation has. These are *ab initio* procedures that give a very detailed description of the groundstate of the system but require humongous amount of computational power to describe systems of experimental interest such as drops with some thousands of atoms. Other *ab initio* techniques include Green's Function, Propagator Methods, Correlated Basis Function or Coupled Cluster Method.[20–22] These methods involve either diagramatic expansions or variations of a trial wavefunction, and are either less suited or just not suited for complex setups like a cluster doped with a strongly interacting impurity.

One alternative to these microscopic approaches is to pursue a phenomenological description of the system by using *Density Functional Theory*. In this approach, all the properties of the liquid are encoded in an energy functional which depends only on the one-body density instead of the complete N-body wavefunction.[23–26] This provides a good scaling with the number of particles while maintaining a wide applicability. The price to pay is the added complexity of finding a realistic energy functional and the limitation of having an hydrodynamic description of the system, with no information on the atoms themselves nor their correlations.

We have chosen the later approach in all the works presented here as its accuracy and efficiency have been proven. Besides, it is the only realistic way of computing real-time dynamics in the picosecond domain for a system of thousands interacting He atoms so far.

1.1.1 Density Functional Theory

Density functional theory is a rigorous formulation of nonrelativistic quantum many-body physics in which the energy of the system is taken as a functional of the one-body density and not the complete N-body wavefunction. The base for this formulation is the demonstration [27] by Hohenberg and Kohn in 1964 that the groundstate properties of a quantum system of interacting particles can be characterized completely by the one-body density through the appropriate energy functional.

Several energy functionals for a system of interacting helium atoms have been developed over the years. The quintessential functional when dealing with inhomogeneous ^{4}He settings is a finite-range functional known as "Orsay-Trento" presented in 1995 by F. Dalfovo et al.[28] The extension to inhomogeneous ^{3}He–^{4}He mixtures made in [29] (which reduces to Orsay-Trento in the absence of ^{3}He) has been the functional of choice for the works presented in this thesis.

With an energy functional at hand, this theory can be easily extended to a Time-Dependent Density Functional Theory (TDDFT). In its simplest implementation, the dynamics of the system is obtained by minimizing the quantum action for the effective

macroscopic wavefunction Ψ,

$$\mathcal{A}[\Psi] = \int dt \left\{ E[\rho] + \int d\vec{r} \frac{\hbar^2}{2m} |\vec{\nabla}\Psi|^2 - i\hbar\Psi^* \frac{\partial}{\partial t}\Psi \right\} ,$$

where Ψ is a complex field whose squared modulus equals the one-body density, $\rho = |\Psi|^2$. This minimization yields a time-dependent Schrödinger-like equation for $\Psi(\vec{r}, t)$ of the form

$$i\hbar \frac{\partial}{\partial t}\Psi(\vec{r}, t) = \left(-\frac{\hbar^2}{2m}\nabla^2 + \frac{\delta E}{\delta \rho(\vec{r}, t)} \right) \Psi(\vec{r}, t) \quad .$$

which can be efficiently solved numerically by generic differential equation methods such as a predictor-corrector algorithm.[30]

In all the problems addressed in this work helium is coupled to an impurity, which may be either an atomic impurity such as Ag or an excess electron trapped in a bubble. This coupling is introduced as a helium-impurity potential also entering in the time evolution equation for the impurity. The power and suitability of TDDFT for the dynamics of liquid helium and droplets becomes apparent since the same formalism has allowed to couple, with only small changes, the helium evolution with an adiabatically evolving wavefunction,[14] a real-time evolving wavefunction,[15] o a moving classical particle with spin-orbit degrees of freedom.[10]

Chapter 2

Structure

2.1 Absorption spectrum of atomic impurities in isotopic mixtures of liquid helium

Resumen (Spanish)

El espectro de absorción de impurezas atómicas en mezclas isotópicas de helio líquido se describe en este trabajo mediante cálculos basados en un formalismo del funcional de la densidad a temperatura cero. Se consideran dos casos: en el primero, el espectro de absorción de átomos de Na ligados a gotas de $^4\mathrm{He}_{1000}$–$^3\mathrm{He}_{N_3}$, con valores de N_3 de 100 a 3000 se presenta como caso de estudio de una impureza que no solvata en gotas de helio. En el segundo, el espectro de absorción de átomos de Mg solvatados en mezclas isotópicas de ^{3}He y ^{4}He se presenta como caso de estudio de impureza disuelta en el líquido uniforme.

Encontramos que el espectro de las impurezas se ve poco afectado por la composición isotópica del entorno, y que depende básicamente de la cantidad de helio que tiene a su alrededor sin importar el isótopo. En el caso de mezclas de líquido uniforme, los resultados se presentan en función de la presión para diferentes valores de concentración de ^{3}He. Los resultados para los líquidos isotópicamente puros de ^{3}He y ^{4}He se comparan con los datos experimentales disponibles en la literatura.

PHYSICAL REVIEW B **83**, 174505 (2011)

Absorption spectrum of atomic impurities in isotopic mixtures of liquid helium

David Mateo, Alberto Hernando, Manuel Barranco, Ricardo Mayol, and Martí Pi
Departament ECM, Facultat de Física, and IN²UB, Universitat de Barcelona, Diagonal 647, 08028 Barcelona, Spain
(Received 7 February 2011; published 6 May 2011)

We theoretically describe the absorption spectrum of atomic impurities in isotopic mixtures of liquid helium within a zero-temperature density functional approach. Two situations are considered. In the first one, the absorption spectrum of Na atoms attached to $^4He_{1000}$-$^3He_{N_3}$ droplets with N_3 values from 100 to 3000 is presented as a case study of an impurity that does not dissolve into helium droplets. In the second one, the absorption spectrum of Mg atoms in liquid ^{3}He-^{4}He mixtures is presented as a case study of an impurity dissolved into liquid helium. We have found that the absorption spectrum of the impurity is rather insensitive to the isotopic composition because the line shift is mostly affected by the total He density around the impurity, not by its actual composition. For bulk liquid mixtures, results are presented as a function of pressure at selected values of the ^{3}He concentration. The results for isotopically pure ^{3}He and ^{4}He liquids doped with Mg are compared with available experimental data.

DOI: 10.1103/PhysRevB.83.174505 PACS number(s): 67.60.−g, 78.40.−q, 32.30.Jc

I. INTRODUCTION

The study of the absorption spectrum of impurities in liquid helium and its droplets has drawn considerable interest because it is a powerful tool to investigate the structure of the dopant-liquid complex, having become a classical field in optical spectroscopy. The optical properties of impurities in liquid ^{4}He and its droplets have been reviewed in Refs. 1 and 2, respectively.

Electronic spectroscopy studies have been carried out for atomic impurities in ^{4}He, and to a lesser extent, in ^{3}He.[3–5] Only very recently, the electronic absorption spectrum of an atomic impurity—a Ca atom—in mixed ^{3}He-^{4}He droplets has been reported and analyzed within density functional (DF) theory.[6] A distinct feature of Ca atoms in mixed helium droplets is that, depending on the size and isotopic composition of the droplet, it may reside at the ^{3}He-^{4}He interface. Therefore, one would expect that its electronic spectrum might shed light on the structure of that interface, as this spectrum is affected by the liquid environment around the impurity.

Experiments on doped mixed droplets have to face the serious problem of determining the actual composition of the system. This is not easy because of the large number of atoms, mostly of ^{3}He, that are evaporated off the droplet after the dopant pick-up, altering the initial composition of the droplet in a way that is difficult to ascertain. The initial composition is not easy to determine either. In contrast, experiments in liquid mixtures may be carried out under well-controlled conditions, fixing, e.g., the ^{3}He concentration $x_3 = N_3/(N_3 + N_4)$ and particle density $\rho = (N_3 + N_4)/V$ and temperature (T) of the mixture, which in turn determine the total pressure (P) throughout the equation of state of the fluid.

In this work, we aim to study the effect of isotopic composition on the absorption spectrum of atomic impurities in both finite (droplets) and extensive (liquid) helium systems. We present results for the $3p \leftarrow 3s$ transition of Na attached to ^{3}He-^{4}He droplets, complementing those we have previously published for Ca.[6] It is well known experimentally[7] and theoretically[8] that, because of the limited solubility of ^{3}He in ^{4}He at low temperatures,[9] mixed droplets have a core-shell structure made of nearly pure ^{4}He and ^{3}He, respectively. Since Na atoms do not dissolve into helium droplets, the *a priori* most interesting situation is when the number of ^{3}He atoms, N_3, is rather small as compared to that of ^{4}He, N_4. Otherwise, the environment around Na is made of pure ^{3}He and one should not expect any difference with the absorption spectrum of Na in isotopically pure ^{3}He droplets.[3]

At variance with the droplet situation, ^{3}He segregation in liquid helium mixtures at low temperatures only appears for concentrations above a critical value that depends on pressure.[9] Hence, it is plausible that the absorption spectrum could be sensitive to the x_3 value of the mixture. To check this hypothesis, we present calculations of the absorption spectrum around the $3s\,3p\ ^1P_1 \leftarrow 3s^2\ ^1S_0$ transition of Mg atoms in liquid helium mixtures for selected values of x_3 and P.

This work is organized as follows. In Sec. II, we briefly recall the DF method used to obtain the structure of doped helium mixtures, drops, and bulk liquid as well, and the procedure used to determine the absorption spectrum incorporating shape fluctuations of the liquid bubble around the dopant. The absorption spectrum of Na in $^4He_{1000}$-$^3He_{N_3}$ droplets with $N_3 = 100$ to 3000, and that of Mg in ^{3}He-^{4}He liquid mixtures for selected values of x_3 and P, is discussed in Sec. III. Finally, a summary is presented in Sec. IV.

II. METHOD

A. Density functional description of the ground state of doped isotopic mixtures

The energy of the Na-droplet complex is written as a functional of the Na wave function $\Phi(\mathbf{r})$, the ^{4}He effective macroscopic wave function $\Psi(\mathbf{r}) = \sqrt{\rho_4(\mathbf{r})}$, where $\rho_4(\mathbf{r})$ is the ^{4}He atomic density normalized to N_4 atoms, and the ^{3}He particle and kinetic energy densities $\rho_3(\mathbf{r})$ (normalized to N_3 atoms) and $\tau_3(\mathbf{r})$.[10] We have used a Thomas-Fermi

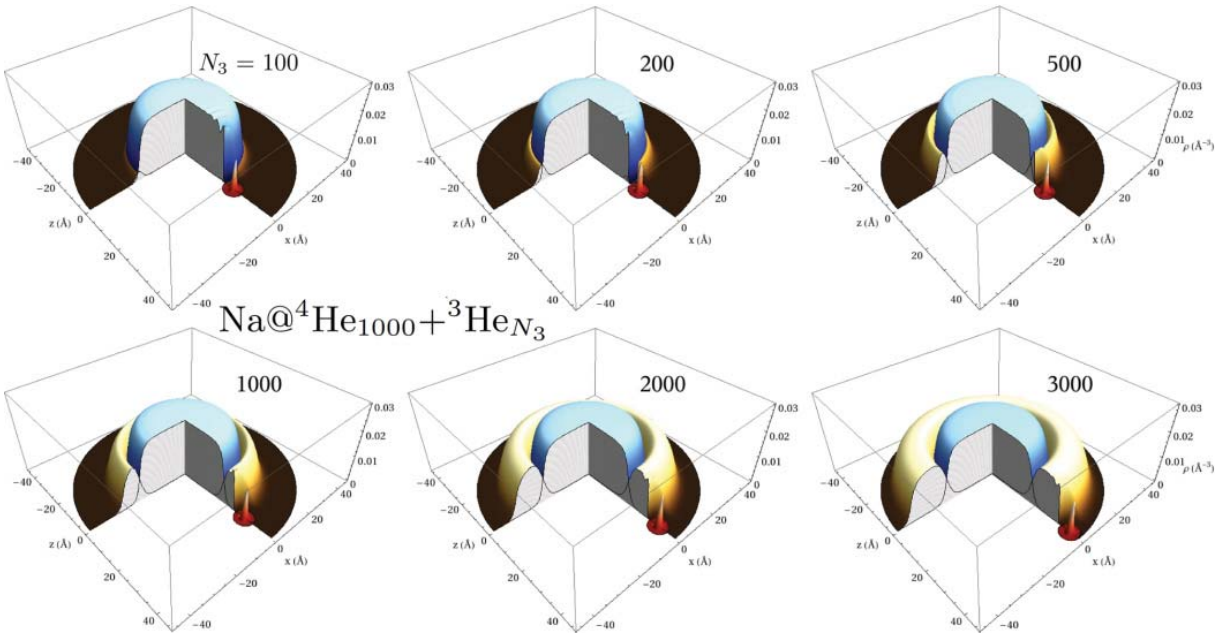

FIG. 1. (Color online) Three-dimensional view of $\mathrm{Na@^4He_{1000}+^3He}_{N_3}$ droplets for different N_3 values. Also shown is the probability density of Na in arbitrary units.

approximation to write $\tau_3(\mathbf{r})$ as a function of $\rho_3(\mathbf{r})$ and its gradient.[3] Within the pair potential approximation, we have[11]

$$E[\Psi,\Phi,\rho_3,\tau_3] = \frac{\hbar^2}{2\,m_{^4\mathrm{He}}}\int d\mathbf{r}\,|\nabla\Psi(\mathbf{r})|^2 + \int d\mathbf{r}\,\mathcal{E}(\rho_4,\rho_3,\tau_3) + \frac{\hbar^2}{2\,m_{\mathrm{Na}}}\int d\mathbf{r}\,|\nabla\Phi(\mathbf{r})|^2 + \iint d\mathbf{r}\,d\mathbf{r}'\,|\Phi(\mathbf{r})|^2\,V_{X^2\Sigma}(|\mathbf{r}-\mathbf{r}'|)\,\rho_{3+4}(\mathbf{r}'). \quad (1)$$

The Na-He $X\,^2\Sigma$ pair potential has been taken from Ref. 12. The equations resulting from the variations of Eq. (1) with respect to Ψ, Φ, and $\rho_3(\mathbf{r})$ are self-consistently solved as indicated in Ref. 11.

Figure 1 displays a three-dimensional view of $\mathrm{Na@^4He_{1000}+^3He}_{N_3}$ droplets for several N_3 values, and the probability density of Na, $|\Phi(\mathbf{r})|^2$, in arbitrary units. The figure shows the above-mentioned core-shell distribution of ^{4}He and ^{3}He atoms in the droplet, as well as the known result that Na does not dissolve into them. In this respect, it is illustrative to compare the results for Na with those for Ca (see Fig. 2 of Ref. 6 corresponding to $\mathrm{Ca@^4He_{1000}+^3He_{2000}}$). So far, Ca is the only known impurity that is dissolved into ^{4}He but not into ^{3}He droplets, and for this reason it may sink into the fermionic component until reaching the surface of the bosonic core. More attractive impurities like OCS reside in the bulk of the core, thus they are instrumental in the discussion of superfluidity at the nanoscale.[7] Here we discuss the remaining case of an impurity that resides at the surface of the droplet irrespective of the isotope. One of the cuts in Fig. 1 displays the pure ^{3}He-^{4}He interface showing the building up of the ^{3}He shell as N_3 increases. It is worth noting that, with a core of 1000 ^{4}He atoms, a large amount of ^{3}He ($N_3 \sim 2000$) is needed before the density of the fermionic shell reaches that of liquid ^{3}He at saturation; see also Ref. 8. The other cut displays the doped ^{3}He-^{4}He interface. Notice that for the $N_4 = 1000$ droplet, one should not expect that the absorption spectrum of Na onto $\mathrm{^4He_{1000}+^3He}_{N_3}$ differs much from that of Na onto an isotopically pure ^{3}He droplet of similar size if $N_3 \gtrsim 1000$.

The starting point for describing a Mg atom in liquid helium mixtures is also Eq. (1). The Mg-He $X\,^1\Sigma$ pair potential has been taken from Ref. 13. In this case, instead of fixing the number of atoms N_3 and N_4, the asymptotic ρ_3 and ρ_4 densities far from the impurity have been fixed to those of the undoped mixture. In practice, we work at fixed P and x_3 values, which in turn fix the ρ_3 and ρ_4 values (and the corresponding chemical potentials) through the $T = 0$ equation of state supplied by our DF.[10] Details of the procedure and method used for solving the variational equations can be found in Ref. 14 for an electron bubble in liquid ^{4}He. The generalization to helium mixtures and atomic impurities is straightforward.

We want to emphasize that our method yields a self-consistent and accurate description of the thermodynamics of undoped liquid mixtures at zero temperature, a necessary starting point to address the properties of the doped system. In particular, it reproduces the $T = 0$ phase diagram of the mixture. Figure 2 shows the calculated phase diagram obtained as explained in Ref. 15.

The top and bottom panels of Fig. 3 show the helium density profile around Mg in the case of isotopically pure ^{4}He and ^{3}He liquids for three different pressures. It can be seen that the helium density is strongly modulated around the impurity, slowly evolving toward the bulk liquid density as the distance

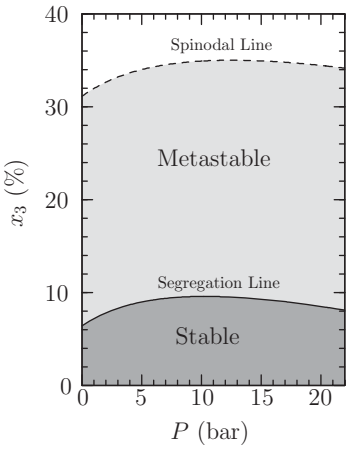

FIG. 2. Calculated phase diagram of the ^{4}He-^{3}He liquid mixture at $T = 0$. The solid line between stable and metastable regions is the maximum solubility line of ^{3}He into ^{4}He, and the dashed line is the spinodal line.

from the impurity increases. Notice also how the liquid density increases as P does, and how the radius of the bubble around the impurity is slightly larger for ^{3}He than for ^{4}He because of the surface tension being smaller for ^{3}He than for ^{4}He. This figure shows that, even for rather weakly interacting dopants such as Mg, the actual structure of the liquid cannot be easily guessed or represented by simple parametrizations. This is especially so in the case of isotopic liquid mixtures; see the middle panel of Fig. 3.

These density profiles already give a first idea of what to expect from the study of the absorption peak as a function of P: the shift increases as the density does, and therefore it will also increase with P. Similarly, the shift should be larger for Mg in isotopically pure ^{4}He than in isotopically pure ^{3}He at given P, as the He-Mg interaction is the same irrespective of the isotope. These facts have been established experimentally.[4,5]

The middle panel of Fig. 3 shows the density profile at $P = 10$ bar for $x_3 = 9\%$. It can be seen from Fig. 2 that these conditions allow us to carry out the calculation for nearly the largest possible ^{3}He concentration before segregation. For the sake of comparison, the result for pure ^{4}He is also shown. Whereas the results displayed in the other panels of Fig. 3 are known to some extent, to the best of our knowledge the density profiles of isotopic mixtures of liquid helium around an attractive impurity have not been previously determined. Along the lines of the other two panels, one would expect a very weak dependence of the atomic shift on the composition of the mixture. Comparing the total helium densities displayed in the middle panel of Fig. 3, the atomic shift might be slightly larger for liquid ^{4}He than for the mixture at the same pressure. In the next section, we address these issues in detail, confirming these expectations.

We would like to close the discussion of the density profiles by pointing out two interesting characteristics of the liquid mixture at low temperatures, relevant for the forthcoming discussion of the absorption spectrum. The first feature is that, as can be seen from Fig. 3, substituting ^{4}He by ^{3}He atoms at a given P does not result in a sizable change in the liquid

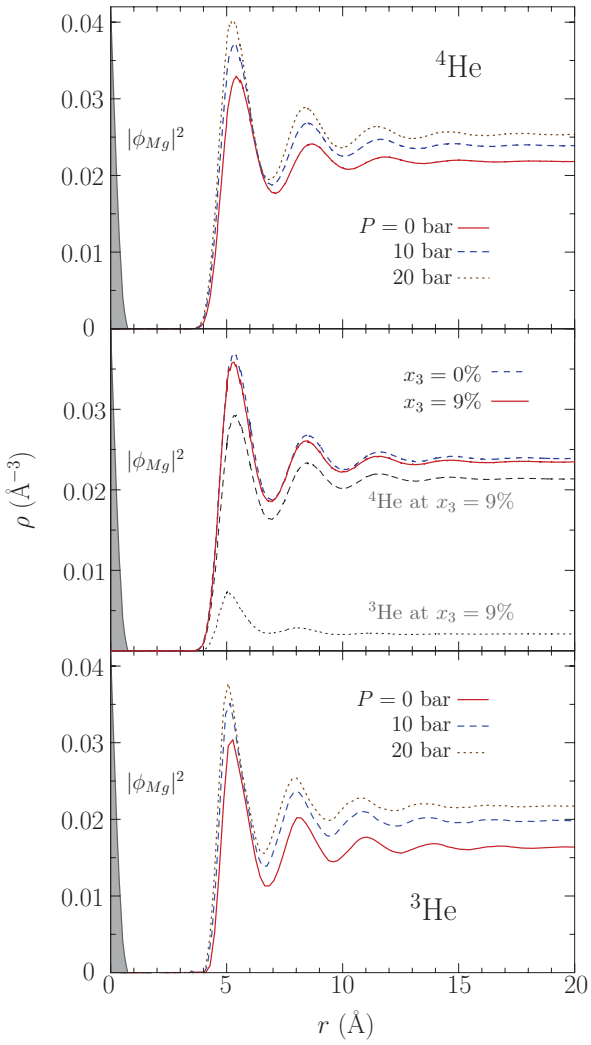

FIG. 3. (Color online) Selected density profiles of the liquid helium mixture around an Mg impurity whose probability density in represented in arbitrary units. Top panel: pure ^{4}He. Bottom panel: pure ^{3}He. Middle panel: density profiles at $P = 10$ bar for $x_3 = 9\%$. Solid line, total density; thin dashed line, ^{4}He density; dotted line, ^{3}He density. For the sake of comparison, the profile of isotopically pure ^{4}He is also shown (dashed line).

total density. This is due to the high incompressibility of liquid helium. The other feature worth noting is that ^{3}He atoms do not segregate around the impurity coating the surface of the bubble. This is due to the large zero-point energy that a ^{3}He atom would have in such a small cavity, and it is more marked the larger the impurity-helium interaction is. As a consequence, the impurity bubble is coated by ^{4}He atoms and not by ^{3}He, in spite of the density increase of both isotopes at the first solvation shell, allowing the appearance of the rovibrational spectrum of OCS molecules in helium droplets[7] that otherwise would be quenched by the presence of normal-phase ^{3}He atoms. This is at variance with the situation at the free surface of a mixed drop or liquid mixture, where the existence of Andreev states

bearing a large capacity of hosting ^{3}He atoms makes possible the accumulation of this isotope at the surface.[8]

B. Absorption spectrum

To determine the absorption spectrum of an impurity atom embedded in a condensed system, it is customary to use Lax's method,[16] together with the diatomics-in-molecules approach.[17] This is basically the method we have followed,[11] once the ground state (gs) of the dopant-helium mixture (droplet or bulk liquid) has been determined. The $^2\Pi$ and $^2\Sigma$ excited pair potentials for Na-He are from Ref. 18, and the $^1\Pi$ and $^1\Sigma$ ones for Mg-He are from Ref. 19. In the case of Na, we have also considered the spin-orbit splitting.[11]

With only these ingredients, the model yields a good description of the absorption energies—provided the pair potentials are accurate enough—but the shape, especially the width, of the absorption line is poorly reproduced. The well-known reason for this drawback is the neglect of the coupling of the impurity dipole excitation to the shape fluctuations (modes) of the liquid cavity around it. Including this coupling in the calculation yields a much better agreement with experiments. This is illustrated, e.g., in Ref. 20 for Mg atoms in ^{4}He droplets and in Ref. 21 for electron bubbles in liquid ^{4}He. Taking into account shape fluctuations is very cumbersome if the impurity bubble is not spherical. The situation is far more complex for liquid ^{3}He and mixtures because the modes of the cavity are difficult to determine.

Shape fluctuations are effortlessly calculated in quantum Monte Carlo simulations of the absorption spectrum[22–24] by taking advantage of the information carried out by the quantum "walkers." Somewhat inspired by this atomiclike simulation, an easy-to-implement method has been proposed within DF theory to include shape fluctuations, and it has been applied to the case of Cs in liquid ^{4}He,[25] and was later adapted to the droplet geometry.[26,27] The extension to the case of isotopic mixtures is straightforward, but for the sake of completeness we present it here as applied to the case of a Na impurity, outlining the method we have followed to determine the absorption spectrum of an impurity in liquid helium.

The Born-Oppenheimer approximation allows the factorization of the electronic and nuclear wave functions, and the Franck-Condon approximation allows the positions of the atomic nuclei to remain frozen during the electronic transition. Within these approximations, the line shape for an electronic transition from the gs to an excited state (ex) is obtained as the Fourier transform of the time-correlation function,

$$I(\omega) \propto \sum_m \int dt e^{-i(\omega+\omega^{\rm gs})t} \int d^3\mathbf{r} \Phi^{\rm gs*} e^{(it/\hbar)H_m^{\rm ex}} \Phi^{\rm gs} , \quad (2)$$

where $\hbar\omega^{\rm gs}$ and $\Phi^{\rm gs}(\mathbf{r})$ are the eigenenergy and eigenfunction of Na in its gs, respectively. The Hamiltonian is $H_m^{\rm ex} = T_{\rm kin} + V_m^{\rm ex}(\mathbf{r})$, where $T_{\rm kin}$ is the kinetic energy operator and $V_m^{\rm ex}(\mathbf{r})$ is the potential energy surface defined by the mth eigenvalue of the excited potential matrix $V(\mathbf{r}) = U(\mathbf{r}) + V_{\rm SO}$, where $U(\mathbf{r})$ is the convolution of the excited pair potentials $^2\Pi$ and $^2\Sigma$ with the *total* helium density $\rho(\mathbf{r})$, as the ^{3}He- and ^{4}He-impurity pair potentials are the same, and $V_{\rm SO}$ accounts for the spin-orbit coupling.[11] Introducing $\Phi^{\rm gs}(\mathbf{r}) = \sum_\nu a_\nu^m \Phi_\nu^m(\mathbf{r})$ in Eq. (2), where $\Phi_\nu^m(\mathbf{r})$ are the eigenfunctions of $H_m^{\rm ex}$ and $a_\nu^m = \int d^3\mathbf{r}\, \Phi_\nu^m(\mathbf{r})^* \Phi^{\rm gs}(\mathbf{r})$ are the Franck-Condon factors, we obtain

$$\begin{aligned} I(\omega) &\propto \sum_m \int dt e^{-i(\omega+\omega^{\rm gs})t} \sum_\nu \left|a_\nu^m\right|^2 e^{i\omega_\nu^m t} \\ &= \sum_m \sum_\nu \left|a_\nu^m\right|^2 \delta\left(\omega + \omega^{\rm gs} - \omega_\nu^m\right) , \end{aligned} \quad (3)$$

where $\hbar\omega_\nu^m$ are the eigenvalues of $H_m^{\rm ex}$.

If the Franck-Condon factors arise from the overlap between the gs and excited states with large quantum numbers, corresponding to the continuous or quasicontinuous spectrum of $H_m^{\rm ex}$, we can assume that $\langle T_{\rm kin}\rangle \ll \langle V_m^{\rm ex}\rangle$, and the Hamiltonian is approximated by $H_m^{\rm ex} \sim V_m^{\rm ex}(\mathbf{r})$. Introducing this approximation in Eq. (2) and integrating over time, we get the semiclassical expression for $I(\omega)$,

$$I(\omega) \propto \sum_m \int d^3\mathbf{r} |\Phi^{\rm gs}(\mathbf{r})|^2 \delta(\omega - [V_m^{\rm ex}(\mathbf{r})/\hbar - \omega^{\rm gs}]) . \quad (4)$$

We have evaluated this expression as follows. First, the helium distribution is stochastically represented by a large number of configurations n_c, of the order of 10^6. Each configuration consists of a set of N positions for the He atoms in the sampling box and one for the impurity. These positions are randomly generated by importance sampling techniques, using the DF helium density $\rho(\mathbf{r})/N$ as the probability density distribution, plus a hard-sphere repulsion between He atoms to approximately take into account He-He correlations. The diameter of the sphere has to be of the order of $h = 2.18$ Å to be consistent with the DF description of the liquid, as h is the length used in the functional to screen the Lennard-Jones interaction between particles and to compute the coarse-grained density.[10] We have chosen a density-dependent sphere radius of the form

$$R_i = R(\mathbf{r}_i) = \frac{h}{2}\left(\frac{\rho_0}{\bar\rho(\mathbf{r}_i)}\right)^{1/3} , \quad (5)$$

where ρ_0 is the saturation density value and $\bar\rho$ is the coarse-grained density, defined as the averaged density over a sphere of radius h. Although this scaling has no effect in the bulk, it is fundamental to correctly reproducing the density in the droplet surface region. The rationale for choosing this R_i is sketched in the Appendix. Lastly, the position of the impurity is also randomly generated using $|\Phi^{\rm gs}(\mathbf{r})|^2$ as the probability density distribution.

To determine the line shape, we obtain for each configuration $\{j\}$ the $V_m^{\rm ex}\{j\}$ eigenvalues of the excited-state energy matrix $\sum_i U(|\mathbf{r}_i^{\{j\}} - \mathbf{r}_{\rm Na}^{\{j\}}|) + V_{\rm SO}$ [Eq. (16) of Ref. 11] and subtract from them the pairwise sum of the gs pair potential interactions $V^{\rm gs}\{j\} = \sum_i V_{X^2\Sigma}(|\mathbf{r}_i^{\{j\}} - \mathbf{r}_{\rm Na}^{\{j\}}|)$ to obtain the excitation energy. The histogram of the collected stochastic energies is identified with the absorption spectrum, i.e.,

$$I(\omega) \propto \sum_m \frac{1}{n_c} \sum_{\{j\}}^{n_c} \delta\left[\omega - \left(V_m^{\rm ex}\{j\} - V^{\rm gs}\{j\}\right)/\hbar\right] . \quad (6)$$

In this way, we obtain the absorption spectrum of impurities in liquid helium including shape fluctuations. When this is the

main source of broadening, as for impurities embedded in the liquid or in the bulk of drops, the method has proved to reproduce fairly well the broadening of the absorption line, as we show for Mg in Sec. III. Note that other sources of broadening such as thermal wandering[20] or droplet size distribution effects may have a sizable influence for impurities residing in the outer surface of the droplet, and they are not accounted for by this procedure.

III. ABSORPTION SPECTRUM RESULTS

A. Na in mixed helium droplets

Figure 4 shows the absorption spectrum for Na@^{4}He$_{1000}$ +^{3} He$_{N_3}$ mixed droplets with $N_3 =$ 100,500,1000, and 3000. The vertical lines represent the location of the absorption lines of the free Na atom. As expected, the shift in the spectrum increases with the number of ^{3}He atoms.[3] In the ^{4}He$_{1000}$ +^{3} He$_{100}$ droplet, the effect of ^{3}He is barely perceptible and its spectrum is sensibly that of Na in the isotopically pure ^{4}He droplet. One might expect the impurity to draw the ^{3}He atoms and be quickly surrounded by them, but this is not quite so even for a more attractive impurity such as Ca.[24,28]

In the $N_3 = 1000$ and 3000 drops, it is the ^{4}He core that plays no significant role, and the spectrum is sensibly that of the isotopically pure ^{3}He droplet.[29] The $N_3 = 500$ droplet is an intermediate case, in which there is enough ^{3}He to influence the absorption spectrum but the number of ^{3}He atoms is still small, and the density in the ^{3}He shell does not reach that of the liquid at saturation; see, e.g., Ref. 8 and Fig. 1. In this configuration, the shift is slightly smaller than in a pure ^{3}He drop, although the difference is too small to be detectable. We recall that the experiments have been carried out for isotopically pure droplets of about 5000 atoms. The calculated peaks are narrower than in the experiment because Na resides at the outer surface of the droplet and thermal wandering and droplet-size distribution effects should contribute to the broadening in a non-negligible way.[11]

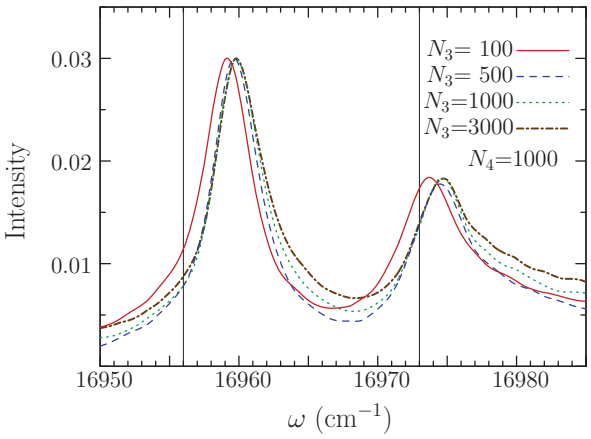

FIG. 4. (Color online) Absorption spectrum (arbitrary units) of Na in ^{4}He$_{1000}$+^{3}He$_{N_3}$ droplets with $N_3 = 100$ (solid line), 500 (dashed line), 1000 (dotted line), and 3000 (dash-dotted line). The thin vertical lines represent the gas-phase transitions. The spectra are normalized so that the more intense peaks all have the same height.

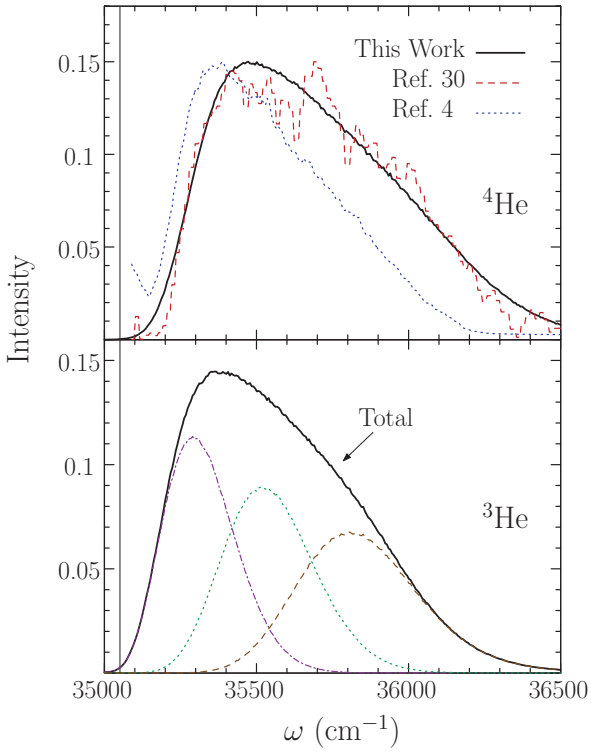

FIG. 5. (Color online) Top panel: Calculated absorption spectrum (arbitrary units) of Mg in liquid ^{4}He at $P = 0$ bar (solid line) compared to the experimental results of Refs. 30 (dashed line) and 5 (dotted line). The spectra are normalized so that the peaks have the same height. Bottom panel: Calculated absorption spectrum (arbitrary units) of Mg in liquid ^{3}He at $P = 0$ bar. The line has been decomposed into its two Π components and one Σ component, the latter one being the higher-energy transition. The thin vertical line represents the gas-phase transition.

B. Mg in liquid helium mixtures

Isotopic liquid helium mixtures are better suited than mixed drops to determine the effect of the isotopic composition on the absorption line, as one avoids finite-size effects and the actual composition of the fluid sample can be controlled. In addition, they offer the possibility to study the pressure effect on the spectrum.

The reason for choosing Mg atoms for this study is twofold. First, there are detailed results for its absorption spectrum in pressurized isotopically pure liquid ^{3}He and ^{4}He,[5,30] indicating that the shift in the absorption peak is about 100 cm^{-1} smaller in ^{3}He than in ^{4}He.[5] It is thus reasonable to expect that the absorption spectrum may show some sensitivity to the isotopic composition of the mixture. Secondly, the adiabatic Mg-He pair potentials for the ground[13] and excited states[19] are known with good accuracy. We want to mention the existence of a series of recent studies of Mg in helium droplets aimed at ascertaining whether this impurity resides in the

bulk or at the surface of ^{4}He drops.[19,20,31–33] Most studies point toward a sizable radial delocalization of Mg inside large drops.

In a first stage, we have computed the absorption spectrum of Mg in isotopically pure liquid ^{4}He and ^{3}He. For the former, there are two inconsistent sets of experimental data obtained by the same group, both of which are compared with our calculations in the top panel of Fig. 5. No detailed results for the line shape in the case of ^{3}He have been published for comparison. We remind the reader that our calculations are at $T = 0$, whereas the experiments have been carried out at 1.4 K.

While our calculations compare very well with the experimental results for ^{4}He in Ref. 30, they are blueshifted with respect to those of Ref. 5 for ^{4}He and ^{3}He as well. Despite this discrepancy, we have found, in agreement with the experimental findings,[5] that the shift is 0.77 nm larger in bulk ^{4}He than in bulk ^{3}He. This is an important check to assure that the calculation may disclose effects associated with the isotopic composition of the liquid mixture, as shown below.

The pressure dependence of the absorption spectrum of Mg in isotopically pure liquid ^{4}He and ^{3}He is shown in Fig. 6 for $P = 0$, 10, and 20 bar, and the peak energy is represented in Fig. 7 as a function of pressure. This dependence is in qualitative agreement with experiment,[5] although our results are systematically blueshifted with respect to the experimental results by about 1 nm. The crosses in Fig. 7 represent the peak energy slightly below the zero-temperature segregation line as a function of pressure. Thus, each point corresponds to a different x_3 value, as shown in Fig. 2. We conclude that the shift in the peak energy of the Mg absorption spectrum is significant. However, the size of the line can make it hard to determine experimentally the x_3 dependence. This is illustrated in Fig. 8, where we have drawn the absorption spectrum of Mg in an $x_3 = 9.4\%$ mixture at $P = 10$ bar. The absorption peak is shifted by 28 cm^{-1} with respect to the isotopically

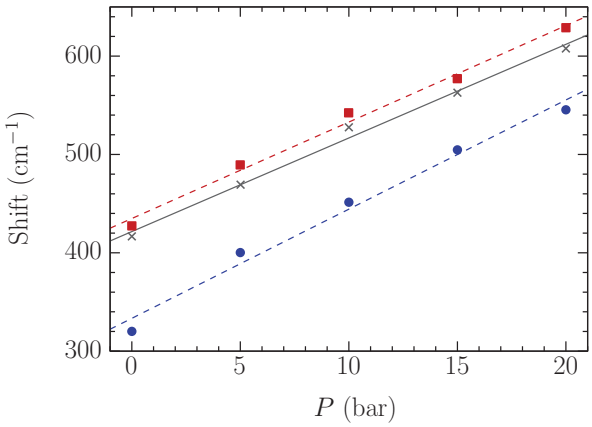

FIG. 7. (Color online) Peak energy shift of the absorption spectrum of Mg in isotopically pure liquid ^{4}He (squares) and ^{3}He (dots) as a function of pressure. The crosses represent the peak energy shift slightly below the segregation line for the corresponding pressures; the x_3 values are 6.3%, 8.9%, 9.4%, 9.2%, and 8.4% for $P = 0$, 5, 10, 15, and 20 bar, respectively. Least-squares linear fits for each set of points are drawn as a guide to the eye.

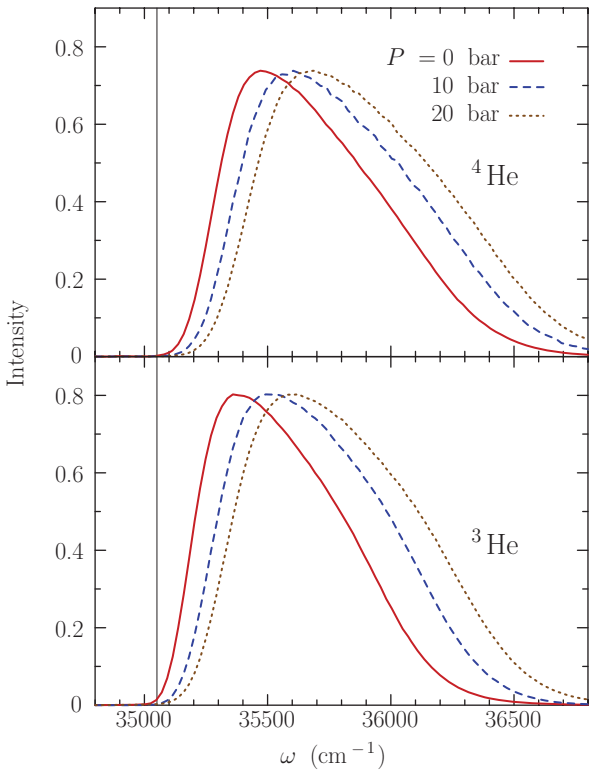

FIG. 6. (Color online) Top panel: Calculated absorption spectrum (arbitrary units) of Mg in liquid ^{4}He at $P = 0$ (solid line), 10 (dashed line), and 20 bars (dotted line). Bottom panel: Same as top panel for ^{3}He. The thin vertical line represents the gas-phase transition. The spectra are normalized so that the peaks have the same height.

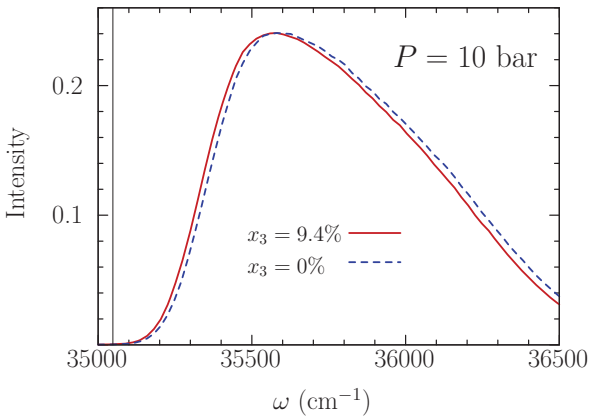

FIG. 8. (Color online) Absorption spectrum (arbitrary units) of Mg in an $x_3 = 9.4\%$ liquid mixture at $P = 10$ bar (solid line). The dashed line is the result for the isotopically pure liquid ^{4}He at the same pressure. The thin vertical line represents the gas-phase transition. The spectra are normalized so that the peaks have the same height.

pure liquid ^{4}He, in spite of the small morphological changes in the density profile introduced by this small ^{3}He amount (see Fig. 3).

IV. SUMMARY

We have studied the absorption spectrum of atomic impurities in mixed helium drops and liquid helium mixtures, paying special attention to the dependence of the spectrum on the ^{3}He concentration. For the study of drops, we have chosen Na as the impurity, which always resides on the surface of the drop, complementing the studies carried out in Ref. 6 for Ca.

For droplets of the size and composition addressed herein, we have found that the shift in mixed droplets is larger than in ^{4}He droplets but slightly smaller than in ^{3}He droplets. Even though a large amount of ^{3}He is needed for the density in the outer shell of the mixed droplet to reach the bulk liquid ^{3}He value, our results indicate that the spectrum of the impurity is very insensitive to the isotopic composition and it rapidly saturates to the value of pure ^{3}He droplets when the quantity of ^{3}He is increased. From this we infer that the effect of isotopic composition on the absorption spectrum is hardly detectable for alkali impurities in helium droplets. We have chosen Mg for the study of liquid mixtures, and we have compared the results obtained for isotopically pure liquid ^{4}He and ^{3}He with the experiments reported in Refs. 5 and 30. We have found that the peak energy in saturated helium mixtures can be shifted by up to some tens of cm^{-1} from that in pure ^{4}He at the same pressure. While much smaller atomic shifts from the gas-phase value have been detected experimentally, to determine the dependence of the atomic shift on the isotopic composition of the mixture is an experimental challenge due to the large width of the absorption line.

Finally, we would like to point out that the infrared spectrum of excess electrons might be a way to determine the structure of electron bubbles in isotopic mixtures of liquid helium, as it has been for isotopically pure liquid ^{4}He or ^{3}He.[34] Due to the electron-helium repulsion, electron bubbles are fairly large, with a radius of about 18.5 Å for ^{4}He and 22.5 Å for ^{3}He.[35] At variance with the situation for the small bubbles around an atomic impurity in liquid helium mixtures, the electron bubble surface should be coated by ^{3}He, as it is for bubbles appearing in homogeneous cavitation processes.[15] This coating increases the bubble radius with respect to that of isotopically pure ^{4}He, as it decreases the surface tension of the liquid. Since the electron spectrum is very sensitive to the bubble radius, determining it would probe the structure of the electron bubble in the mixture. Knowledge of this structure has potential implications for cavitation in liquid helium mixtures.[36,37] Work is in progress to obtain the electron absorption energies in liquid helium mixtures.

ACKNOWLEDGMENTS

We would like to thank Frank Stienkemeier and Oliver Bünermann for useful exchanges. This work has been performed under Grants No. FIS2008-00421/FIS from DGI, Spain (FEDER), and No. 2009SGR01289 from Generalitat de Catalunya. D.M. has been supported by the ME (Spain) FPU program, Grant No. AP2008-04343. A.H. has been supported by the MICINN (Spain) FPI program, Grant No. BES-2009-027139.

APPENDIX

Ignoring normalization, which is irrelevant for the present discussion, the probability distribution we have chosen for sampling N helium atoms is

$$P^N(\{\mathbf{r}_i\}) = \prod_{i=1}^{N} \frac{\rho(\mathbf{r}_i)}{N} \prod_{j<i}^{N} \Theta(r_{ij} - h), \tag{A1}$$

where Θ is the step function. The atomic density $\langle \sum_i \delta(r - r_i) \rangle$ corresponding to this probability distribution is

$$\left\langle \sum_{i=1}^{N} \delta(r - r_i) \right\rangle = \rho(r) \int \left(\prod_{j=1}^{N-1} dr_j \Theta(|\mathbf{r}_j - \mathbf{r}| - h) \right) P^{N-1}(\{\mathbf{r}_i\}) \neq \rho(r). \tag{A2}$$

Hence, due to the He-He correlations introduced in P^N, the density of the system is not equal—and cannot be—to the DF particle density $\rho(r)$, and one has to do something to recover $\rho(r)$ back from the sampling. To do so, we have introduced a density dependence on h such that the integral appearing in Eq. (A2) is a constant that could be absorbed in the normalization. This cannot be done exactly, but if one assumes that $\rho(r)$ varies smoothly, i.e., $\nabla\rho(\mathbf{r}) \ll \rho(\mathbf{r})/h$, then the result of the integral can be written as a power series of $h^3\bar{\rho}(\mathbf{r})$, where $\bar{\rho}(\mathbf{r})$ is the coarse-grained density. Then, to turn the integral into a constant, we just need to add a density dependence in h of the form $h \propto \bar{\rho}(\mathbf{r})^{-1/3}$. This is the reason why we have chosen the hard-sphere radius R as expressed in Eq. (5).

[1] B. Tabbert, H. Günther, and G. zu Putlitz, J. Low Temp. Phys. **109**, 653 (1997).

[2] J. P. Toennies and A. F. Vilesov, Angew. Chem. Ind. Ed. **43**, 2622 (2004); F. Stienkemeier and K. K. Lehmann, J. Phys. B **39**, R127 (2006); M. Barranco, R. Guardiola, S. Hernández, R. Mayol, Jesús Navarro, and M. Pi, J. Low Temp. Phys. **142**, 1 (2006); J. Tiggesbäumker and F. Stienkemeier, Phys. Chem. Chem. Phys. **9**, 4748 (2007); M. Y. Choi, G. E. Douberly, T. M. Falconer, W. K. Lewis, C. M. Lindsay, J. M. Merrit, P. L. Stiles, and R. E. Miller, Int. Rev. Phys. Chem. **25**, 15 (2006); K. Szalewicz, *ibid.* **27**, 273 (2008).

[3] F. Stienkemeier, O. Bünermann, R. Mayol, F. Ancilotto, M. Barranco, and M. Pi, Phys. Rev. B **70**, 214509 (2004).

[4] Y. Moriwaki and N. Morita, Eur. Phys. J. D **33**, 323 (2005).

[5]Y. Moriwaki, K. Inui, K. Kobayashi, F. Matsushima, and N. Morita, J. Mol. Struct. **786**, 112 (2006).
[6]O. Bünermann, M. Dvorak, F. Stienkemeier, A. Hernando, R. Mayol, M. Pi, M. Barranco, and F. Ancilotto, Phys. Rev. B **79**, 214511 (2009).
[7]S. Grebenev, J. P. Toennies, and A. F. Vilesov, Science **279**, 2083 (1998).
[8]M. Pi, R. Mayol, and M. Barranco, Phys. Rev. Lett. **82**, 3093 (1999).
[9]D. O. Edwards and M. S. Pettersen, J. Low Temp. Phys. **87**, 473 (1992).
[10]M. Barranco, M. Pi, S. M. Gatica, E. S. Hernández, and J. Navarro, Phys. Rev. B **56**, 8997 (1997).
[11]A. Hernando, M. Barranco, R. Mayol, M. Pi, and M. Krośnicki, Phys. Rev. B **77**, 024513 (2008).
[12]S. H. Patil, J. Chem. Phys. **94**, 8089 (1991).
[13]R. J. Hinde, J. Phys. B **36**, 3119 (2003).
[14]D. Mateo, M. Pi, and M. Barranco, Phys. Rev. B **81**, 174510 (2010).
[15]M. Guilleumas, D. M. Jezek, M. Pi, M. Barranco, and J. Navarro, Phys. Rev. B **51**, 1140 (1995).
[16]M. Lax, J. Chem. Phys. **20**, 1752 (1952).
[17]F. O. Ellison, J. Am. Chem. Soc. **85**, 3540 (1963).
[18]J. Pascale, Phys. Rev. A **28**, 632 (1983).
[19]M. Mella, G. Calderoni, and F. Cargnoni, J. Chem. Phys. **123**, 054328 (2005).
[20]A. Hernando, M. Barranco, R. Mayol, M. Pi, and F. Ancilotto, Phys. Rev. B **78**, 184515 (2008).
[21]H. J. Maris and W. Guo, J. Low Temp. Phys. **137**, 491 (2004).
[22]S. Ogata, J. Phys. Soc. Jpn. **68**, 2153 (1999).
[23]M. Mella, M. C. Colombo, and F. G. Morosi, J. Chem. Phys. **117**, 9695 (2002).
[24]R. Guardiola, J. Navarro, D. Mateo, and M. Barranco, J. Chem. Phys. **131**, 174110 (2009).
[25]T. Nakatsukasa, K. Yabana, and G. F. Bertsch, Phys. Rev. A **65**, 032512 (2002).
[26]A. Hernando, M. Barranco, R. Mayol, M. Pi, F. Ancilotto, O. Bünermann, and F. Stienkemeier, J. Low Temp. Phys. **158**, 105 (2010).
[27]A. Hernando, R. Mayol, M. Pi, M. Barranco, I. S. K. Kerkines, and A. Mavridis, Int. J. Quantum Chem. **111**, 400 (2011).
[28]D. Mateo, M. Barranco, R. Mayol, and M. Pi, Eur. Phys. J. D **52**, 63 (2009).
[29]Due to an unfortunate mistake in the calculation of the spectra, by which the mean gs potential interaction was used in Eq. (6) instead of its stochastic value, the calculated shift for ^{3}He droplets in Ref. 26 is in error.
[30]Y. Moriwaki and N. Morita, Eur. Phys. J. D **5**, 53 (1999).
[31]J. Reho, U. Merker, M. R. Radcliff, K. K. Lehmann, and G. Scoles, J. Chem. Phys. **112**, 8409 (2000).
[32]Y. Ren and V. V. Kresin, Phys. Rev. A **76**, 043204 (2007).
[33]A. Przystawik, S. Göde, T. Döppner, J. Tiggesbäumker, and K-H. Meiwes-Broer, Phys. Rev. A **78**, 021202(R) (2008).
[34]C. C. Grimes and G. Adams, Phys. Rev. B **45**, 2305 (1992).
[35]V. Grau, M. Barranco, R. Mayol, and M. Pi, Phys. Rev. B **73**, 064502 (2006).
[36]M. Barranco, M. Guilleumas, M. Pi, and D. M. Jezek, in *Microscopic Approaches to Quantum Liquids in Confined Geometries*, edited by E. Krotscheck and J. Navarro (World Scientific, Singapore, 2002).
[37]H. J. Maris, J. Phys. Soc. Jpn. **77**, 111008 (2008).

2.2 A density functional study of the structure of small OCS@^{3}He$_N$ clusters

Resumen (Spanish)

La estructura de agregados con $N = 1$, 8, 18, y 40 átomos de ^{3}He dopados con una molécula de OCS se ha calculado mediante un esquema Kohn-Sham del funcional de la densidad. El estado fundamental para $N = 1$ está altamente localizado alrededor de la "cintura" de la molécula, y los excitados están considerablemente más deslocalizados. El agregado con 8 átomos presenta una densidad apreciable en ambos extremos de la molécula linear y en la cintura. Con $N = 18$ la molécula pasa a estar completamente solvatada por ^{3}He. Con $N = 40$ la densidad muestra dos capas de solvatación completas con estructura más bien esférica. Una comparación con cálculos realizados para los mismos tamaños con ^{4}He muestra apreciables similitudes como la acumulación alrededor de la cintura molecular, pero también revela una estructura más difusa y menos anisotrópica en el caso del ^{3}He.

Estos cálculos se presentan en el contexto del análisis reciente del espectro infrarojo del OCS medido en grandes gotas de ^{3}He puro.[13] El momento de inercia de la estructura constituida por 11 átomos, consistente con los datos experimentales, se encuentra entre los momentos de inercia predichos en este trabajo para $N = 8$ y 18 átomos. En general, los cálculos muestran que las gotas de ^{3}He dopadas son ligeramente más difusas y menos ligadas que sus equivalentes de ^{4}He.

THE JOURNAL OF CHEMICAL PHYSICS **138**, 044321 (2013)

A density functional study of the structure of small OCS@^{3}He$_N$ clusters

David Mateo,[1] Martí Pi,[1] Jesús Navarro,[2] and J. Peter Toennies[3]
[1]*Departament E.C.M., Facultat de Física, and IN^{2}UB, Universitat de Barcelona, Diagonal 645, E-08028 Barcelona, Spain*
[2]*IFIC (CSIC-Universidad de Valencia), Apartado Postal 22085, E-46.071-Valencia, Spain*
[3]*Max Planck Institut für Dynamik und Selbstorganisation, Am Fassberg 17, 37077 Göttingen, Germany*

(Received 15 November 2012; accepted 2 January 2013; published online 31 January 2013)

Kohn-Sham density functional calculations are reported for the structures of clusters consisting of a carbonyl sulfide (OCS) molecule with $N = 1$, 8, 18, and 40 attached ^{3}He atoms. The $N = 1$ cluster ground state is highly localized at the molecular waist (donut ring position), but for higher levels of excitation becomes increasingly delocalized. The first magic cluster with 8 atoms has a significant density at both ends of the molecule in addition to the donut ring. With $N = 18$ ^{3}He atoms the molecule is enclosed by a magic number closed shell. Another magic stable structure consisting of two nearly isotropically spherical closed shells is found at $N = 40$. A comparison with calculations for the same sized ^{4}He clusters show some important similarities, e.g., pile up at the donut ring position but altogether a more diffuse, less anisotropic structure. These results are discussed in the light of the recently analyzed infrared spectra measured in large pure ^{3}He droplets ($N \approx 1.2 \times 10^4$) [B. Sartakov, J. P. Toennies, and A. F. Vilesov, J. Chem. Phys. **136**, 134316 (2012)]. The moments of inertia of the 11 atom spherical shell structure, which is consistent with the experimental spectrum, lies between the predicted moments of inertia for $N = 8$ and $N = 18$ clusters. Overall the calculations reveal that the structures and energies of small doped ^{3}He are only slightly more diffuse and less energetic than the same ^{4}He clusters. © *2013 American Institute of Physics*. [http://dx.doi.org/10.1063/1.4788828]

I. INTRODUCTION

In the course of the last two decades superfluid droplets of ^{4}He atoms have become established as very gentle and ultra-cold, nearly ideal matrix for high resolution spectroscopy.[1,2] One of the most surprising observations is the appearance of well resolved rotational lines, as first observed for SF_6 and carbonyl sulfide (OCS), indicating that the molecules rotate freely inside the droplets. This remarkable behaviour has since been confirmed for more than 30 other small molecules and several clusters. Another important observation made for heavy molecules like OCS embedded in superfluid ^{4}He droplets is the increase of the effective moment of inertia (MOI) by about a factor 2.8 compared to the free OCS molecule.[3] The increased MOI can be explained by a symmetric donut ring of ^{4}He atoms around the waist of the OCS molecule, which participate in the end-over-end rotations of the molecule. The ring consists of 5 atoms in the case of small clusters with only that number of atoms.[4–7] In larger clusters the evidence indicates that the donut ring consists of 6 atoms.[3,8,9] Theory has identified the donut atoms as a non-superfluid fraction as opposed to the other surrounding superfluid atoms which do not rotate with the molecule.[10] Recent spectroscopic and theoretical studies of linear molecules, such as CO_2 and N_2O, with $N = 2$ to 80 attached ^{4}He atoms also suggest the presence of a donut ring around their waist.[11,12] The absence of the expected Q-branch in the ro-vibrational spectrum of molecules in ^{4}He droplets is consistent with the fact that the energy of axial rotations of the donut ring of atoms is too large for excitation in the very cold droplets. The absence of Q-branches in small ^{4}He doped clusters with $N = 2$ to 80 atoms has also been explained in the same way.[4] A similar explanation also applies to rings of 5 and 6 bosonic pH_2 molecules.[13] Thus the accumulation of particles in the donut ring position appears to be a characteristic property of bosons.

Fermionic ^{3}He clusters and droplets are of even more basic interest than those made up of ^{4}He atoms since all nuclei, atoms, and molecules may be looked upon each as a special type of fermionic cluster and thus the understanding of their interactions is truly fundamental. Of all the fermions ^{3}He is the simplest neutral fermion with the twofold unique characteristic of occurring both in the thermodynamic limit as a bulk liquid and as a finite-sized droplet. ^{3}He droplets have been predicted to have temperatures of the order of 0.1 K[14] as recently confirmed experimentally[15] and are therefore much colder than ^{4}He droplets (0.37 K),[16,17] but not cold enough to be superfluid ($T_c \sim 3 \times 10^{-3}$ K). Thus ^{3}He droplets were used to test for the effect of superfluidity on the dynamical behavior of the embedded chromophore molecule OCS.[18] The broad unresolved spectrum observed in pure ^{3}He droplets was interpreted as evidence that the sharp rotational spectrum of the same molecule in ^{4}He droplets results from their being superfluid. Subsequently it was suggested that it was not the lack of hydrodynamic superfluidity, but instead the strong coupling to the particle-hole excitations of the fermionic ^{3}He bath, not present in bosonic ^{4}He with its sharp phonon and roton dispersion curve, that caused the line broadening.[19]

Very recently the infrared spectrum of OCS in large pure ^{3}He droplets reported in 1998[18] was fully analyzed.[15] The analysis indicates that as with ^{4}He droplets a Q-branch is most likely absent and that the effective moment of inertia is even

larger than in ^{4}He droplets by a factor of two. Compared to the free molecule the MOI is a factor 5.5 larger. The increase was attributed to an evenly distributed shell of 11 ^{3}He atoms surrounding the chromophore.

Aside from the above infrared study, only a few other spectroscopic experiments have been reported for ^{3}He droplets all of which have been in the visible-UV region.[20–26] These experiments have revealed changes in the line shifts and widths of optical transitions of alkali atoms[22,23] that are smaller in ^{3}He than in ^{4}He droplets. For both isotopes these shifts and widths are small since alkali atoms are located on the surface of the droplets irrespective of the helium isotope.[23] It has also been established that alkaline earth atoms heavier than Mg reside on the surface of ^{4}He droplets whereas they all reside in the interior of ^{3}He droplets.[25] One experiment has reported on the spectroscopy of Ca attached to mixed ^{3}He-^{4}He droplets,[24] concluding that the Ca atom sits at the interface of both isotopes. In the only experiment involving embedded molecules the vibronic spectrum of glyoxal ($C_2H_2O_2$) revealed a zero phonon line with a broad wing to the red due to particle-hole pair excitations.[26] A small sharp peak superimposed on the wing was attributed to vibrations of the snowball shell of ^{3}He surrounding the molecule.

Here we report on the first detailed calculations of the structure and energy levels of small clusters of ^{3}He atoms attached to the highly *anisotropic* OCS molecule. In the past a number of density functional (DF) calculations have been reported for the radial density distribution of pure ^{3}He droplets[27–29] and the surface distortion produced by partly solvated metal atoms.[25,30,31] The present calculations may be looked upon as an extension of earlier DF calculations for rare gas atoms and the spherical SF_6 molecule, immersed in the interior of small ^{3}He clusters,[32] to an *anisotropic* foreign molecule.

The article starts with a description of the $T = 0$ density functional theory used. For a single attached ^{3}He atom the energy levels for the 19 lowest bound states and the density distributions for the six lowest σ-states are calculated by solving the Schrödinger equation. The Kohn-Sham energy levels of the lowest occupied and some of the unoccupied states indicate that unlike $N = 6$, the $N = 8$, 18, and 40 clusters have closed shells and correspond to the only magic number sizes. The anisotropic density distributions are reported for $N = 8$, 18, and 40 and compared with similar calculations for the same sized bosonic ^{4}He clusters. As with the ^{4}He atoms there is an increase of the density at the donut position, but the atoms are more uniformly distributed over the surface of the chromophore. The moments of inertia are analyzed and compared and found to be reasonably consistent with the recent analysis of OCS rotational spectra in large ^{3}He droplets. The article closes with a discussion of the differences between fermionic and bosonic clusters.

II. DENSITY FUNCTIONAL THEORY

The OCS-^{3}He$_N$ complex is analyzed here within a finite-range density functional framework. The main ingredients are the He-OCS *ab initio* interaction potentials of Paesani and Whaley[5] and the density functional previously used[33] to describe pure ^{3}He droplets. The axisymmetric He-OCS potential energy surfaces reported by Paesani and Whaley were obtained from fourth-order Möller-Plesset perturbation theory. We used their VMP4$_{eq}$ potential, which corresponds to the OCS equilibrium geometry.[5] This potential like all the other potentials has its global minimum perpendicular to the OCS axis centered between the O and C atoms in what is called the donut ring position. Two other weaker local minima are located at the two ends of the linear molecule.

In the present calculations of OCS@^{3}He$_N$ complexes the OCS molecule enters into the calculations only via the anisotropic OCS-He interaction, i.e., the molecule itself is treated as an external potential acting on the ^{3}He$_N$ droplet. Thus the total energy E of a complex is written as

$$E[\rho,\tau] = \int \mathrm{d}\mathbf{r}\,\{\mathcal{E}(\rho,\tau) + V_{\mathrm{He-OCS}}(\mathbf{r})\,\rho(\mathbf{r})\}\,. \quad (1)$$

In this expression $\mathcal{E}(\rho,\tau)$ is the ^{3}He energy density functional of Ref. 33, which is written in terms of the ^{3}He particle and kinetic energy densities $\rho(\mathbf{r})$ and $\tau(\mathbf{r})$ as

$$\mathcal{E}(\rho,\tau) = \frac{\hbar^2}{2m_3^*(\mathbf{r})}\tau(\mathbf{r}) + \frac{1}{2}c\rho^2(\mathbf{r})\tilde{\rho}^\gamma(\mathbf{r}) + \frac{1}{2}\int \mathrm{d}\mathbf{r}'\,\rho(\mathbf{r})V_{LJ}(|\mathbf{r}-\mathbf{r}'|)\rho(\mathbf{r}')\,. \quad (2)$$

The first term is the kinetic energy with an effective ^{3}He mass

$$m_3^*(\mathbf{r}) = m_3\left(1 - \frac{\tilde{\rho}(\mathbf{r})}{\rho_c}\right)^{-2}, \quad (3)$$

where ρ_c is a constant listed below and $\tilde{\rho}(\mathbf{r})$ is a coarse-grained density as introduced in the study of classical fluids,[34] defined by

$$\tilde{\rho}(\mathbf{r}) = \int \mathrm{d}\mathbf{r}'\,\rho(\mathbf{r}')w(|\mathbf{r}-\mathbf{r}'|)\,, \quad (4)$$

with

$$w(r) = \frac{3}{4\pi h^3}, \quad r \le h, \qquad = 0, \quad r < h. \quad (5)$$

The second term in Eq. (2) describes short-range correlations and the third term is a truncated Lennard-Jones potential, which accounts for the long range interaction between the He atoms

$$V_{LJ}(r) = 4\varepsilon\left[\left(\frac{\sigma}{r}\right)^{12} - \left(\frac{\sigma}{r}\right)^{6}\right], \quad r > h, \qquad = 0, \quad r \le h. \quad (6)$$

The same parameter values obtained earlier were used:[33] $\rho_c = 0.0406$ Å^{-3}, $\varepsilon = 10.22$ K, $\sigma = 2.46$ Å, $\gamma = 2.1251$, $c = 1.55379 \times 10^6$ K Å$^{3+3^*\gamma}$, $h = 2.1131$ Å.

The ^{3}He particle and kinetic energy densities $\rho(\mathbf{r})$ and $\tau(\mathbf{r})$, respectively, are expressed in terms of the Kohn-Sham (KS) single-particle (s.p.) orbitals $\phi_i(\mathbf{r})$

$$\rho(\mathbf{r}) = \sum_i n_i \, |\phi_i(\mathbf{r})|^2, \tag{7}$$

$$\tau(\mathbf{r}) = \sum_i n_i \, |\nabla\phi_i(\mathbf{r})|^2, \tag{8}$$

where the n_i are the occupation numbers. To account for spin pairing each of the $\phi_i(r)$ are occupied by two atoms. We have self-consistently solved the Euler-Lagrange equations that result from the variations of Eq. (1) with respect to the ^{3}He normalized s.p. orbitals

$$\frac{\delta}{\delta\phi_i^*}\left(E[\rho,\tau] - \sum_j \epsilon_j |\phi_j|^2\right) = 0, \tag{9}$$

resulting in

$$-\nabla\frac{\hbar^2}{2\,m_3^*}\nabla\phi_i + \left\{\frac{\delta\mathcal{E}}{\delta\rho} + V_{\mathrm{He-OCS}}\right\}\phi_i = \epsilon_i\phi_i, \tag{10}$$

where ϵ_i is the ith ^{3}He s.p. energy.

Equation (10) has been solved by discretizing the derivatives with 13-point formulas. An imaginary time method in conjunction with a Gram-Schmidt orthonormalization procedure was employed to determine the eigenfunctions and eigenvalues.[35] In previous investigations[36,37] we chose to work in a three-dimensional cartesian grid, ignoring the obvious axial symmetry of the system. The rationale for this procedure is that the non-local terms in the functional—i.e., convolution integrals—can be computed more efficiently in such a grid using fast Fourier transform techniques.[38] In the present case we have chosen a mixed approach in which the KS orbitals (and thus the particle and kinetic energy densities) are computed in a two-dimensional, axially symmetric grid with integration steps of $\Delta r = \Delta z = 0.35$ Å. We then interpolate the values of the particle and kinetic energy densities to map the bidimensional cylindrical grid into a three dimensional cartesian one. This mixed approach is useful for fermionic systems where a large number of KS orbitals is involved but only the convolution of the total density is needed and it has the advantage that the computation is much faster due to the lower dimension of the grid. It also allows to assign a well-defined orbital angular momentum l_z to every s.p. state, guaranteeing that states with different value of l_z are orthogonal; nevertheless a Gram-Schmidt procedure is required for all states with the same l_z value. Besides the twofold spin degeneracy of every s.p. state, we recall that the $\pm l_z$ orbitals are also doubly degenerate. Consequently, states with $l_z = 0$ are twofold spin degenerate and those with $l_z \neq 0$ are fourfold degenerate. Throughout, Greek letters $\sigma, \pi, \delta\ldots$ will be used to denote states with $|l_z| = 0, 1, 2\ldots$.

Although the primary concern of this work is the description of fermionic ^{3}He complexes, it is interesting to make a comparison with the bosonic ones with the same number of helium atoms and calculated along similar lines. To this end, we have used a slightly modified version of the Orsay-Trento (OT) functional,[39] usually employed for ^{4}He droplets. The original OT functional contains two terms of the form $\rho\tilde{\rho}^2$ and $\rho\tilde{\rho}^3$, which look similar to the term $\rho^2\tilde{\rho}^\gamma$ entering the density functional for ^{3}He given in Eq. (2), except that the latter contains a squared bare density ρ^2 in place of a linear bare density. This makes some difference for doped helium clusters, since a "squared" density term yields stable results whereas for very attractive impurities a "linear" one does not. Consequently, we have replaced the two mentioned terms by the new ones $\rho^2\tilde{\rho}$ and $\rho^2\tilde{\rho}^2$, keeping the same original parameters. This modified OT functional has also been successfully used for studying the solvation of several ionic impurities in bulk liquid ^{4}He.[40]

We restrict our cluster calculations to the sizes $N = 6$, 8, 18, and 40 of which the last three were found to be the only closed shell magic numbers in this size region along with $N = 2$, which we decided not to include because of the large error introduced by the self-interaction in such a small cluster. The same magic numbers were found earlier for the strongly interacting spherical noble gas atoms Kr and Xe and for SF_6.[32] For the less strongly interacting atoms Ne and Ar an additional magic number was found with $N = 20$. These magic clusters are characterized by the existence of a clear energy gap between the last occupied and the first unoccupied levels, so that the Fermi energy can be unambiguously defined as the highest single-particle energy of the occupied orbitals. In that case the density of the cluster is represented by a single Slater determinant of Kohn-Sham orbitals. Non-magic clusters are instead characterized by a quasi-degeneracy of the highest occupied and lowest unoccupied single particle levels, so that there is some ambiguity in the attribution of the occupied levels.

III. RESULTS

A. Energies and densities of the OCS-^{3}He dimer

As a first step towards understanding the OCS@^{3}He$_N$ clusters, we discuss first the $N = 1$ case. With only a single ^{3}He atom the structure provides insight into the effect of the large zero point energy of the light particle on its localization in the anisotropic potential. The Schrödinger equation for a ^{3}He atom in the anisotropic OCS-^{3}He interaction potential was solved numerically. There are only 19 bound levels, whose energies are listed in Table I. Because of the spin- and l_z-degeneracy mentioned above the 19 levels correspond to altogether 64 bound states. The energy levels are plotted in Fig. 1 as a function of l_z^2. The first band of $n = 1$ states increases linearly with l_z^2, as expected for the increased rotational energies of the highly localized ring-shaped bands.[41] For $n > 1$ the curves bend over with increasing l_z^2.

The probability density distribution of the σ states is shown in Fig. 2. The first three states are situated in each of the three lowest minima of the anisotropic potential. The 1σ state is highly localized at the global minimum in the donut ring position between the O and C atoms. The next highest 2σ state is spread out at the O end of the molecule over a wide angular range corresponding to the wide potential minimum.[5] The 3σ state is more localized in the narrow angular region of the slightly deeper well at the S end. The higher energy σ

TABLE I. Energies and spin degeneracies of the 19 bound states of the OCS@^{3}He complex.

State	Degeneracy	Energy (K)	State	Degeneracy	Energy (K)
1σ	2	−21.215	3π	4	−5.214
1π	4	−20.543	1η	4	−5.082
1δ	4	−18.539	5σ	2	−3.760
1ϕ	4	−15.243	4π	4	−3.562
1γ	4	−10.720	3δ	4	−2.894
2σ	2	−9.583	2ϕ	4	−2.772
2π	4	−8.225	6σ	2	−1.104
3σ	2	−7.955	5π	4	−0.714
4σ	2	−6.323	4δ	4	−0.308
2δ	4	−5.887			

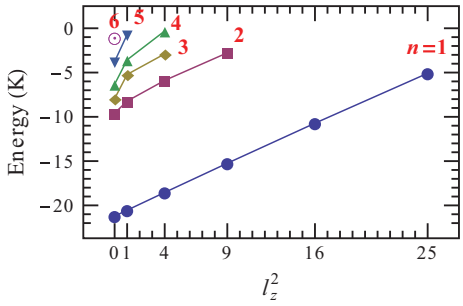

FIG. 1. Energies of the 19 single-particle bound states found for the OCS-^{3}He complex.

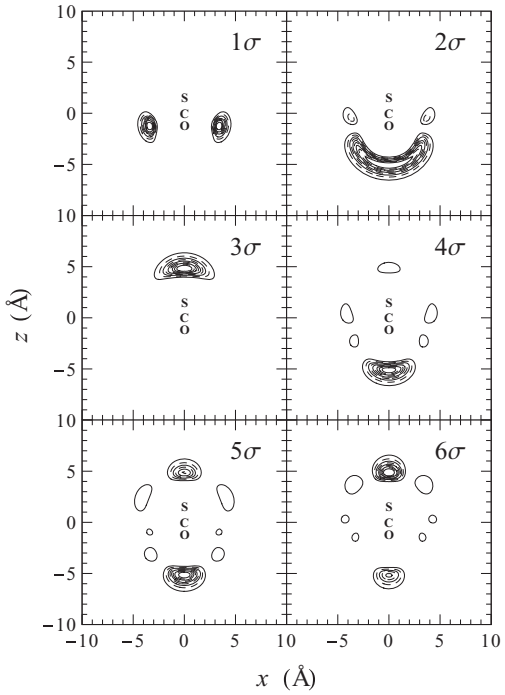

FIG. 2. Probability density of the σ states. In each frame, the contour lines follow the points where the probability density equals 0.1, 0.2, 0.3, ...0.9 times the maximum probability density for that state. Solid lines (for odd fractions 0.1, 0.3, etc.) and dashed lines (for even fractions 0.2, 0.4, etc.) are used to distinguish adjoining contours.

states are more delocalized and more uniformly spread over the entire "surface" of the molecule. The probability distributions for the $l_z \neq 0$ states (not shown) are qualitatively similar to the $l_z = 0$ states with the same main quantum numbers (i.e., 2π, 2δ, etc. are similar to 2σ) except they all have zero probability at the symmetry axis due to centrifugal distortion.

B. Energies and densities of selected OCS-^{3}He clusters

In this subsection we present and discuss the results obtained for complexes with $N = 6$, 8, 18, and 40. One could be tempted to consider an extreme independent-particle approach in which a Slater determinant is constructed from the previously determined states with $N = 1$, hoping that the particle density would roughly reproduce that of the OCS@^{3}He$_N$ complex. However, the strong He–He correlations and the intricate topology of the He-OCS interaction combine to critically affect the shape of the KS orbitals and their ordering as N increases.

The single-particle energy levels for these selected sizes are shown in Fig. 3. No shell closure can be assigned to the size $N = 6$, since the energy gap between the last occupied 1π and the first unoccupied 2σ state is smaller than the energy differences between adjacent states. In contrast, for the sizes 8, 18, and 40 the occupied orbitals are energetically well separated from the unoccupied orbitals, much more than for any other $N \leq 40$ size. This distinct energy gap defines a clear shell closure and the corresponding magic sizes in the $N = 1 - 40$ interval.

The total energies of the doped and pure ^{3}He clusters are listed in Table II where they are compared with the same sized ^{4}He clusters. In the case of the ^{3}He clusters it is only possible to compare the energy of the doped cluster with the energy of the pure cluster for $N = 40$ since clusters with less than about $N \simeq 30$ ^{3}He atoms are not bound.[42–44] As a result, the OCS solvation energy, defined as the difference of the cluster energies with and without the impurity, is the same as the total energy for $N = 6$, 8, 18. For $N = 40$ it is −261.5 K, which is only slightly less than the energy of the doped

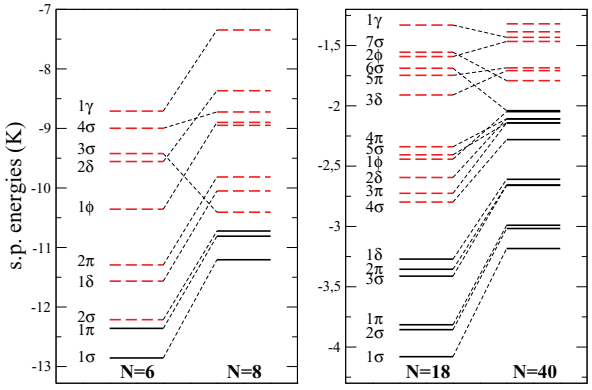

FIG. 3. Single-particle energy levels obtained for OCS@^{3}He$_N$ complexes with $N_3 = 6$, 8, 18, and 40. Solid and dashed lines refer to occupied and unoccupied states, respectively.

TABLE II. DF total energies and solvation energies (in K) of OCS@^{3}He$_N$ and OCS@^{4}He$_N$, and of pure ^{3}He$_N$ and ^{4}He$_N$ clusters.

	OCS@^{3}He$_N$		Pure ^{3}He$_N$		Solv. energy	OCS@^{4}He$_N$		Pure ^{4}He$_N$		Solv. energy	
N	E_3	E_3/N	E_3	E_3/N	ΔE_3	E_4	E_4/N	E_4	E_4/N	ΔE_4	$\Delta E_4/\Delta E_3$
1	−21.2	−21.2	...	...	−21.2	−25.5	−25.5	$\simeq 0$	$\simeq 0$	−25.5	1.20
6	−129.3	−21.6	...	...	−129.3	−145.9	−24.2	−1.5	−0.25	−144.4	1.12
8	−151.2	−18.9	...	...	−151.2	−170.0	−21.3	−4.2	−0.53	−165.8	1.10
18	−217.9	−12.1	...	...	−217.9	−271.7	−15.1	−26.7	−1.5	−245.0	1.12
40	−266.9	−6.7	−5.4	−0.14	−261.5	−378.6	−9.5	−100.3	−2.5	−278.3	1.06

cluster. As explained in Sec. II for comparison with the same sized ^{4}He cluster, which is treated as a superfluid, we have used the slightly modified OT density functional.[39] In Table II are also listed the calculated DF energies of same sized doped and pure ^{4}He clusters. The solvation energies in ^{4}He clusters are only slightly larger in magnitude by about 10% than in the ^{3}He clusters. Since the potentials are identical in the two isotopes this is consistent with the relatively small differences in the structures of the clusters in the two isotopes as discussed in detail below.

The ^{3}He density probability distributions for the ground state complexes with $N = 1$ (1σ), 8, 18, and 40 are shown in Fig. 4 where they are compared with the corresponding ^{4}He cluster distributions. The $N = 40$ ^{4}He density distribution is in reasonable agreement with the one obtained by Kwon and Whaley[8] for $N = 39$ within a path integral Monte Carlo calculation at a temperature of 0.31 K. Figure 5 provides a perspective view of the probability densities for ^{3}He and ^{4}He clusters with $N = 40$ atoms.

As the number of He atoms increases they start to spread more uniformly around the OCS and eventually completely surround the molecule. This behaviour is very similar in both isotopes and the overall differences between the ^{3}He and ^{4}He density distributions in Fig. 4 are surprisingly small. This is probably due to the much greater force exerted by the OCS molecule on the surrounding He atoms which dominates over the forces between the He atoms. The interatomic potentials for the two isotopes are identical and their interactions are affected only by the differences in the zero point energies and in the Fermi repulsion resulting from the different statistics.

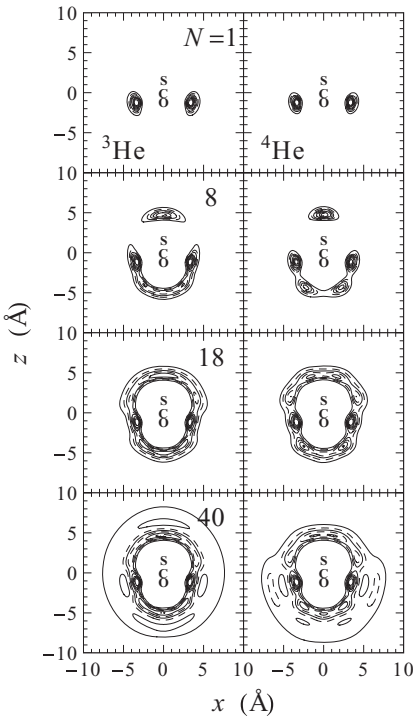

FIG. 4. One-body densities of helium atoms in OCS@^{3}He$_N$ (left panels) and OCS@^{4}He$_N$ (right panels) clusters with $N = 1$, 8, 18, 40. In each frame, the contour lines follow the points where the density equals 0.1, 0.2, 0.3, ...0.9 times the maximum density for that droplet. Solid and dashed lines are used to distinguish adjoining contours.

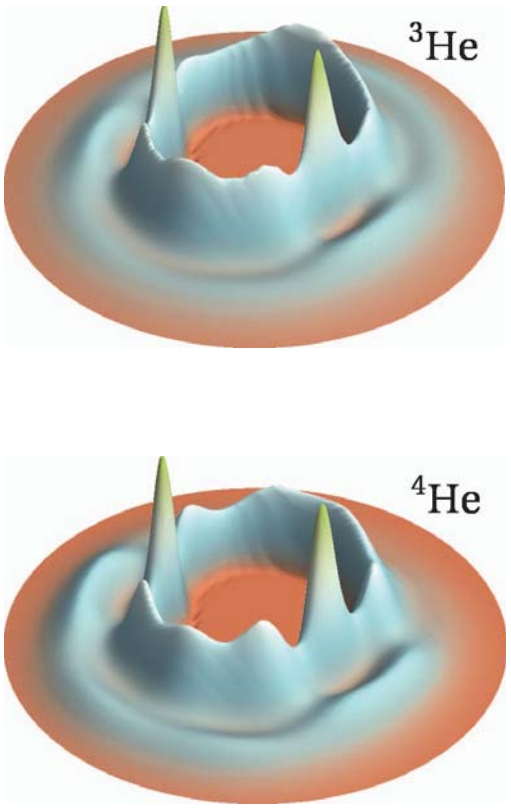

FIG. 5. Three-dimensional visualization of the densities of Fig. 4 for $N = 40$.

Thus in the bosonic clusters there is a higher accumulation of atoms around the different minima of the potential and an overall more asymmetric density shape which follows more closely the potential contours than in the fermionic clusters. The tendency of the ^{3}He orbitals to avoid each other and reduce their mutual repulsion is best seen with the $N = 40$ cluster. With increasing number of atoms the large mean-field effects not only cause the KS energy levels to bunch together but also smear out the distribution of atoms so that they become more spherical.

To determine the number of helium atoms in the donut ring where the OCS-He potential has its absolute minimum, one could simply integrate the He density around the donut. But in practice there are two main difficulties. First, the definition of the "donut region" is somewhat arbitrary and second, the integration method used is not accurate enough to compute integrals in such a small region. An alternative estimate is to use the $N = 1$ probability density as a "guide density" to define the donut region. We assume that if there are λ_N atoms around the potential minimum, the density in that region is going to be roughly similar to $\lambda_N \rho_1$, where ρ_N stands for the particle density of ^{3}He in the OCS-^{3}He$_N$ cluster. Therefore, to determine the number of atoms λ_N in the donut of an N-sized cluster we minimize the quantity

$$\varepsilon(\lambda_N) = \int d\mathbf{r}\left\{\rho_N(\mathbf{r}) - \lambda_N \rho_1(\mathbf{r})\right\}^2, \tag{11}$$

which gives the solution

$$\frac{d\varepsilon}{d\lambda_N} = 0 \quad \rightarrow \quad \lambda_N = \frac{\int d\mathbf{r}\rho_N(\mathbf{r})\rho_1(\mathbf{r})}{\int d\mathbf{r}\rho_1^2(\mathbf{r})}. \tag{12}$$

The resulting λ_N turns out to be 4.05 ($N = 8$), 4.18 ($N = 18$), and 4.30 ($N = 40$). Thus more than 4 ^{3}He atoms are located in the donut rings compared to 5 for the smallest ^{4}He clusters and 6 atoms in larger ^{4}He clusters and droplets.

C. Moment of inertia of the clusters

The distribution of He atoms around the OCS molecule is of interest in connection with the rotational properties of the complexes. For fermions in the normal (non-superfluid) phase, the proper method for calculating the MOI within DFT is provided by the cranking formula which is obtained by applying a classical crank rotating with angular velocity ω to the deformed cluster around an axis perpendicular to the symmetry, x axis, for instance. This is known as the Inglis model in nuclear physics[45,46] and the resulting expression can alternatively be obtained with the one-particle operator $\omega \cdot L_x$ using first order perturbation theory. In this model only one particle-hole pair is excited at a time and the model thus holds within the KS approach. Fortunately the Inglis formula provides values for the MOI that are very close to the rigid body value.[45,46] For this reason, we have assumed the He distribution to behave as a rigid solid and calculated the cluster MOI as

$$I_{ij} = m_{\mathrm{He}} \int d\mathbf{r}\rho(\mathbf{r})\left(r^2\delta_{ij} - r_i r_j\right) + I_{ij}^{OCS}. \tag{13}$$

Because of the axial symmetry of the densities all non-diagonal elements of this matrix vanish and only the $I_{11} = I_{22} = I_b$ and $I_{33} = I_a$ terms survive. The intrinsic MOI of the isolated molecule are $I_b^{OCS} = 83$ amu Å^2 and $I_a^{OCS} = 0$.[47]

TABLE III. Comparison of the moments of inertia (in amu Å^2) calculated from the He distributions, considered to be rigid, with the experimental values of the free molecules and measured in large droplets.

N	I_a (^{3}He)	I_a (^{4}He)	I_b (^{3}He)	I_b (^{4}He)
Free mol.	0	0	83[a]	83[a]
8	268	276	131	383
8(expt.)	...	...	...	348[b]
18	957	815	1129	1028
18(expt.)	...	...	...	230[c]
40	3850	3079	4096	3123
40 (expt.)	...	...	...	215[c]
Large droplets(expt.)	≤80 or 240[d]	...	≈500[b]	230[e]

[a]Reference 48.
[b]Calculated from values of "B" listed in Ref. 4.
[c]Reference 11.
[d]Reference 15.
[e]Reference 3.

Table III lists the MOI values for OCS attached to $N = 8$, 18, and 40 ^{3}He and ^{4}He clusters calculated using Eq. (13) from the density functional distributions and compares them with the available experimental results. These are only available for I_b of small ^{4}He clusters.[4,11] The large discrepancies between the rigid ^{4}He clusters with $N = 18$ and 40 and the experimental results have been explained by assuming that the chromophore, together with about 5 or 6 tightly attached atoms in the donut ring, undergoes end-over-end rotations independently of all the other atoms of the cluster. Thus the effective MOI, which depending somewhat on cluster size, lies between 215 and 348 amu Å^2, is much smaller than calculated for the entire rigid cluster. The difference is attributed to an effect of microscopic superfluidity, which is not accounted for in the present calculations.[4,11] As mentioned in the introduction values for the axial MOI I_a are not available since the donut rotations are not activated at the low temperatures of the clusters. The same considerations apply to large droplets, for which I_a could also not be determined from the spectra.

In the case of the ^{3}He clusters, for which superfluid effects are not expected, the present calculations can only be compared with the results measured in large droplets.[15] Because of the largely unresolved broad features of the spectrum, 8 different models were tested by comparing the least square best fits of each with the measured spectrum. The models assumed either a linear rotor or a symmetric top structure, a fixed droplet temperature or a best fit temperature and either a Gauss or a Lorentz profile for the rotational lines. The conclusion drawn from the analysis of the 4 symmetric top models, which come closest to the structure obtained in the present study, in three cases was that the axial moment of inertia I_a is less than 80 amu Å^2 and only in one case was $I_a = 240$ amu Å^2. All 8 models led to values for I_b between 620 and 413 amu Å^2 averaging to about 500 amu Å^2. From this value it was estimated, based on an *ad hoc* assumption of a spherical shell, which is consistent with a symmetric top model, that roughly 11 attached ^{3}He atoms are co-rotating with the OCS molecule independent of the other atoms in the droplet. A difficulty with this interpretation was that a spheri-

cal shell implies $I_a \approx 350$ amu Å^2 which is significantly larger than even the only comparable large value obtained assuming a symmetric top structure. Although the present predicted value for $N = 8$ ($I_a = 268$ amu Å^2) is already somewhat larger than the best fit value of 240 amu Å^2 it is gratifying that the spherical shell value of $I_a \approx 350$ amu Å^2 lies between the present calculated values for $N = 8$ and 18. Since also the average experimental value of $I_b = 500$ amu Å^2 lies between the present values for $N = 8$ and $N = 18$ we conclude that the present calculations are reasonably consistent with the 11 atom spherical shell structure considered to be the most likely structure by the experimentalists.

It is surprising, however, that the experimental value for I_b does not coincide with a magic number. The fact that the experimental number of 11 differs significantly from the two nearest magic numbers suggests that perhaps the transition between co-rotating and decoupled atoms is a gradual one. Finally we note that the argument used to explain the missing Q-branch in ^{4}He clusters does not apply to ^{3}He clusters. In the latter case the fermionic statistics allows the axial rotations to be excited even at the very low temperatures (≈0.1 K) of the droplets as outlined in the appendix of Ref. 15. In this respect the experiment also lends support to the symmetric top (and spherical shell) model since it is the only one which predicts the presence of a Q-branch in the experimental spectrum.

Thus these calculations largely clarify the differences between the solvation shells for the two isotopes. In the bosonic ^{4}He droplets the attached atoms are compactly localized in the donut ring which can accommodate at most 6 atoms while the others are completely decoupled from the rotations as is currently attributed to the phenomenon of microscopic superfluidity. The co-rotating He atoms are attributed to a non-superfluid fraction, which are "adiabatically following"[10] the rotations of the chromophore in contrast to the other atoms which are superfluid. In the fermionic ^{3}He droplets the co-rotating shell contains more atoms and is only partly localized in the donut position, and therefore is more spread out. Moreover the surrounding atoms and their collective excitations interact more strongly with the rotating complex.[19] The attached solvation shell is however also decoupled from the rest of the ^{3}He droplet even though it is certainly not superfluid.

IV. DISCUSSION

The present calculations of the MOI involve a number of assumptions in addition to those inherent in density functional theory. Foremost for the interpretation of the OCS-^{3}He-droplet spectra is the assumption of a rigid cluster with a fixed size, which rotates without interacting with its environment. This model must be considered to be highly idealized in view of the large viscosity of ^{3}He (200 micropoise at 0.1 K) which is largely responsible for the large line widths in the experimental spectrum. The present theory also neglects the effect of the translations and rotations of the chromophore on the density distributions. In the case of small ^{4}He clusters this has been investigated for a number of chromophores including OCS.[8,48,49] The density becomes somewhat more spread out and delocalized and the moment of inertia is slightly increased.[49] In the present case a dynamic quantum Monte Carlo simulation would be required to more accurately estimate the size of the cluster which rotates together with the chromophore molecule. Such a calculation or even a simple classical model would also have to account for the large viscosity of the ^{3}He liquid.

Finally, we comment briefly on the future prospects of carrying out *ab initio* calculations of small doped ^{3}He clusters. Our experience in the present study indicates that the extreme independent-particle approach, which has been so helpful in nuclear physics, fails to properly predict the atom shell filling. This is largely due to the strong helium-helium interaction and the neglect of Fermi statistics; both aspects which are incorporated in the DF approach used here. Jungwirth and Krylov[50] were the first to call attention to the close analogy between the quantum chemistry theory of atoms and molecules and that of ^{3}He atoms attached to heavy chromophores. The electron-electron Coulomb repulsion is replaced by the ^{3}He-^{3}He van der Waals potential and the Coulomb attraction to the nucleus by the strong van der Waals attraction between the ^{3}He atoms and the chromophore. Following this analogy, a full-configuration-interaction nuclear-orbital implementation has been developed and applied by de Lara-Castells and collaborators[52,52,53] to study ground- and excited-state properties of doped clusters containing up to four ^{3}He atoms. However, because of the weakly attractive long range and strongly repulsive short range interaction of the He atoms, very large basis sets were required in order to get satisfactory results for larger systems. Finally we note that a diffusion Monte Carlo calculation, which has been employed in the past to study both pure and doped ^{3}He clusters,[43,44,54,55] can be used to study larger clusters up to several tens of atoms. Work along these lines is now in progress.

ACKNOWLEDGMENTS

This work has been supported by 2009SGR1289 from Generalitat de Catalunya, FIS2011-28617-C02-02 from DGI, Spain. We thank Manuel Barranco for many discussions, suggestions, and comments about this paper, Francesco Paesani and Birgitta Whaley for providing us with their OCS-He interaction, Pilar de Lara-Castells for clarifying comments about her theory, Robert McKellar for correspondence, and Boris Sartakov for reading and commenting on the paper.

[1] See the articles in "Special topic issue: Helium nanodroplets—A novel medium for chemistry and physics," J. Chem. Phys. **115**(22) (2001); online at http://jcp.aip.org/resource/1/jcpsa6/v115/i22.
[2] J. P. Toennies and A. F. Vilesov, Angew. Chem., Int. Ed. **43**(20), 2622 (2004).
[3] S. Grebenev, M. Hartmann, M. Havenith, B. Sartakov, J. P. Toennies, and A. F. Vilesov, J. Chem. Phys. **112**, 4485 (2000).
[4] J. Tang and A. R. W. McKellar, J. Chem. Phys. **119**, 5467 (2003).
[5] F. Paesani and K. B. Whaley, J. Chem. Phys. **121**, 4180 (2004).
[6] Y. Xu and W. Jaeger, J. Chem. Phys. **119**, 5457 (2003).
[7] S. Moroni, A. Sarsa, S. Fantoni, K. E. Schmidt, and S. Baroni, Phys. Rev. Lett. **90**, 143401 (2003).
[8] Y. Kwon and K. B. Whaley, J. Chem. Phys. **115**, 10146 (2001).
[9] F. Paesani, F. A. Gianturco, and K. B. Whaley, J. Chem. Phys. **115**, 10225 (2001).

[10]Y. Kwon, P. Huang, M. V. Patel, D. Blume, and K. B. Whaley, J. Chem. Phys. **113**(16), 6469 (2000).
[11]A. R. W. McKellar, Y. Xu, and W. Jäger, J. Phys. Chem. A **111**, 7329 (2007).
[12]A. R. W. McKellar, Appl. Phys. B **90**, 213 (2008).
[13]S. Grebenev, B. Sartakov, J. P. Toennies, and A. Vilesov, Phys. Rev. Lett. **89**(22), 225301 (2002).
[14]A. Guirao, M. Pi, and M. Barranco, Z. Phys. D **21**(2), 185 (1991).
[15]B. Sartakov, J. P. Toennies, and A. Vilesov, J. Chem. Phys. **136**, 134316 (2012).
[16]D. M. Brink and S. Stringari, Z. Phys. D: At., Mol. Clusters **15**, 257 (1990).
[17]M. Hartmann, N. Pörtner, B. Sartakov, J. P. Toennies, and A. F. Vilesov, J. Chem. Phys. **110**, 5109 (1999).
[18]S. Grebenev, J. P. Toennies, and A. F. Vilesov, Science **279**(5359), 2083 (1998).
[19]V. S. Babichenko and Y. Kagan, Phys. Rev. Lett. **83**(17), 3458 (1999).
[20]S. Grebenev, N. Pörtner, A. F. Vilesov, M. Hartmann, A. Lindinger, E. Lugovoi, J. P. Toennies, and B. Sartakov, *Proceedings of the Nobel Symposium 117: The Physics and Chemistry of Clusters* (World Scientific, Singapore, 2001).
[21]K. von Haeften, T. Laarmann, H. Wabnitz, and T. Möller, Phys. Rev. Lett. **88**, 233401 (2002).
[22]F. Stienkemeier, O. Bunermann, R. Mayol, F. Ancilotto, M. Barranco, and M. Pi, Phys. Rev. B **70**, 214509 (2004).
[23]O. Bünermann, G. Droppelmann, A. Hernando, R. Mayol, and F. Stienkemeier, J. Phys. Chem. A **111**, 12684 (2007).
[24]O. Bünermann, M. Dvorak, F. Stienkemeier, A. Hernando, R. Mayol, M. Pi, M. Barranco, and F. Ancilotto, Phys. Rev. B **79**, 214511 (2009).
[25]A. Hernando, R. Mayol, M. Pi, M. Barranco, F. Ancilotto, O. Bunermann, and F. Stienkemeier, J. Phys. Chem. A **111**, 7303 (2007).
[26]N. Pörtner, J. P. Toennies, A. F. Vilesov, G. Benedek, and W. Hizhnyakov, Europhys. Lett. **88**, 26007 (2009).
[27]S. Weisberger and P. G. Reinhard, Z. Phys. D: Atoms, Molecules and Clusters **23**, 275 (1992).
[28]M. Barranco, D. M. Jezek, E. S. Hernández, J. Navarro, and Ll. Serra, Z. Phys. D: At., Mol. Clusters **28**, 257 (1993).
[29]J. Harms, J. P. Toennies, M. Barranco, and M. Pi, Phys. Rev. B **63**, 184513 (2001).
[30]A. Hernando, M. Barranco, R. Mayol, M. Pi, and F. Ancilotto, Phys. Rev. B **78**, 184515 (2008).
[31]D. Mateo, M. Barranco, R. Mayol, and M. Pi, Eur. Phys. J. D **52**, 63–66 (2009).
[32]F. Garcias, Ll. Serra, M. Casas, and M. Barranco, J. Chem. Phys. **108**, 9102 (1998).
[33]M. Barranco, M. Pi, S. M. Gatica, E. S. Hernández, and J. Navarro, Phys. Rev. B **56**, 8997 (1997).
[34]P. Tarazona, Phys. Rev. A **31**, 2672 (1985).
[35]F. Ancilotto, D. G. Austing, M. Barranco, R. Mayol, K. Muraki, M. Pi, S. Sasaki, and S. Tarucha, Phys. Rev. B **67**, 205311 (2003).
[36]D. Mateo, D. Jin, M. Barranco, and M. Pi, J. Chem. Phys. **134**, 044507 (2011).
[37]M. Pi, R. Mayol, A. Hernando, M. Barranco, and F. Ancilotto, J. Chem. Phys. **126**, 244502 (2007).
[38]M. Frigo and S. G. Johnson, Proc. IEEE **93**, 216 (2005).
[39]F. Dalfovo, A. Lastri, L. Pricaupenko, S. Stringari, and J. Treiner, Phys. Rev. B **52**, 1193 (1995).
[40]S. L. Fiedler, D. Mateo, T. Aleksanyan, and J. Eloranta, Phys. Rev. B **86**, 144522 (2012).
[41]R. Mayol, M. Barranco, E. S. Hernández, M. Pi, and M. Guilleumas, Phys. Rev. Lett. **90**, 185301 (2003).
[42]M. Barranco, J. Navarro, and A. Poves, Phys. Rev. Lett. **78**, 4729 (1997).
[43]R. Guardiola and J. Navarro, Phys. Rev. A **71**, 035201 (2005).
[44]E. Sola, J. Casulleras, and J. Boronat, Phys. Rev. B **73**, 092515 (2006).
[45]A. de Shalit and H. Feshbach, *Theoretical Nuclear Physics* (Wiley, New York, 1974), pp. 415 ff.
[46]P. Ring and P. Schuck, *The Nuclear Many-Body Problem* (Springer, New York, 1980).
[47]H. Hunt, S. C. Foster, J. W. C. Johns, and A. R. W. McKellar, J. Mol. Spectrosc. **111**, 42 (1985).
[48]M. V. Patel, A. Viel, F. Paesani, P. Huang, and K. B. Whaley, J. Chem. Phys. **118**, 5011 (2003).
[49]F. Paesani and K. B. Whaley, J. Chem. Phys. **121**, 5293 (2004).
[50]P. Jungwirth and A. I. Krylov, J. Chem. Phys. **115**, 10214 (2001).
[51]M. P. de Lara-Castells, G. Delgado-Barrio, P. Villareal, and A. O. Mitrushchenkov, J. Chem. Phys. **125**, 221101 (2006).
[52]M. P. de Lara-Castells, N. F. Aguirre, P. Villareal, G. Delgado-Barrio, and A. O. Mitrushchenkov, J. Chem. Phys. **132**, 194313 (2010).
[53]M. P. de Lara-Castells, G. Delgado-Barrio, P. Villareal, and A. O. Mitrushchenkov, Int. J. Quantum Chem. **111**, 406 (2011).
[54]R. Guardiola, J. Navarro, D. Mateo, and M. Barranco, J. Chem. Phys. **131**, 174110 (2009).
[55]J. Navarro, D. Mateo, M. Barranco, and A. Sarsa, J. Chem. Phys. **136**, 054301 (2012).

Chapter 3

Dynamics

3.1 Evolution of the excited electron bubble in liquid ^{4}He and the appearance of fission-like processes

Resumen (Spanish)

Hemos seguido la evolución de una burbuja electrónica excitada en ^{4}He superfluido durante unas decenas de picosegundos combinando el cálculo dinámico del líquido con la evolución adiabática del electrón. El cálculo muestra cómo el camino seguido por la burbuja excitada al estado 1P en su relajación hacia el estado fundamental depende de forma crítica de la presión aplicada. Para presiones inferiores a 1 bar, el electrón puede desexcitarse radiativamente hasta el estado fundamental deformado y evolucionar hacia el auténtico estado fundamental esférico. Para presiones superiores a 1 bar hemos observado que dos "baby bubbles" claramente diferenciadas aparecen en el trascurso de la evolución, lo que apunta a un nuevo camino de relajación en el que el electrón se localiza en una de las dos burbujas mientras la vacía colapsa. Esto permite una relajación puramente no-radiativa.

Nuestros cálculos muestran en buen acuerdo con los experimentos en los que las burbujas electrónicas 1P se detectan solo por debajo de una presión crítica del orden de 1 bar mientras que para presiones más elevadas la relajación de las burbujas sucede por una vía diferente. Un análisis similar de la burbuja 2P muestra que la aproximación adiabática falla en un estadio temprano de la evolución debido al cruce de los estados 2P y 1F.

PHYSICAL REVIEW B **81**, 174510 (2010)

Evolution of the excited electron bubble in liquid ^{4}He and the appearance of fission-like processes

David Mateo, Martí Pi, and Manuel Barranco
Departament ECM, Facultat de Física, and IN2UB, Universitat de Barcelona, Diagonal 647, 08028 Barcelona, Spain
(Received 9 October 2009; revised manuscript received 5 March 2010; published 11 May 2010)

We have studied the evolution of an excited electron bubble in superfluid ^{4}He for several tens of picosecond combining the dynamics of the liquid with an adiabatic evolution for the electron. The path followed by the excited bubble in its decay to the ground state is shown to strongly depend on pressure. While for pressures below 1 bar the 1P excited electron bubble has allowance for radiatively decay to the deformed ground state, evolving then nonradiatively toward the ground state of the spherical electron bubble, we have found that above 1 bar two distinct baby bubbles appear in the course of the dynamical evolution, pointing to a different relaxation path in which the electron may be localized in one of the baby bubbles while the other collapses, allowing for a pure radiationless de-excitation. Our calculations are in agreement with experiments indicating that relaxed 1P bubbles are only observed for pressures smaller than a critical one, on the order of 1 bar, and that above this value the decay of the excited bubble has to proceed differently. A similar analysis carried out for the 2P bubble shows that the adiabatic approximation fails at an early stage of its dynamical evolution due to the crossing of the 2P and 1F states.

DOI: 10.1103/PhysRevB.81.174510 PACS number(s): 47.55.D−, 67.25.du, 33.20.Kf, 71.15.Mb

I. INTRODUCTION

Electron bubbles (ebubbles) in liquid helium are fascinating objects with an apparently simple structure that have been the subject of a large number of experimental and theoretical studies, see, e.g., Refs. 1–12 and references therein. The imaging of individual ebubbles moving in the liquid,[13] some unexplained events in cavitation experiments,[14] and the efforts in creating and detecting multielectron bubbles[15,16] are recent issues calling for a dynamical description of the electron bubble, but not the only ones. For instance, the equilibration of the electron bubble in superfluid liquid helium, studied in detail by Eloranta and Apkarian[8] within time-dependent density-functional (DF) theory, also needed of an accurate dynamical description. The ebubbles addressed in that work are spherically symmetric, which made the calculations affordable for using the best available DF for ^{4}He, the so-called Orsay-Trento functional.[17] Other dynamical studies have resorted to much simpler approaches inspired on local functionals of the kind proposed by Stringari and Treiner long time ago,[18] or on generalizations of the Gross-Pitaevskii equation to the description of liquid helium.[19–22] They have allowed to carry out dynamical studies involving nonspherical ebubbles, and their interaction with vortices in the superfluid. However, these local approaches do not describe the superfluid accurately. In particular, its elemental excitations are poorly reproduced. To circumvent this shortcoming, nonlocal extensions have been proposed[23] and applied, e.g., to vortex nucleation in superfluid helium.[24]

Another problem requiring a dynamical treatment, still not addressed in full detail, is the relaxation of an ebubble after being excited by photoabsorption, which constitutes the subject matter of this work. This process couples the fairly slow displacement of the helium bubble with the rapid motion of the electron it hosts, producing excitations in the liquid that take away a sizeable part of the energy deposited in the ebubble during the absorption. The emission spectrum of the electron bubble after it has relaxed around the excited electron state has been calculated.[10,25,26] However, whether and how these full relaxed configurations are attained before decaying by photoemission was not elucidated.

In this work we attempt a theoretical description of the evolution of the excited ebubble based on the zero-temperature DF approach, using an as much accurate as technically feasible description of the liquid and an electron-helium (e-He) interaction that have been proved to reproduce the experimental absorption energies of the ebubble. The initial configuration is determined by a static calculation of the excited ebubble. This state has a large radiative lifetime, on the order of several tens of microsecond, in contrast with the short time scale for the helium displacement, on the order of picosecond. The subsequent dynamical evolution of the ebubble is described within the adiabatic approximation, which is valid for a period of time difficult to ascertain,[27] that we shall discuss in some detail. We will show that, depending on the initial excited state and the external pressure applied to the liquid, the bubble may keep its initial simply connected topology, or evolve toward a nonsimply connected one made of two baby bubbles that share the probability of finding the electron in,[28] the electron eventually localizing in one of them while the other collapses. To reduce the numerical effort to a reasonable amount, we shall mostly discuss results for the collapse of an ebubble starting from the spherical 1P state. Results for the collapse of the 2P state will be also shown.

This work is organized as follows. In Sec. II we describe our model and present a quasistatic study of the ebubble, completing the results we have presented elsewhere,[25] and recalling some technical details about the method we have used to solve the variational equations for the fluid and the electron. In Sec. III we present the adiabatic evolution of the ebubble for two selected values of the liquid pressure. The validity of the adiabatic approximation is analyzed in Sec. IV and a summary is presented in Sec. V.

II. QUASISTATIC DESCRIPTION

We first address some properties of excited electron bubbles in liquid ^{4}He using the Orsay-Trento density functional including the terms that mimic backflow effects and are crucial to quantitatively reproduce the experimental phonon-roton dispersion relation in bulk liquid ^{4}He at zero pressure.[17] They have no influence on the statics of the system and have been often neglected[12,29] in the dynamics because their inclusion makes the dynamical calculations very cumbersome.[8,30–32] In practice, we have found that these terms have little effect on the dynamics of the electron bubble presented in this work.

The e-He interaction has been modeled by the Hartree-type local effective potential derived by Cheng *et al.*[33] This allows us to write the energy of the electron-helium system as a functional of the electron wave function $\Phi(\mathbf{r})$ and the ^{4}He effective macroscopic wave function $\Psi(\mathbf{r}) = \sqrt{\rho(\mathbf{r})}\exp[\imath S(\mathbf{r})]$, where $\rho(\mathbf{r})$ is the particle density and $\mathbf{v}(\mathbf{r}) = \hbar\nabla S(\mathbf{r})/m_{\mathrm{He}}$ is the velocity field of the superfluid

$$E[\Psi,\Phi] = \frac{\hbar^2}{2m_{\mathrm{He}}}\int d\mathbf{r}|\nabla\Psi(\mathbf{r})|^2 + \int d\mathbf{r}\mathcal{E}(\rho) + \frac{\hbar^2}{2m_e}\int d\mathbf{r}|\nabla\Phi(\mathbf{r})|^2 + \int d\mathbf{r}|\Phi|^2 V_{\text{e-He}}(\rho). \quad (1)$$

In this expression, $\mathcal{E}(\rho)$ is the ^{4}He "potential" energy density and the e-He interaction $V_{\text{e-He}}(\rho)$ is written as a function of the helium density.[33] Details are given in Refs. 9 and 34. In the absence of vortex lines, S is zero and E becomes a functional of ρ and Φ. Otherwise, one has to use the complex wave function $\Psi(\mathbf{r})$ to describe the superfluid.

For a given pressure (P), we have solved the Euler-Lagrange equations which result from the variation with respect to Ψ^* and Φ^* of the zero temperature constrained grandpotential density $\tilde{\omega}(\Psi,\Phi) = \omega(\Psi,\Phi) - \varepsilon|\Phi|^2$, with

$$\omega(\Psi,\Phi) = \frac{\hbar^2}{2m_{\mathrm{He}}}|\nabla\Psi(\mathbf{r})|^2 + \mathcal{E}(\rho) + \frac{\hbar^2}{2m_e}|\nabla\Phi|^2 + |\Phi|^2 V_{\text{e-He}}(\rho) - \mu\rho, \quad (2)$$

where μ is chemical potential of the liquid. The variation of the above functional yields two coupled equations that have to be self-consistently solved

$$-\frac{\hbar^2}{2m_{\mathrm{He}}}\Delta\Psi + \left\{\frac{\delta\mathcal{E}}{\delta\rho} + |\Phi|^2\frac{\partial V_{\text{e-He}}(\rho)}{\partial\rho}\right\}\Psi = \mu\Psi, \quad (3)$$

$$-\frac{\hbar^2}{2m_e}\Delta\Phi + V_{\text{e-He}}(\rho)\Phi = \varepsilon\Phi, \quad (4)$$

where ε is the eigenvalue of the Schrödinger equation obeyed by the electron.

Our method of solving the variational equations is based on a high-order discretization in Cartesian coordinates of the differential operators entering them (13-point formulas in the present case), and the use of fast Fourier transformation techniques[35] to efficiently compute the convolution integrals in $\omega(\rho)$, such as the mean-field helium potential and the coarse-grained density entering the definition of the correlation energy.[12] This allows us to use a large spatial mesh step, of about 1 Å size, without an apparent loss of numerical accuracy when we compare our results with others (see below) obtained using three-point formulas for the derivatives that, as a consequence, require a rather small mesh step to be accurate. The density at the boundary of the three-dimensional $140\times140\times140$ Å^3 box used to carry out the calculations is fixed to the value of the bulk liquid density at the given P. We recall that knowledge of $\mathcal{E}(\rho)$ allows to determine the equation of state of the bulk liquid and its chemical potential, since $\mu = \partial\mathcal{E}/\partial\rho$ and $P = -\mathcal{E}(\rho) + \mu\rho$. Equations (3) and (4) have been solved employing an imaginary-time method,[36] and we have carried out the appropriate tests to check the stability of the solutions. We mention that the energies we have obtained for the $1S\rightarrow1P$ and $1S\rightarrow2P$ transitions[9] are in very good agreement with experiment,[6] and that our results compare well with those obtained by Eloranta and Apkarian[8] using the same functional but a different numerical method and e-He interaction. This constitutes an excellent test not only for the numerics but also for the physical ingredients employed in both calculations. We have recently discussed the effect of the presence of vortices on the absorption spectrum of ebubbles attached to them.[25]

Upon excitation to the 1P state by light absorption, the ebubble experiences a drastic change in shape. This is due to the fairly large radiative lifetime of this state (calculated to be 44 μs in Ref. 26, 60 μs in Ref. 10, and 56 μs in Ref. 25) as compared to any characteristic helium time scale, allowing the liquid to relax around the excited state. As a consequence, the bubble adapts its shape to the 1P electron probability density before decaying by photoemission to the deformed 1S state. Consequently, the bubble configuration at the emission time can be obtained by minimizing the grand-potential of the system keeping the electron in the excited 1P state. We have done it by solving Eqs. (3) and (4) taking for Φ the $\Phi_{1\mathrm{P}}$ wave function. In this case, a Gram-Schmidt scheme has been implemented to determine both 1P and 1S relaxed states that obviously no longer correspond to a spherical bubble. In this axially symmetric environment, the spherical nL states are split depending on the value (m) of the orbital angular momentum on the symmetry z axis, and the $\pm m$ states are degenerate. We have found that, within a nL manifold, the m states are ordered in increasing $|m|$ values.[25] For this reason, we will refer to the axially symmetric state that corresponds to the $m=0$ submanifold when we speak of a deformed "nL" state. When needed, we shall use the conventional notation for the orbital angular momentum of single-particle states in linear molecules, namely, $\sigma,\pi,\delta,\phi,\ldots$ for $|m|=0,1,2,3,\ldots$, and superscripts +(–) for specularly symmetric (antisymmetric) states.

Figure 1 displays quasiequilibrium ebubble configurations at different stages of the absorption-emission cycle obtained at $P=0$ bar. The electron-probability densities are represented by colored clouds, these with one lobe correspond to 1S states (spherical bubble, picture 1; deformed bubble, picture 4) and these with two lobes correspond to 1P states (spherical bubble, picture 2; deformed bubble, picture 3). In this figure, the line indicates the bubble dividing surface, i.e., the surface at which the liquid density equals half the

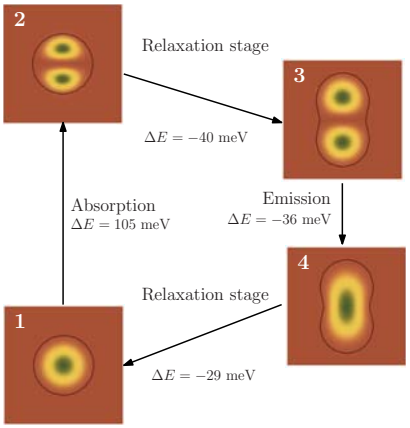

FIG. 1. (Color online) Ebubble quasiequilibrium configurations at different stages of the absorption-emission cycle corresponding to $P=0$ bar. The electron-probability densities are represented by colored clouds. The dashed line is the bubble dividing surface. The size of the frames is 70×70 Å^2.

saturation-density value ρ_0, e.g., 0.0218 Å^{-3} at $P=0$ bar, and represents the surface of the helium bubble. We have found[25] that at $P=0$ bar, the $1P\rightarrow1S$ emission energy is 36 meV, close to the 35 meV found in Ref. 10, constituting another excellent test of the theoretical framework used by us and by these authors. The energy released in the optical 1S-1P absorption-emission cycle can be determined combining the results we have obtained in previous works.[9,25] For instance, at $P=0$ bar the released energy is 69 meV (compare with the 76 meV obtained in Ref. 10). This energy is transferred to the superfluid through generation of different kind of excitations.

Quasiequilibrium configurations of the ebubble relaxed around the 1P state are shown in Fig. 2 for several P values. In this figure, helium is represented by warm colors and the electron-probability density (arbitrary units) by cool colors. The relaxation of the bubble around the 1P state produces a characteristic two-lobe peanut structure whose waist—or neck—is progressively marked as the pressure applied to the liquid increases. Notice that helium displays a stratified density around the bubble. This feature appears whenever the superfluid presents a kind of free surface, as in drops, films or bubbles.[9,17,36]

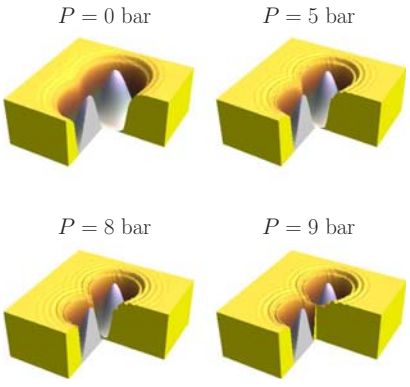

FIG. 2. (Color online) 1P bubble quasiequilibrium configurations for $P=0$, 5, 8, and 9 bars. Helium is represented by warm colors and the electron-probability density (arbitrary scale) by cool colors. The size of the samples is 70×70 Å^2.

Figure 2 shows that at a pressure of ~8 bars helium starts to penetrate between the two lobes of the electron wave function. At ~9 bars the helium density in this region reaches the saturation density, and the bubble splits into two baby bubbles. This produces an abrupt change in the emission energy, falling an order of magnitute between $P=8$ and 9 bars; in the "broken-neck" region extending up to the solidification pressure, the photon-emission energy is barely ~1 meV.[25] This is expectable at these pressures, as the main difference between 1S and 1P probability densities appears in the waist region. If this region is inaccessible to the electron due to the presence of helium, these states become almost degenerate. On the contrary, if this region is not accessible to the superfluid due, e.g., to the presence of a vortex whose vorticity line coincides with the symmetry axis of the ebubble, the baby bubbles may be held together by a tiny neck.[25]

It is worth pointing out that some of the quasiequilibrium configurations displayed in Fig. 2 may not be reachable in the evolution of the bubble. The reason is that helium falling in the waist region during the violent collapse may produce a large pileup of superfluid in that region, thus causing the actual breaking of the neck at pressures much smaller than the 8 bars obtained quasistatically. This possibility has been anticipated by Maris.[2]

III. TIME EVOLUTION OF THE EBUBBLE: PICOSECOND DYNAMICS

The dynamics of the excess electron localization in liquid helium has been adiabatically addressed by Rosenblit and Jortner[37,38] using a sharp-surface model for the bubble. The superfluid was considered as incompressible, and the bubble expansion time, i.e., the time for creating the ebubble, was estimated to be 8.5 ps when energy dissipation by emission of sound waves was taken into account.[38] This process exhibits a marked P dependence, the higher the pressure the shorter the expansion time.

Later on, the incompressibility approximation was relaxed using a DF approach, finding that at $P=0$ bar the bubble surface breathes with a period of about 130 ps.[8] These calculations have revealed that the localization process may launch shock waves, and that the subsequent main dissipation mechanism is sound radiation; excitations in the roton well were not produced.[8] In the present work we consider that the ebubble has had time enough to relax to its spherical 1S ground state and the electron is subsequently excited by light absorption to the 1P state, whose dynamical evolution is the subject matter of this section.

A. Adiabatic time evolution

Since the electron evolves much faster than helium as their mass ratio is $m_{\mathrm{He}}/m_{\mathrm{e}}\simeq7300$, we have followed the dy-

namics of the excited ebubble by combining the actual time evolution of the liquid with an adiabatic evolution for the electron. Within this approximation, the electron wave function is found by solving, at each time step, the static Schrödinger Eq. (4) to obtain the instantaneous 1P electron state Φ_{1P}, and the structure of the liquid is obtained by determining the complex, time-dependent effective wave function $\Psi(\mathbf{r},t)$ from the time-dependent DF equation

$$\imath\hbar\frac{\partial\Psi(\mathbf{r},t)}{\partial t} = -\frac{\hbar^2}{2m_{\mathrm{He}}}\Delta\Psi(\mathbf{r},t) + \left\{\mathcal{U}[\rho,\mathbf{v}] + |\Phi_{1P}|^2\frac{\partial V_{\text{e-He}}(\rho)}{\partial\rho}\right\}\Psi(\mathbf{r},t), \quad (5)$$

where the effective potential $\mathcal{U}[\rho,\mathbf{v}]$ is given, e.g., in Refs. 30 and 31 and has an explicit dependence on the local current field $\mathbf{j}(\mathbf{r})=\rho(\mathbf{r})\mathbf{v}(\mathbf{r})$ arising from the backflow term the static potential energy in Eq. (1) lacks of. These coupled equations are solved imposing as initial conditions the stationary solution of the superfluid for the spherical 1S ebubble, employing the electron wave function Φ_{1P} for building the e-He interaction, as indicated in Eq. (5). The time step has been set to 0.01 ps, and we have used a fourth-order Runge-Kutta method to obtain the first time steps of the evolution. To determine the solution for subsequent times, we have used Hamming's (predictor-modifier-corrector) method.[39] This procedure is very robust and accurate, even for large amplitude motions.[40]

B. Results

We have solved the adiabatic-dynamic coupled equations for $P=0$, 0.5, 1, 2, 3, and 5 bars. We will mostly show results for the two extreme pressure values, namely, 0 and 5 bars. The evolution starts by stretching the bubble along the symmetry z axis and shrinking its waist. This produces density waves in the liquid that take away a sizeable part of the energy injected into the system during the absorption process, 105 meV at $P=0$ bar and 148 meV at 5 bars.[9]

The evolution can be safely followed for about 25–30 ps. For larger times, the density waves reflected on the box boundaries get back to the region where the bubble sits, spoiling the calculation. This time interval is large enough to see bubble splitting at the higher pressures. Otherwise, one needs to introduce a source of damping in the equation governing the liquid evolution [Eq. (5)], to prevent sound waves from bouncing back. Usually, introducing damping requires to enlarge the calculation box to accommodate a buffer region where waves are washed out, see, e.g., Refs. 8, 21, 22, and 41. This increases the number of grid points and slows the calculation.

Below 1 bar, we have found that the ebubble configuration is simply connected and radiates a sizeable part of the excitation energy as sound waves. For instance, at $P=0$ bar, the energy difference between the spherical 1P configuration and the relaxed 1P quasiequilibrium configuration is ~40 meV (see Fig. 1). The ebubble undergoes damped oscillations that will likely lead it to the corresponding quasistatic 1P configuration described in Sec. II. As a consequence, it would eventually decay radiatively to the deformed 1S state that will radiationless evolve toward the spherical 1S state.

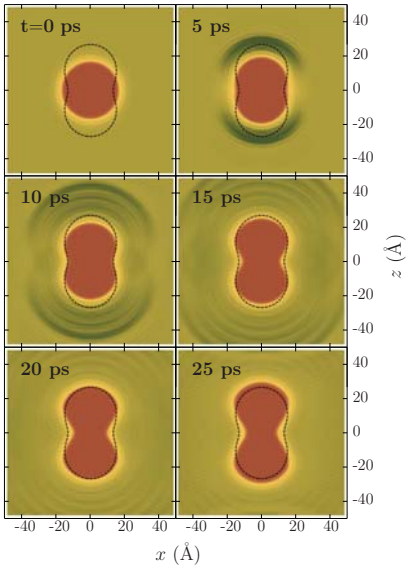

FIG. 3. (Color online) Adiabatic evolution of the 1P ebubble at $P=0$ bar. The panels display the helium configurations corresponding to 0, 5, 10, 15, 20, and 25 ps. The dashed line represents the dividing surface of the quasiequilibrium configuration at $P=0$ bar shown in Fig. 2.

An example of this sort of evolution is shown in Fig. 3 for $P=0$ bar. We have found that after 15 ps, the shape of the 1P bubble is similar to the quasistatic configuration referred to in Sec. II. Using a simpler model, Maris has found a smaller value, 11 ps.[2] The difference is a natural consequence of the two basic approximations he has made, namely, treating the liquid as incompressible and neglecting sound-wave radiation. Due to the inertia of the bubble in the expansion process, it continues to stretch in the direction of the symmetry axis. This dilatation in the z direction goes on for the largest times we have followed the evolution (30 ps), accompanied by the appearance of a more marked neck.

At 1 bar, the neck collapses due to the large kinetic energy of the liquid filling in the region between the two 1P lobes, and the ebubble configuration becomes nonsimply connected. This causes the deformed 1P and 1S levels to become nearly degenerate, and their probability densities are almost identical. The appearance of any asymmetric fluctuation, which is beyond the scope and capabilities of our framework, will cause the electron to eventually localize in either of the baby bubbles. The subsequent evolution of the system is the collapse of the empty baby bubble and the evolution of the other one toward the spherical 1S ground state. In this case, the excited 1P bubble decays to the 1S spherical configuration without passing through the 1P quasistatic configuration described in the previous section, and the deexcitation is nonradiative. An example of this sort of evolution is shown in Fig. 4 for $P=5$ bars. For this pressure, we have found that a configuration similar to the simply

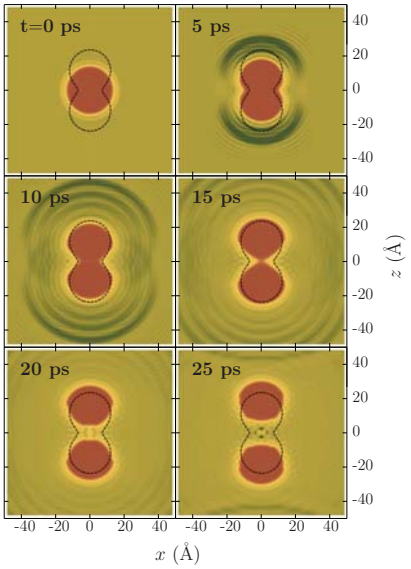

FIG. 4. (Color online) Adiabatic evolution of the 1P ebubble at $P=5$ bars. The panels display the helium configurations corresponding to 0, 5, 10, 15, 20, and 25 ps. The dashed line represents the dividing surface of the quasiequilibrium configuration at $P=5$ bars shown in Fig. 2.

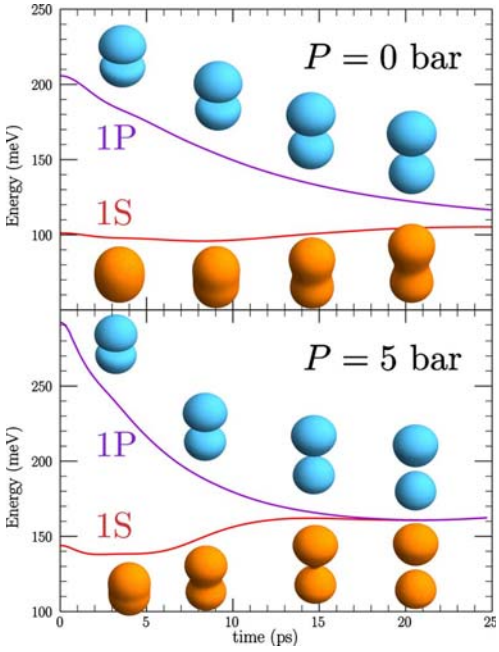

FIG. 5. (Color online) Adiabatic evolution of the energies of the 1S (empty) and 1P (occupied) states, together with a representation of the electron-probability densities for $P=0$ bar (top panel) and $P=5$ bar (bottom panel). The electron-probability densities are also displayed at four selected time values.

connected quasistatic one is attained after 10 ps, although the inertia of the bubble expansion breaks the quasistatic neck at about 18 ps. The density pileup in the neck region continues and at about 22 ps the helium density in this region has a peak of $\sim 2\rho_0$, whose relaxation pushes the two baby bubbles in opposite directions helping the fission process.

Our calculations are in agreement with cavitation experiments[42] indicating that relaxed 1P bubbles are only produced for pressures smaller than about 1 bar, and that above this value the decay of the excited bubble has to proceed differently, likely radiationless. Indeed, we have found that the 1P bubble fissions at $P=1$ bar, but it does not at $P=0.5$ bar. Our results are also in agreement with the interpretation[27] of the vanishing of the photoconductivity signal below 1 atm experimentally observed by Grimes and Adams.[6] According to this interpretation, an ebubble in the 1P state is unstable against a radiationless de-excitation back to the ground state, the electron ultimately settling into one of the baby bubbles while the other collapses with phonon (heat) emission. It is this released heat that drives the photocurrent. Below that pressure, the ebubble decays radiatively, it does not release enough heat and is not detected in the photocurrent experiment.

The evolution of the electron energies for the 1S (empty) and 1P (occupied) states, together with a representation of the electron-probability densities, is presented in Fig. 5 for two pressure values. The fission of the bubble at $P=1$ bar happens after 60 ps. To obtain this result, we have proceeded as in Refs. 21 and 22, introducing a damping term in Eq. (5). To make sure that the bubble does not fission at $P=0.5$ bar, we have also introduced a damping term for this pressure.

We have studied the excitations produced in the liquid by the expansion of the ebubble. From the evolution of the first wave front, we have estimated that it moves in the z direction at ~ 330 m/s at $P=0$ bar and at ~ 410 m/s at $P=5$ bars. These values are well above the speed of sound in helium at these pressures, meaning that the dynamics is highly nonlinear. Besides, we have determined the nature of these excitations by Fourier analyzing the density waves along the z axis, leaving aside the region near the bubble surface. The density profile is shown in the top panel of Fig. 6, corresponding to $P=0$ bar at 13 ps, and the Fourier transform of the density fluctuation (related to the static structure function of the liquid) is presented in the bottom panel. Apart from the low-q component, arising from the mean-density profile, one can identify two distinct peaks, the more marked one at $q \sim 0.8$ Å^{-1} in the phonon branch near to the maxon region, and another at $q \sim 2.3$ Å^{-1} slightly to the right of the roton minimum. A similar "roton" peak was found in Ref. 8. A less marked peak appears at $q \sim 1.7$ Å^{-1}, slightly to the left of the roton minimum. Similar peaks have been found for shorter and larger times. From the relative intensity of these peaks, we are prone to identify most of the emitted waves as high-energy "phonons."

We have also analyzed the effect of the backflow term on the appearance of the density waves. One can see from the bottom panel of Fig. 6 that neglecting this term changes a little the relative intensity of the phonon and roton peaks, increasing the former and decreasing the later as expected from the effect of the backflow term on the excitation modes of the superfluid, see Fig. 12 of Ref. 17. We want to stress that rotons are not excited if one uses a less accurate, local

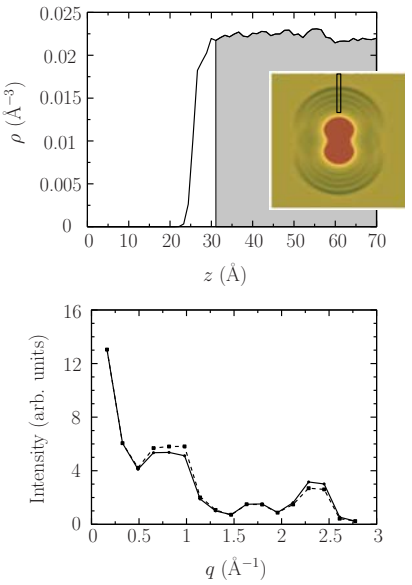

FIG. 6. (Color online) Top panel: density profile of the superfluid corresponding to $P=0$ bar at 13 ps (only the $z \geq 0$ part is shown). The inset shows the ebubble configuration in a 140 $\times 140$ Å^2 frame, and the region displayed in the rectangle is the Fourier transformed one. Bottom panel: solid line, Fourier transform of the superfluid density profile shown in gray in the top panel. The dashed line is the Fourier transform of the density obtained at the same evolution time without including backflow effects. In both cases the peak at $q=0$ Å^{-1} arises from the mean-density profile, not subtracted from the local density before transforming. The lines have been drawn as a guide to the eyes.

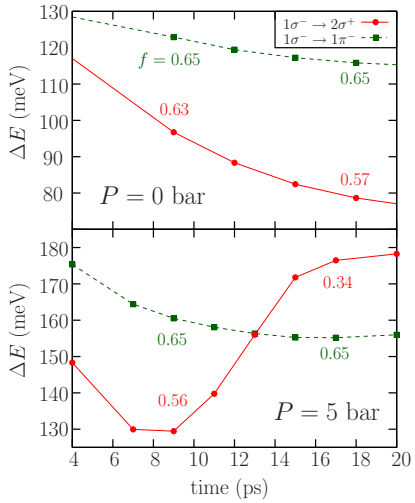

FIG. 7. (Color online) Time-resolved excitation energies at $P=0$ and 5 bars for electron transitions from the $1\sigma^-$ state arising from the spherical 1P, $m=0$ one, to either the $1\pi^-$ state (circles), or to the $2\sigma^+$ one (squares), both initially belonging to the spherical 1D manifold. In each panel, the oscillator strength for two selected time values is also displayed. Lines have been drawn as a guide to the eyes.

functional such as that of Refs. 18–22. In this case, only the low-q phonon spectrum of the superfluid is quantitatively reproduced. Whether this has a sizeable influence on the ebubble dynamics or not, can only be ascertained by a detailed comparison between the results obtained using both kind of functionals.

1P ebubbles may be excited by photoabsorption to the 1D state, either to its $m=0$ component ($2\sigma^+$) or to its $m=\pm 1$ components ($1\pi^-$). The absorption spectrum at different stages of the time evolution can be measured in a pump-probe experiment by which the ebubble is excited by two consecutive laser pulses. The delay set between these pulses should correspond to the time elapsed between the excitation of the spherical bubble and the time at which the absorption spectrum of the 1P ebubble is recorded. Time-resolved electronic spectroscopy has been proposed by Rosenblit and Jortner[38] as a tool for the exploration of the localization dynamics of the excess electron.

Time-resolved excitation energies are shown in Fig. 7 at $P=0$ and 5 bars. While the evolution of the $1\sigma^- \rightarrow 1\pi^-$ excitation is qualitatively similar at both pressures, the $1\sigma^- \rightarrow 2\sigma^+$ excitation evolves differently in the high-pressure regime when the bubble splits. Indeed, at 0 bar the excitation energy smoothly decreases with time, whereas at 5 bars it starts decreasing, increasing next, and eventually becoming larger than the excitation energy to the $1\pi^-$ state. Note that both the change in behavior and the crossing take place some picosecond before bubble splitting.

The $1\sigma^- \rightarrow 1\pi^-$ transition is little affected by bubble splitting because it involves two states with negative specular symmetry, which means that the probability density of both states is zero in the neck region. On the contrary, the $1\sigma^- \rightarrow 2\sigma^+$ transition involves two states with different specular symmetry and thus it is more affected by bubble splitting.

Along with the excitation energies, some values of the associated oscillator strengths are displayed in Fig. 7. The oscillator strengths have been calculated in the dipole approximation as[43]

$$f_{ab} = \frac{2m_e}{3\hbar^2}(E_a - E_b)|\langle a|\mathbf{r}|b\rangle|^2.$$

As known, the oscillator strengths fulfill a sum rule that in the one-electron case is $\Sigma_a f_{ab}=1$.[44] At both pressures, we have found that these transitions have comparable oscillator strengths. The largest difference appears for $P=5$ bars in the split-bubble regime. In it, the strength of the $1\sigma^- \rightarrow 2\sigma^+$ transition is roughly half that of the $1\sigma^- \rightarrow 1\pi^-$ transition. We thus conclude that the analysis of the peak energy and oscillator strength of the $1\sigma^- \rightarrow 2\sigma^+$ transition might disclose the fission-like behavior of the excited 1P bubble, complementing the experimental information gathered from cavitation and photoconductivity experiments.

The current field $[\mathbf{j}(\mathbf{r})=\rho(\mathbf{r})\mathbf{v}(\mathbf{r})]$ is shown in Fig. 8 for $P=0$ and 5 bars at 12 and 22 ps. At 12 ps the current fields are qualitatively similar for both pressures: the bubble expands along the symmetry axis and shrinks in a plane perpendicular to it. At 22 ps, when $P=5$ bars, large currents keep bringing liquid into the neck region, splitting the bubble

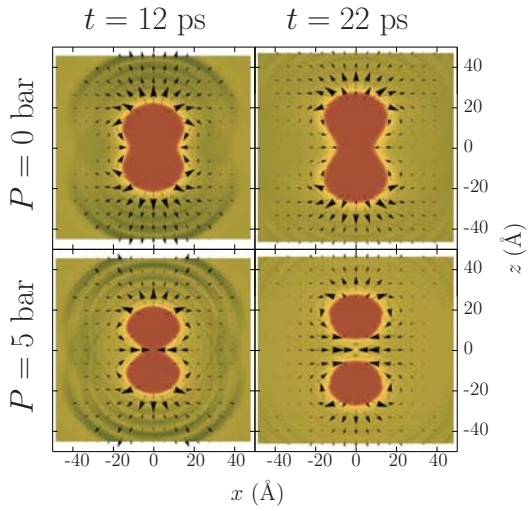

FIG. 8. (Color online) Current field at $P=0$ bar (top panels) and 5 bars (bottom panels) at time $t=12$ ps (left) and $t=22$ ps (right). In each panel, the larger the arrow, the larger the current.

and producing important density oscillations in the central region.

We have also followed the collapse of the 2P bubble at $P=0$ bar. About 2 ps after the collapse has started, a sizeable part of the excitation energy has been released into the liquid and two waves are distinguishable around the bubble, as shown in Fig. 9. These waves travel through the liquid at the same speed as in the 1P bubble case, ~330 m/s. Shortly after 7 ps, the $m=0$ levels of the 2P and 1F states become very close and, as discussed in the next section, see Eq. (7), the adiabatic approximation fails. At this point, the 2P bubble displays an incipient four-lobe shape arising from a similar structure in the 2P electron probability density. It is worth mentioning that a likely related effect, namely, the near degeneracy of the 2P and 1F states, was found in the quasistatic calculations of Ref. 26 as P increased.

In view of the mentioned failure and the lacking of experimental information on the collapse of the 2P bubble, we have closed its study at this point, leaving it for future work.

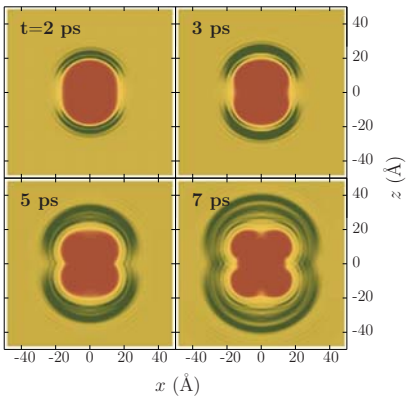

FIG. 9. (Color online) Adiabatic evolution of the 2P ebubble at $P=0$ bar. The panels display the helium configurations corresponding to 2, 3, 5, and 7 ps.

IV. VALIDITY OF THE ADIABATIC APPROXIMATION

The validity of the adiabatic approximation in the first stages of the bubble collapse, when the topology of the bubble is simply connected, stems from the very different time scale of the electron motion as compared to that of the bubble,[45] represented by the period of its shape oscillations. If the fluid is incompressible and the bubble spherical, the surface λ modes of the cavity are at energies

$$\hbar\omega_\lambda = \sqrt{\frac{\gamma}{m_{\mathrm{He}}\rho_0 R^3}(\lambda-1)(\lambda+1)(\lambda+2)}, \qquad (6)$$

where γ and ρ_0 are the surface tension and atom density of the liquid, respectively. For $\lambda=2$ this energy is about 1 K, and the period of the oscillation is ~50 ps.

The situation may change in the course of the collapse because the energy difference $\Delta=E_{1\mathrm{P}}-E_{1\mathrm{S}}$ between the deformed states decreases and the time scale $\tau=h/\Delta$ may become similar to the period of the shape oscillations of the deformed bubble. Since Δ is small in the two bubble regime, the approximation likely fails there.[27,46] It is worthwhile mentioning that neck fluctuations, not included in our approach nor in previous works, would pinch off the bubble at earlier stages of the collapse, in a similar way as they may cause the prompt scission of the fissioning atomic nucleus after the saddle configuration has been overcome.[47]

On the light of our model, in which no assumptions are made on the shape of the bubble nor the impenetrability of the bubble surface by the localized electron, it is instructive to analyze the validity of the adiabatic approximation assuming that, during the evolution, the bubble keeps its original axial symmetry and specular symmetry about the plane perpendicular to the symmetry axis that contains the node of the 1P state. This excludes any possible fluctuation and the appearance of asymmetric modes, like the breathing mode discussed in Ref. 27. Our discussion relies on the detailed presentation by Messiah,[48] that we summarize in the following.

The subsystem to which the adiabatic approximation is applied is the electron, whose wave function is decoupled from that of the liquid. This wave function evolves in the potential field generated by the liquid distribution, and its Hamiltonian is time dependent, $\mathcal{H}_{\mathrm{e}}(t)=\mathcal{H}_{\mathrm{e}}[\rho_{\mathrm{He}}(t)]$. Let ϕ_n^t be an eigenfunction of the Hamiltonian at time t, so that $\mathcal{H}_{\mathrm{e}}(t)\phi_n^t=\varepsilon_n(t)\phi_n^t$. If $\phi_n(t)$ is the actual wave function ϕ_n^0 evolved up to time t, one has $\phi_n(t)=\mathcal{U}(t)\phi_n^0$, where $\mathcal{U}$ is the evolution operator. In the adiabatic approximation, one identifies $\phi_n(t)$ with ϕ_n^t, the intuitive justification being that if one perturbes the subsystem slowly and gently enough, it has enough time to adapt itself to the new environment "with no inertia" from the past configuration.

The error made in this approximation for a given state $|i\rangle$—the validity of the adiabatic approximation is assessed for a given state of the subsystem, not necessarily for them all—is defined as the probability of finding the subsystem in a state different from the initial one evolved in time within the "true" dynamics, $\eta_{ij}=|\langle\phi_j^t|\mathcal{U}(t)|\phi_i^0\rangle|^2$. This error can be written in a workable way as[48]

$$\eta_{ij}(t) = \left| \frac{\hbar}{[\varepsilon_j(t) - \varepsilon_i(t)]^2} \langle \phi_j^t | \frac{d\mathcal{H}_e}{dt} | \phi_i^t \rangle \right|^2. \quad (7)$$

If $\eta_{ij} \ll 1 \, \forall \, i \neq j$, the adiabatic approximation is justified. It is usually understood that it breaks down when the levels get very close or when they cross each other. Notice, however, that this assumes that these states can be connected by the evolved Hamiltonian. If a symmetry is dynamically conserved (in our case, angular momentum and specular symmetry are), then the adiabatic evolution of states with a given quantum number associated to this symmetry is not perturbed by states with different values of this quantum number. Although sometimes ignored, this is a very reasonable statement.

In the case of the $1\sigma^-$ state arising from the spherical 1P manifold, the adiabatic approximation holds even when its energy becomes almost identical to the energy of the $1\sigma^+$ state arising from the spherical 1S one, i.e., a small Δ does not invalidate the adiabatic approximation. The closest state having the same angular momentum and specular symmetry is the $2\sigma^-$ one arising from the spherical 1F manifold. At $P=5$ bars, we have found that these two states are 2000 K apart in the 10–20 ps range. Since $\hbar \sim 7.6$ K ps, one has $\hbar/(E_{2\sigma^-} - E_{1\sigma^-})^2 \sim 2 \times 10^{-6}$ ps K^{-1}. The value of the matrix element in Eq. (7) is some tens of kelvin per picosecond, so that the adiabatic approximation would be fulfilled even for the configuration displayed in Fig. 4 at 25 ps. Indeed, we have calculated η in the above time range and have found that it is on the order of 10^{-8}.

It is also worth analyzing the stability of the quasiequilibrium configurations when the symmetries are not exactly conserved because of perturbations from the environment. In this situation, let us assume that when the bubble splits the electron localizes in one of the lobes. Leaving out the discussion on the actual localization process, we have tried to infer the likely evolution of an ebubble with a localized electron. The localized electron state in either baby bubble is approximated by

$$\Phi_\pm = \frac{1}{\sqrt{2}} \phi_{1S} \pm \frac{1}{\sqrt{2}} \phi_{1P}. \quad (8)$$

Consider now a short-time dynamics in which the liquid is kept frozen. The evolution of, e.g., the Φ_+ localized state is an oscillation between the two lobes

$$\Phi(t) = e^{-iE_{1S}t/\hbar} [\cos(\omega t)\Phi_+ - i \sin(\omega t)\Phi_-], \quad (9)$$

where $\omega = (E_{1P} - E_{1S})/\hbar$. If this frequency is large enough, the liquid cannot react to the localization of the electron in either lobe and will essentially behave as if the electron were delocalized.

The time elapsed between two consecutive localizations of the electron in a given baby bubble is $\tau = \pi/\omega$. The value of this period as a function of pressure for the quasiequilibrium configurations is displayed in Fig. 10. In the split-bubble regime ($P \gtrsim 9$ bars), this period is of several picosecond, indicating that the electron-localization dynamics into one of the baby bubbles is not a trivial process to address.

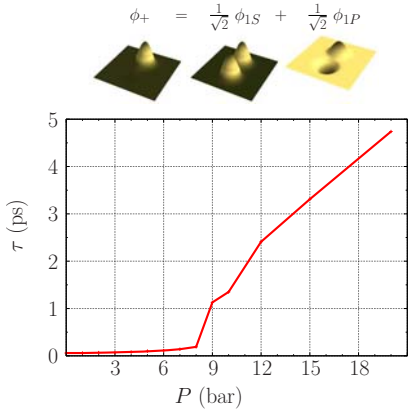

FIG. 10. (Color online) Top: superposition of the 1S and 1P states corresponding to the quasiequilibrium configuration at $P = 9$ bars to approximately localize the electron in one of the baby bubbles. Bottom: tunneling period of a localized electron in one of the lobes of the quasiequilibrium ebubble as a function of pressure.

The electron will bounce back and forth as the liquid tries to adapt to it. Real-time calculations are thus needed to describe electron localization.

It is clear that the previous discussion on the validity of the adiabatic evolution lacks for incorporating fluctuations or excitations of low-energy modes that may appear in the course of the bubble evolution and couple the 1P and 1S states that otherwise are not, as previously discussed. One such mode has been thoroughly addressed by Elser:[27] a peanut configuration, whose walls are impenetrable by the electron, is represented by two intersecting sharp spheres of radius R_2 (instead of the deformed baby bubbles displayed in Fig. 4) joined along a circular orifice of radius a. These spheres are breathing in counterphase, producing an antisymmetric mode whose stiffness $\mathcal{K}$ and inertia $\mathcal{M}$ can be obtained analytically. This mode is very appealing, as it represents a small, swifting imbalance of the symmetric electron-probability density.

In the harmonic limit, if $a \ll R_2$, the stiffness and inertia of the asymmetric mode are[49]

$$\mathcal{K} = 16 \left[\frac{E_0^2}{R_2^2 \Delta} + \pi(\gamma + R_2 P) \right],$$

$$\mathcal{M} = 4\pi\xi m_{^4\mathrm{He}} \rho_0 R_2^3. \quad (10)$$

In these equations, $E_0 = \gamma R_0^2 \sim 9$ meV represents the energy unit with $\gamma = 2.36 \times 10^{-2}$ meV Å^{-2} being the surface tension of the liquid, $R_0 \sim 20$ Å is the radius of the spherical bubble, $R_2 \sim 16$ Å is the radius of the baby bubbles, $\xi \sim 1.70$ is a dimensionless constant, and $\Delta = E_{1P} - E_{1S}$. The frequency of the antisymmetric breathing mode is given by $\omega_{AB} = \sqrt{\mathcal{K}/\mathcal{M}}$, and the radius of the orifice is[27]

$$\Delta = \frac{4\pi}{3} E_0 \left(\frac{R_0}{R_2}\right)^2 \left(\frac{a}{R_2}\right)^3. \quad (11)$$

The adiabatic approximation fails when $\omega_{AB} \simeq \Delta/\hbar$. This yields $\Delta \sim 0.14$ meV in the $P=0-5$ bars range, as only the first term in the stiffness turns out to be relevant in this regime. Thus, keeping only the first term in $\mathcal{K}$, one gets[50]

$$\frac{a}{R_2} = \left[\left(\frac{27}{8\pi^4 \xi}\right)\left(\frac{m_e}{m_{He}\rho_0 R_0^3}\right)\left(\frac{R_2}{R_0}\right)\right]^{1/9} \sim 0.13. \quad (12)$$

Hence, $a \sim 2.1$ Å. Clearly, such analytical results cannot be obtained within the DF approach, but we can use them to determine whether the dynamic and static configurations shown in Secs. II and III are reliable.

The adiabatic approximation thus holds at $P=0$ bar, as the neck radius is fairly large, see Fig. 3, and Δ is always much larger than 0.14 meV, see Fig. 5. From Fig. 4 we also conclude that, at $P=5$ bars, the adiabatic approximation is valid up to nearly the collapse of the waist. Indeed, the neck radius of the helium configuration at about 17–18 ps is ~ 2 Å, see Fig. 4. It is worth noting the difficulty in defining an effective radius for the orifice when the surface of the bubble is diffuse; we recall that the surface thickness of a ^{4}He drop of 10^3-10^4 atoms is some 6–8 Å.[51] Note also that the surface thickness of the helium bubble is rather independent of the curvature of the surface, as can be inferred from the fairly constant bright region around the bubbles displayed in Figs. 3 and 4.

Since we do not treat the bubble as impenetrable to the excess electron, the relation between the actual Δ and a values should not exactly be as given by Eq. (11). Using the result $\hbar\omega_{AB} \leq \Delta = 0.14$ meV as a criterion for the applicability of the adiabatic approximation instead of reaching the limiting value $a \sim 2$ Å, we find that the approximation holds up to 21 ps, when the bubble has already split into two baby bubbles. Both procedures indicate that when the adiabatic approximation likely fails, the baby bubbles have already developed.

The previous analysis leads us to conclude that, at high pressures, baby bubbles are formed some tens of picosecond after the starting of the collapse of the 1P bubble. From this point on, the likely fate of the system is the localization of the electron in one of the baby bubbles and the collapse of the other. This process is helped/triggered by fluctuations that break the specular symmetry of the ebubble configuration. As mentioned, determining the time scale of electron localization is beyond the capabilities of the adiabatic approximation. It has been calculated[21] that once the electron is localized, it takes to the superfluid some 20 ps to adapt to it while the other baby bubble is absorbed.

V. SUMMARY

Within density-functional theory, we have carried out an analysis of the adiabatic evolution of the excited electron bubble in superfluid liquid ^{4}He. We have found that for pressures below 1 bar, the 1P ebubble may relax to its quasistatic equilibrium configuration and decay radiatively to the deformed 1S state. This state evolves nonradiatively to the spherical 1S bubble, completing the absorption/emission cycle. This conclusion arises, in part, from studies carried out for 100 ps using a less accurate functional,[52] whose results qualitatively agree with ours for the first tens of picosecond.

At higher pressures, the situation drastically changes and the excited 1P bubble no longer decays to the quasistatic equilibrium configuration, whose physical realization is unlikely. Indeed, our analysis of the adiabatic approximation indicates that it is valid up to a point where two deformed, nearly disconnected baby bubbles appear in the dynamical evolution, pointing toward a fission-like de-excitation process, the likely subsequent evolution of the system being the localization of the electron in one of the baby bubbles and the collapse of the other. This collapse takes some 20 ps,[21] and the whole de-excitation process is radiationless.

We have also found a marked change in the behavior of the time-resolved absorption spectrum of the 1P bubble depending on whether the bubble fissions or not, i.e., on the liquid pressure. This change is, in principle, an experimentally accessible observable whose determination may complement the information obtained from cavitation and photoconductivity experiments.

Our analysis of the collapse of the 2P bubble has shown that the adiabatic approximation breaks down at an early stage of the dynamical process due to the crossing of 2P and 1F states. Although disclosed by the adiabatic approximation, this crossing has nothing to do with the approximation itself, but is inherent to the dynamics of the electron bubble. From the crossing point on, the bubble will relax around a mixed state with 2P and 1F components, and hence the physical realization of a pure quasiequilibrium 2P configuration is unlikely. It is very plausible that the same applies to other high-energy nL ebubbles generated in the absorption process. The possibility that some of them undergo a spontaneous symmetry breaking, as suggested by Grinfeld and Kojima[53] for the 2S state, can only reinforce our conclusion. Obviously, this does not question the existence of either relaxed quasiequilibrium configurations at low pressures or of baby bubbles at high pressures, arising from the evolution of the spherical 2P bubble. It just means that, on the one hand, the relaxed bubble will not be a pure 2P configuration and, on the other hand, to study the de-excitation of these bubbles one has to go beyond the adiabatic approximation and carry out a more demanding real-time dynamics calculation for the electron.

ACKNOWLEDGMENTS

We thank Humphrey Maris, Francesco Ancilotto, Dafei Jin, and Alberto Hernando for useful discussions. This work has been performed under Grant No. FIS2008-00421/FIS from DGI, Spain (FEDER), and Grant No. 2009SGR1289 from Generalitat de Catalunya.

[1] M. Rosenblit and J. Jortner, J. Chem. Phys. **124**, 194505 (2006); **124**, 194506 (2006).
[2] H. J. Maris, J. Phys. Soc. Jpn. **77**, 111008 (2008).
[3] J. A. Northby and T. M. Sanders, Phys. Rev. Lett. **18**, 1184 (1967).
[4] W. B. Fowler and D. L. Dexter, Phys. Rev. **176**, 337 (1968).
[5] T. Miyakawa and D. L. Dexter, Phys. Rev. A **1**, 513 (1970).
[6] C. C. Grimes and G. Adams, Phys. Rev. B **41**, 6366 (1990).
[7] C. C. Grimes and G. Adams, Phys. Rev. B **45**, 2305 (1992).
[8] J. Eloranta and V. A. Apkarian, J. Chem. Phys. **117**, 10139 (2002).
[9] V. Grau, M. Barranco, R. Mayol, and M. Pi, Phys. Rev. B **73**, 064502 (2006).
[10] L. Lehtovaara and J. Eloranta, J. Low Temp. Phys. **148**, 43 (2007).
[11] B. DuVall and V. Celli, Phys. Rev. **180**, 276 (1969).
[12] M. Pi, R. Mayol, A. Hernando, M. Barranco, and F. Ancilotto, J. Chem. Phys. **126**, 244502 (2007).
[13] W. Guo, D. Jin, G. M. Seidel, and H. J. Maris, Phys. Rev. B **79**, 054515 (2009).
[14] A. Ghosh and H. J. Maris, Phys. Rev. Lett. **95**, 265301 (2005).
[15] J. Tempere, I. F. Silvera, and J. T. Devreese, Surf. Sci. Rep. **62**, 159 (2007).
[16] J. Fang, A. E. Dementyev, J. Tempere, and I. F. Silvera, Rev. Sci. Instrum. **80**, 043901 (2009).
[17] F. Dalfovo, A. Lastri, L. Pricaupenko, S. Stringari, and J. Treiner, Phys. Rev. B **52**, 1193 (1995).
[18] S. Stringari and J. Treiner, Phys. Rev. B **36**, 8369 (1987); J. Chem. Phys. **87**, 5021 (1987).
[19] N. G. Berloff and P. H. Roberts, Phys. Rev. B **63**, 024510 (2000); J. Phys. A **34**, 81 (2001).
[20] E. J. M. Madarassy and C. F. Barenghi, J. Low Temp. Phys. **152**, 122 (2008).
[21] D. Jin, W. Guo, W. Wei, and H. J. Maris, J. Low Temp. Phys. **158**, 307 (2010).
[22] D. Jin and H. J. Maris, J. Low Temp. Phys. **158**, 317 (2010).
[23] N. G. Berloff and P. H. Roberts, J. Phys. A **32**, 5611 (1999).
[24] N. G. Berloff and P. H. Roberts, Phys. Lett. A **274**, 69 (2000).
[25] D. Mateo, A. Hernando, M. Barranco, and M. Pi, J. Low Temp. Phys. **158**, 397 (2010).
[26] H. J. Maris, J. Low Temp. Phys. **132**, 77 (2003).
[27] V. Elser, J. Low Temp. Phys. **123**, 7 (2001).
[28] R. Jackiw, C. Rebbi, and J. R. Schrieffer, J. Low Temp. Phys. **122**, 587 (2001).
[29] F. Ancilotto, M. Barranco, and M. Pi, Phys. Rev. Lett. **91**, 105302 (2003).
[30] L. Lehtovaara, T. Kiljunen, and J. Eloranta, J. Comput. Phys. **194**, 78 (2004).
[31] L. Giacomazzi, F. Toigo, and F. Ancilotto, Phys. Rev. B **67**, 104501 (2003).
[32] F. Ancilotto, F. Dalfovo, L. P. Pitaevskii, and F. Toigo, Phys. Rev. B **71**, 104530 (2005).
[33] E. Cheng, M. W. Cole, and M. H. Cohen, Phys. Rev. B **50**, 1136 (1994); **50**, 16134 (1994) (erratum).
[34] M. Pi, M. Barranco, R. Mayol, and V. Grau, J. Low Temp. Phys. **139**, 397 (2005).
[35] M. Frigo and S. G. Johnson, Proc. IEEE **93**, 216 (2005).
[36] M. Barranco, M. Guilleumas, E. S. Hernández, R. Mayol, M. Pi, and L. Szybisz, Phys. Rev. B **68**, 024515 (2003).
[37] M. Rosenblit and J. Jortner, Phys. Rev. Lett. **75**, 4079 (1995).
[38] M. Rosenblit and J. Jortner, J. Phys. Chem. A **101**, 751 (1997).
[39] A. Ralston and H. S. Wilf, *Mathematical Methods for Digital Computers* (Wiley, New York, 1960).
[40] M. Barranco, R. Guardiola, S. Hernández, R. Mayol, J. Navarro, and M. Pi, J. Low Temp. Phys. **142**, 1 (2006).
[41] Ch. Cerjan, D. Kosloff, R. Kosloff, and M. Reshef, Geophysics **50**, 705 (1985).
[42] H. J. Maris, A. Ghosh, D. Konstantinov, and M. Hirsch, J. Low Temp. Phys. **134**, 227 (2004).
[43] M. Weissbluth, *Atoms and Molecules* (Academic Press, New York, 1978).
[44] Recall that if the initial state $|b\rangle$ is not the ground state, the sum includes negative terms arising from de-excitation transitions, hence a partial sum can be greater than unity.
[45] H. J. Maris, J. Low Temp. Phys. **120**, 173 (2000).
[46] A. I. M. Rae and W. F. Vinen, J. Low Temp. Phys. **123**, 1 (2001).
[47] U. Brosa, S. Grossmann, A. Müller, and E. Becker, Nucl. Phys. A **502**, 423 (1989).
[48] A. Messiah, *Quantum Mechanics* (North-Holland, Amsterdam, 1962).
[49] Since the asymmetric mode of Ref. 27 does not conserve the volume of the bubble, the stiffness slightly changes from the expression given in Ref. 27 if $P \neq 0$. In the numerical application we have used the $\gamma(P)$ law deduced in Ref. 9.
[50] This equation differs from Eq. (9) of Ref. 27 because of an error made there to obtain it from a straightforward combination of its Eqs. (3) and (8), as can be easily checked.
[51] J. Harms, J. P. Toennies, and F. Dalfovo, Phys. Rev. B **58**, 3341 (1998).
[52] D. Jin, W. Guo, W. Wei, and H. J. Maris (unpublished), and Ref. 21.
[53] P. Grinfeld and H. Kojima, Phys. Rev. Lett. **91**, 105301 (2003).

3.2 Excited electron-bubble states in superfluid ^{4}He: A time-dependent density functional approach

Resumen (Spanish)

Presentamos un estudio sistemático de los diferentes estados excitados de las burbujas electrónicas en ^{4}He superfluido usando el método del funcional de la densidad dependiente del tiempo. Para describir la evolución de las burbujas 1P hemos usado dos funcionales distintos junto con dos esquemas diferentes de evolución temporal: un funcional preciso de rango finito para el helio con una aproximación adiabática para el electrón, y un funcional eficiente de rango cero para el helio con una evolución en tiempo real para el electrón. Una comparación detallada entre los resultados obtenidos con cada método nos permite seleccionar el más idóneo para cada problema.

Con este conocimiento previo, hemos aplicado el funcional de rango finito al cálculo del espectro de absorción de las burbujas 1P resuelto temporalmente, en principio accesible experimentalmente con la tecnología actual. También hemos usado el funcional de rango cero para calcular la evolución en tiempo real de la burbuja 2P durante unos cientos de picosegundos, que presenta interés a nivel teórico debido a la pérdida de adiabaticidad de este estado. Nuestros resultados permiten descartar la existencia de burbujas metaestables relajadas entorno de estados excitados por encima del 1P, invalidando por no ser físicos estudios previos de estos estados llevados a cabo con métodos estáticos.

THE JOURNAL OF CHEMICAL PHYSICS **134**, 044507 (2011)

Excited electron-bubble states in superfluid ^{4}He: A time-dependent density functional approach

David Mateo,[1] Dafei Jin,[2] Manuel Barranco,[1] and Martí Pi[1]
[1]*Departament ECM, Facultat de Física, and IN^{2}UB, Universitat de Barcelona. Diagonal 647, 08028 Barcelona, Spain*
[2]*Department of Physics, Brown University, Providence, Rhode Island 02912, USA*

(Received 3 November 2010; accepted 30 December 2010; published online 24 January 2011)

We present a systematic study on the excited electron-bubble states in superfluid ^{4}He using a time-dependent density functional approach. For the evolution of the 1P bubble state, two different functionals accompanied with two different time-development schemes are used, namely an accurate finite-range functional for helium with an adiabatic approximation for electron versus an efficient zero-range functional for helium with a real-time evolution for electron. We make a detailed comparison between the quantitative results obtained from the two methods, which allow us to employ with confidence the optimal method for suitable problems. Based on this knowledge, we use the finite-range functional to calculate the time-resolved absorption spectrum of the 1P bubble, which in principle can be experimentally determined, and we use the zero-range functional to real-time evolve the 2P bubble for several hundreds of picoseconds, which is theoretically interesting due to the break down of adiabaticity for this state. Our results discard the physical realization of relaxed, metastable configurations above the 1P state. © *2011 American Institute of Physics*. [doi:10.1063/1.3544216]

I. INTRODUCTION

Electron bubble (e-bubble) in liquid helium has been an attractive topic for numerous experimental and theoretical studies in the past, and it has drawn again some interest in recent years.[1–11] Density functional (DF) theory has proved to be a powerful tool in dealing with many interesting physical situations involving electron bubbles. When it is applied to optically excited e-bubbles, not only can it achieve quantitative agreement with experiments on the absorption spectra,[1,3,12,13] but it can also nicely display the dynamical evolutions on the picosecond time scale, such as how the bubbles change shapes, release energy, or even break into smaller bubbles.[14,15] These latest works likely require using different density functionals (finite-range or zero-range for liquid helium) in different time-development schemes (adiabatic or real-time evolutions for electron). Regardless of the technical details, the time-dependent density functional approach is no doubt the only workable approach at present for studying the evolution of the excited e-bubble states in liquid helium. The quantitative results drawn from these simulations can be useful to interpret the experimental results and predict new ones.

Upon dipole excitation from the 1S ground state to the 1P or 2P excited state, an e-bubble evolves by relaxing its shape around the excited electron probability density. This relaxation eventually drives the e-bubble back to the spherical 1S ground state. It has been quantitatively shown[15] that depending on the pressure (P) applied to the liquid, this may happen in two different ways. At a pressure below about 1 bar, the e-bubble undergoes damped oscillations for a period of time long enough to allow the electron to radiatively decay to the deformed 1S state, which then evolves radiationlessly to the spherical 1S state. In contrast, at 1 bar or above, the excited e-bubble evolves toward a configuration made of two baby bubbles, so that the probability of finding the electron evenly distributes between them. This two-bubble configuration is unstable against asymmetric perturbations, and one expects this instability to cause the electron to localize in one of the baby bubbles while the other collapses.[12,15,16]

When doing this calculation, the authors of Ref. 15 naturally chose the so-called Orsay–Trento DF.[17] This functional is finite range and incorporates a term that mimics backflow effects in order to accurately reproduce the dispersion relation of the elementary excitations of superfluid ^{4}He. This is instrumental to properly describe the energy transfer from the bubble to the liquid that proceeds by causing all sorts of possible excitations in the superfluid. The token one has to pay for its use is the very high computational cost. Due to the large difference between the intrinsic time scales of electron and helium, this functional is not well adapted for fully real-time, three-dimensional evolutions. Considering this limitation, the adiabatic approximation was used to update the electron wavefunction at every instantaneous helium configuration.[15] One of the main concerns is then to establish how long the adiabatic approximation is valid for. A careful analysis led to the conclusion that it holds for the 1P e-bubble for at least several tens of picoseconds,[15] a period of time large enough to guarantee the reliability of the results obtained for this state. Contrarily, the adiabatic approximation breaks down very quickly for the 2P e-bubble, implying that the existence of relaxed quasiequilibrium 2P bubbles is questionable.

The authors of Ref. 14 followed a different path. Instead of using a finite-range DF, they employed a much simpler zero-range one. This allowed them to carry out fully real-time calculations for hundreds of picoseconds without imposing any adiabatic assumption, at the price of an inaccurate description of the elementary excitations of the liquid. Although this may not qualitatively affect the physical

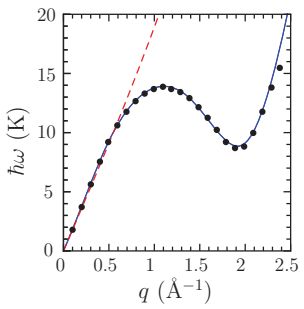

FIG. 1. Dispersion relation of the elementary excitation in bulk liquid ^{4}He at $T = 0$. Solid line: the OT finite-range functional results. Dashed line: the ST zero-range functional results. Dots: the experimental data from Ref. 22.

results, it is unclear how quantitatively reliable are the results so obtained.

In this work, we perform a more systematic study on the relaxation of the excited e-bubbles. We first carry out a detailed comparison between the finite-range and zero-range functionals applied to the 1P bubble problem, through which we gain some insight about their strong points and shortcomings. We then use the finite-range functional to calculate the time-resolved absorption spectrum of the 1P bubble, which can in principle be measured in the experiments. Next, we use the zero-range functional to real-time evolve the 2P bubble for several hundreds of picoseconds, which is of theoretical interest as one can clearly trace how the adiabatic approximation breaks down for this state. These investigations generalize and complement those presented in Ref. 15 within the adiabatic approximation.

Our paper is organized as follows. In Sec. II, we introduce the theoretical framework and numerical schemes. In Sec. III, we discuss the results so obtained. Finally, a summary is presented in Sec. IV. Several movies showing the dynamical evolution of electron bubbles can be found in the supplementary material.[18]

II. THEORETICAL FRAMEWORK

Within the DF approach, the energy of an electron–helium system at zero temperature can be written as a functional of the single-electron wavefunction Φ and the macroscopic helium wavefunction Ψ

$$E[\Phi,\Psi] = \frac{\hbar^2}{2m_e}\int d\boldsymbol{r}\,|\nabla\Phi|^2 + \frac{\hbar^2}{2m_{He}}\int d\boldsymbol{r}\,|\nabla\Psi|^2 + \int d\boldsymbol{r}\,|\Phi|^2\,V_{e-He}[\rho] + \int d\boldsymbol{r}\,\mathcal{E}_{He-He}[\rho]. \quad (1)$$

Specifically, $\Psi = \sqrt{\rho}\exp[\imath S]$ gives the helium particle density ρ and the superfluid velocity $\mathbf{v} = \hbar\nabla S/m_{He}$.[15] $V_{e-He}[\rho]$ is the electron–helium interaction potential,[19] and $\mathcal{E}_{He-He}[\rho]$ is the helium–helium potential energy density. For the sake of comparison, we choose for $\mathcal{E}_{He-He}[\rho]$ either the finite-range Orsay–Trento (OT) density functional,[17] or the zero-range Stringari–Treiner (ST) density functional.[20] It is known that the former one provides a very accurate description of superfluid ^{4}He, particularly of the dispersion relation that covers all the roton excitations up to the wave number $q = 2.3$ Å^{-1}. In contrast, the latter one only reproduces the long-wavelength phonon excitations and is not so accurate, but it has the advantage of high computational efficiency in dynamic evolutions. The dispersion relations obtained from both functionals using the method of Ref. 21 are plotted in Fig. 1 together with the experimental results.[22]

Functional variations of the associated grand potential with respect to Ψ and Φ yield the following Euler–Lagrange equation for the helium and Schrödinger equation for the electron:

$$-\frac{\hbar^2}{2m_{He}}\Delta\Psi + \left\{\frac{\delta\mathcal{E}_{He-He}[\rho]}{\delta\rho} + |\Phi|^2\,\frac{\delta V_{e-He}[\rho]}{\delta\rho}\right\}\Psi = \mu\Psi \quad (2)$$

$$-\frac{\hbar^2}{2m_e}\Delta\Phi + V_{e-He}[\rho]\Phi = \varepsilon\Phi\,, \quad (3)$$

where μ is the helium chemical potential and ε is the electron eigenenergy. Throughout this paper, we treat pressure as a given external condition. The associated chemical potential and particle density in bulk liquid are obtained from the equation of state derived from the DF being used.

The above equations are solved numerically with 13-point finite-difference formulae. In the finite-range DF case, we work in three-dimensional Cartesian coordinates that allow for an extensive use of fast Fourier transformation techniques[23] as explained in Ref. 5. Whenever necessary, we implement a Gram–Schmidt scheme to determine from Eq. (3) the electron spectrum in the helium cavity. In the zero-range DF case, we work in cylindrical coordinates assuming azimuthal symmetry around the z-axis ($r = 0$) and specular symmetry about the $z = 0$ plane. Hence, we only need to solve the equations in the $r \geq 0$ and $z \geq 0$ "quadrant," which greatly speeds up the calculation and so we can attain longer-time physics. There is no difficulty to relax these symmetry restrictions except slowing down the calculation. However, the results are not expected to be very different since there is no detectable symmetry-breaking instability in our problems. For both functionals we use a fairly large spatial step of about 1 Å, without any apparent loss of numerical accuracy.[15]

The time evolution starts from an excited e-bubble state, which means that the electron has been suddenly brought from the 1S onto the 1P or 2P state of the original spherical e-bubble. From this initial configuration, the superfluid helium then evolves according to

$$\frac{\partial\Psi}{\partial t} = -\frac{\imath}{\hbar}\left\{-\frac{\hbar^2}{2m_{He}}\Delta - \mu + \mathcal{U}_{He-He}[\rho,\mathbf{v}] + |\Phi|^2\,\frac{\delta V_{e-He}[\rho]}{\delta\rho}\right\}\Psi, \quad (4)$$

where the detailed form of the effective potential $\mathcal{U}_{He-He}[\rho,\mathbf{v}]$ can be found, e.g., in Refs. 24 and 25.

In the adiabatic approximation scheme, we do not evolve the electron in real-time but keep tracing the instantaneous eigenstates satisfying Eq. (3). In most cases, e-bubbles around excited electron states evolve toward configurations that are

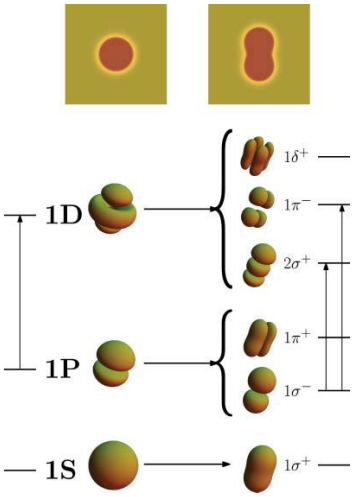

FIG. 2. Splitting of electronic levels along with a representation of their probability densities once the spherical symmetry is broken. The states in the spherical configuration (left) are labeled in the standard nL way. In the axially symmetric case (right) the label is nl_z^s, where $s = +(-)$ stands for symmetric (antisymmetric) states under specular reflection.

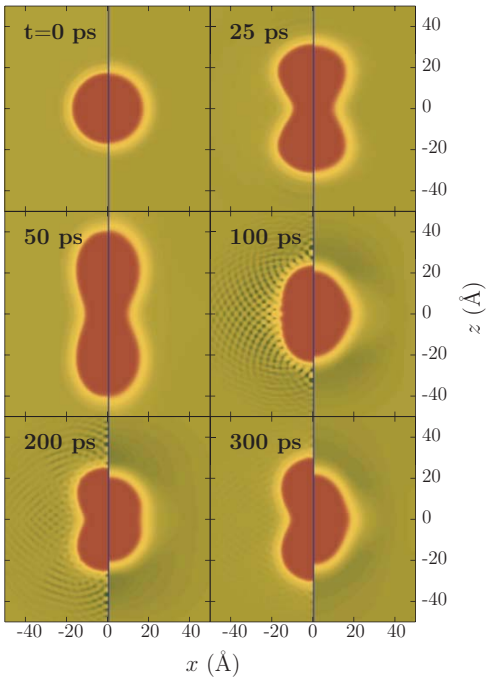

FIG. 3. Evolution of the 1P e-bubble at $P = 0$ bar. The left-hand side of each panel shows the results for the OT finite-range density functional plus adiabatic approximation for the electron. The right-hand side part of each panel shows the results for the ST zero-range density functional plus real-time evolution for the electron.

not spherically but axially symmetric. The originally degenerate angular momentum electron eigenstates in the spherical bubble now split according to the projection (m-values) on the symmetry z-axis, among which only the $\pm m$ states are still degenerate with each other. It is thus convenient to use the notation for the orbital angular momentum of single particle states in linear molecules, i.e., $\sigma, \pi, \delta, \phi, \ldots$ for $|m| = 0, 1, 2, 3, \ldots$ In addition to the axial symmetry, a nP bubble also keeps the original specular symmetry in the course of its evolution. Hence, one can construct the electron eigenbasis in such a way that the electron wavefunctions satisfy $\Phi(r, z, \theta) = \pm\Phi(r, -z, \theta)$. The correspondence between the lower lying spherically and axially symmetric electron states is displayed in Fig. 2 along with a representation of their probability densities. The superscript $+(-)$ denotes specularly symmetric (antisymmetric) states.

In the real-time dynamics scheme, the electron evolves according to

$$\frac{\partial \Phi}{\partial t} = -\frac{\imath}{\hbar}\left\{-\frac{\hbar^2}{2m_e}\Delta + V_{e\text{-}He}[\rho]\right\}\Phi\ . \tag{5}$$

We employ a fourth-order Runge–Kutta method to obtain the first time steps, and Hamming's method[26] for subsequent steps. A time step of 10^{-2} ps is chosen for the adiabatic scheme, and of 10^{-6} ps for the real-time dynamics scheme. These very different values reflect the mass ratio $m_e/m_{He} \sim 10^{-4}$. This is the reason that makes a dynamical evolution unaffordable when $\mathcal{E}_{He-He}[\rho]$ is finite-range, since updating the mean field is computationally very costly. Note that the original 1P and 2P levels are threefold degenerate, and that any of the substates (or a superposition of them) can be chosen as the initial state of the electron to start the evolution of the e-bubble. This choice influences the subsequent evolution because $|\Phi|^2$ in Eq. (4) depends on it. We have chosen to initially place the 1P (2P) electron in the $1\sigma^-(3\sigma^-)$ eigenstate because, since the m states are ordered in increasing $|m|$ values when the spherical nL manifold splits,[10] the dynamics of a $m \neq 0$ electron state can be destabilized by small fluctuations at an early stage of its evolution.

During the bubble evolution, sound waves released from its surface eventually reach the cell boundary. If no action is taken, they will bounce back spoiling the calculation. A way to handle this problem is to include some source of damping into Eq. (4) governing the fluid evolution, see e.g., Refs. 1,27, and 28. We have opted by making the replacement $\imath \longrightarrow \imath + \Lambda(\boldsymbol{r})$ in Eq. (4). This corresponds to a rotation of time axis in the complex plane by introducing a damping field $\Lambda(\boldsymbol{r})$, which takes the form[29]

$$\Lambda(\boldsymbol{r}) = \Lambda_0\left[1 + \tanh\left(\frac{s - s_0}{a}\right)\right], \quad s \equiv |\boldsymbol{r}|\ . \tag{6}$$

We keep the dimensionless parameter $\Lambda_0 \simeq 1.6$, and set $a = 5$ Å, $s_0 = 60$ Å in the finite-range calculation, and $a = 8$ Å, $s_0 = 90$ Å in the zero-range calculation. The evolution is damping-free [$\Lambda(\boldsymbol{r}) \ll 1$] in a sphere of radius $s < s_0 - 2a$, which is 50 Å in the finite-range case and 70 Å in the zero-range case. From Figs. 3–6 and the supplementary material[18] one can see that this region is large enough for the 1P e-bubble to expand inside a nondampening environment. For the 2P e-bubble evolution, we use a (r, z) calculation box of 150×150 Å^2 and $s_0 = 120$ Å, leaving ~ 100 Å of nondampening space for the bubble to expand.

The above prescription works extremely well, as it efficiently dampens the excitations of the macroscopic

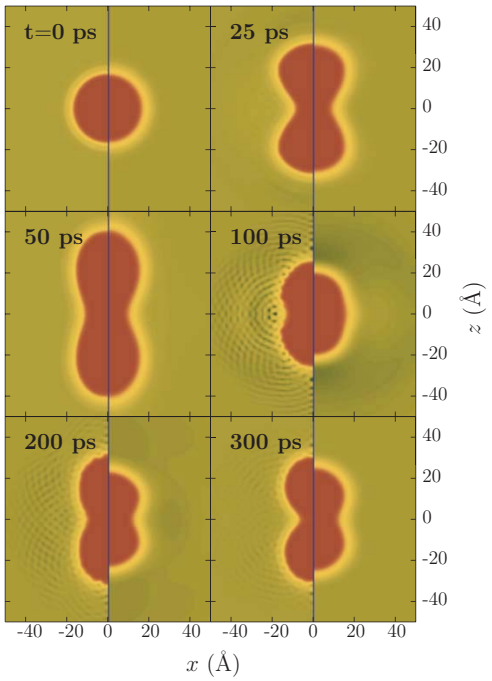

FIG. 4. Same as Fig. 3 at $P = 0.5$ bar.

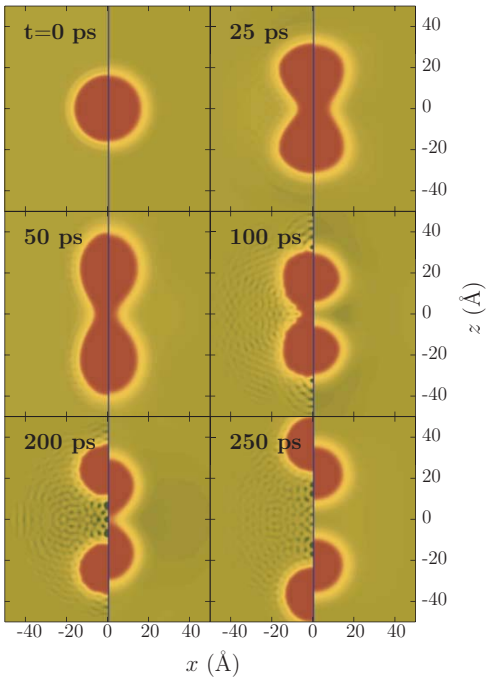

FIG. 5. Same as Fig. 3 at $P = 1$ bar.

wavefunction at the cell boundaries, and does not need a large buffer region to absorb the waves—actually we use the same box where the starting static calculations have been carried out.[14] It allows us to extend the adiabatic calculations of Ref. 15 from tens to hundreds of picoseconds.

III. RESULTS AND DISCUSSION

A. 1P e-bubble dynamics

1. Adiabatic versus real-time dynamical evolution

To some extent, an e-bubble in liquid helium is nearly a textbook example of an electron confined in a spherical-square-well potential. Its static properties are fairly insensitive to the complexities of the chosen functional provided the bulk and surface properties can be well reproduced.[12,13] In particular, a zero-range DF description of the 1S–1P absorption energies of the e-bubble as a function of P does not differ much from that obtained by a finite-range DF description.[3] This means that in some situations one may simply use a zero-range functional, which has an advantage of high computational speed.

Clearly, the dynamics of an e-bubble is much more involved than its statics. In our problems, the—nonspherical—squeezing and stretching of the bubble may cause its waist to shrink to a point when electron tunneling plays a role, and may also dissipate a large amount of energy by exciting elementary modes in the surrounding liquid. So, even if the static properties of the e-bubble are equally well described by both functionals, it is not obvious whether they yield a similar dynamical evolution for an excited e-bubble. This is the first issue we want to address.

We use two different schemes to compute the relaxation of a 1P e-bubble at $P = 0, 0.5, 1$, and 5 bars, and compare the results so obtained. One such scheme is the finite-range OT density functional description for helium with the adiabatic evolution for electron. The other scheme is the zero-range ST density functional description for helium with real-time evolution for the electron.

As can be seen in Figs. 3–6, the evolution starts with the bubble stretching along the z-axis and shrinking on its waist. After this stage, the bubble may continue oscillating and releasing energy into the liquid, eventually reaching a relaxed, metastable 1P state, or may split into two baby bubbles due to the liquid filling-in around the bubble waist. The density waves radiated to the liquid during this evolution take away a considerable part of the energy injected into the system during the absorption process, i.e., 105 meV at $P = 0$ and 148 meV at 5 bar.[3]

In Figs. 3–6 we compare the bubble evolution obtained within the two frameworks for different pressures. At a first glance, both dynamics are nearly equivalent during the first 50 ps, starting to differ from this time on although they are still qualitatively similar. A more detailed analysis, focused on three key elements of the density profiles, indicates the following:

(a). The shape of the bubble surface, defined as the locus where the liquid density equals half the saturation density value ρ_0, e.g., 0.0218 Å^{-3} at $P = 0$ bar. This shape determines the most crucial properties of an e-bubble. From this shape, we know whether the bubble is simply connected or has split. Up to $t \lesssim 50$ ps, the shape of the bubble is nearly identical in both descriptions. At later times, the bubble shape changes at a slower pace in the ST than in the OT description.

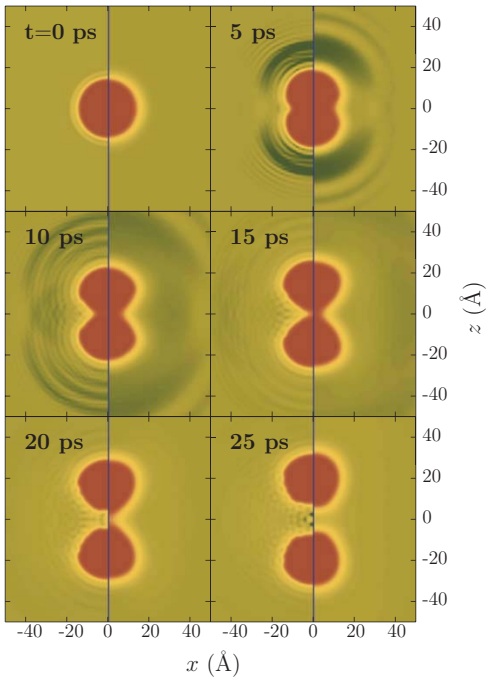

FIG. 6. Same as Fig. 3 at $P = 5$ bar.

Figure 7 illustrates the time evolution of the bubble surface. In particular, the top panel shows the evolution of the point on the bubble surface at $r = 0$ with $z > 0$. This represents half the longitudinal extent of the e-bubble. One can see that this length oscillates in the ST calculation with a lower frequency than in the OT one. Notice that superfluidity is instrumental to keep the bubble surface oscillating without appreciable dampening (yet some energy is still released to the liquid). If helium were in the normal state, these oscillations would be washed out more quickly due to viscosity effects, likely raising the pressure threshold at which the bubble splits.

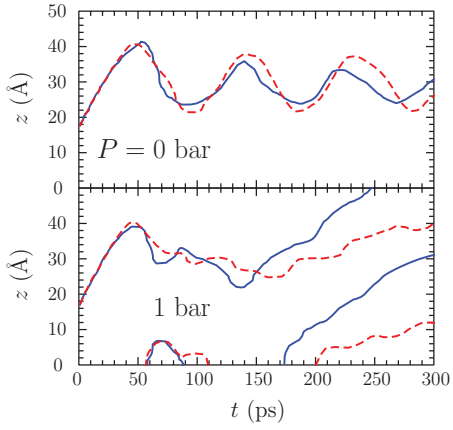

FIG. 7. Evolution of the extent of the bubble along the z-axis at $P = 0$ and 1 bar. The solid line is the OT finite-range result, and the dashed line is the ST zero-range result.

If the bubble symmetrically splits into two baby bubbles, there are two such points, as can be seen in the bottom panel for $P = 1$ bar. We have found that, besides the moment at which the distance between the baby bubbles increases steadily—about 175 ps for the OT functional and 200 ps for ST functional—there is a time interval between ~60 and ~90 ps for the OT functional, and ~60 and ~110 for the ST functional, where the 1P bubble at $P = 1$ bar has split but the emerging baby bubbles are "locked" by the shared electron that exerts some attractive force on them, forcing them back to a simply connected configuration. Eventually, the baby bubbles are unlocked and the distance between them grows.

(b). The surface thickness of the bubble, defined as the width of the region satisfying $0.1\rho_0 \leq \rho(\boldsymbol{r}) \leq 0.9\rho_0$. The thickness of the bubble surface has been found to be nearly independent of the local surface curvature at anytime during the evolution, see also Ref. 15. It is about 1 Å larger in the ST than in the OT description,[17,30] as can be seen in Figs. 3–6 (the blurrier the bubble–helium interface, the larger the surface thickness). The zero temperature OT result, about 6 Å, is in agreement with the experimental findings.[31,32]

(c). The density oscillations traveling through the liquid. This is the point at which the differences between the two functionals become more apparent. The density waves produced by the ST functional have much larger wavelengths because this approach cannot sustain short wavelength inhomogeneities due to the huge energy cost from the $|\nabla\rho(\boldsymbol{r})|^2$ surface energy term. The OT functional has not such a term and is free from this drawback. Roughly speaking, the short wavelength waves arising in the OT approach are smeared out in a sort of big *tsunami* in the ST case, see for instance the panels corresponding to $t = 5$ and 10 ps in Fig. 6. It is worth emphasizing that the wave interference pattern found in the OT description is not an artifact produced by waves bouncing back from the box boundaries, as those are already washed out by the damping term. It arises from the interference of waves produced at different points on the e-bubble surface.

We estimated in Ref. 15 that the first wave front was moving at supersonic velocities, about 330 m/s at $P = 0$ and 410 m/s at $P = 5$ bar. This rises the interesting question of whether shock waves[33] are generated by the displacement of the surface of the bubble. As a matter of fact, a shock wave was launched in the spherical expansion of a highly compressed electron bubble.[1] This wave travelled at supersonic velocities (560 m/s), while the subsequent fronts moved at the speed of sound, some 240 m/s. The analysis carried out by these authors was facilitated by the spherical geometry of the expansion that allowed them to use a very large box for this one-dimensional problem. In our case, the problem is three-dimensional, the wave fronts have a more complex structure and our numerical scheme does not allow to confirm nor discard the appearance of shock waves in the superfluid. In particular, it does not allow us to distinguish between a very distorted density profile, like that we have shown in Fig. 6 of Ref. 15, and a discontinuity in the density and pressure profile characterizing shock waves.[33] Since there is no reason to believe that geometry plays any fundamental role, we are prone to suggest that when the energy released to the liquid is large

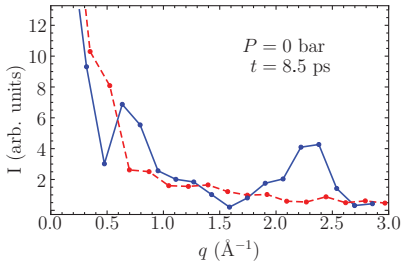

FIG. 8. Fourier transform of the density fluctuation along the z-axis within the region 30 Å $\leq z \leq$ 70 Å for the expansion process of the 1P e-bubble at $P = 0$ bar and $t = 8.5$ ps. The solid line corresponds to the OT calculation, and the dashed line corresponds to the ST functional calculation. The lines have been drawn as a guide to the eye.

enough, as in the 1P to 1S de-excitation at high pressures, or in the 2P to 1S de-excitation, the first launched front is indeed a shock wave.

To quantitatively study the nature of the waves emitted during the bubble evolution, we perform a Fourier analysis of the density profile along the symmetry axis, restricting it to the region 30 Å $\leq z \leq$ 70 Å, away from the bubble location to avoid uncontrolled effects arising from the bubble itself. The Fourier transform of the density fluctuation is shown in Fig. 8 at $t = 8.5$ ps and $P = 0$ bar. While both functionals generate low-q density waves in the phonon region (see Fig. 1) the ST approach does not display any structure, whereas in the OT approach one can identify two distinct peaks. The higher one is located at $q \sim 0.8$ Å^{-1} near the maxon region, and the lower one is located at $q \sim 2.3$ Å^{-1} close to the roton minimum.

With these results on the evolution of the 1P e-bubble in mind, we can state with some confidence that the ST description is accurate enough for describing the fate of the e-bubble, yielding the appropriate final topology at a given pressure, and a more than qualitative picture of its evolution. The shape of the cavity, which is responsible for most electron properties, is essentially the same in both ST and OT descriptions. The different way of energy release associated with their each kind of elementary excitation may yield somewhat diverse evolutions at longer times, but it has little relevance for the problems at hand. One should keep in mind, however, that if the actual subject of the study are the elementary excitations of the bulk liquid, the use of the OT functional is then unavoidable.

We also want to stress that computing the 1P e-bubble dynamics in real time for the ST functional has allowed us to explicitly check the adiabatic approximation in the electron evolution during the time interval relevant for the e-bubble "fission."[15] We have computed the overlap between the time-evolving electron wave function and the instantaneous eigenstate $1\sigma^-$, and have found it to be equal to unity at all times, meaning that the adiabatic approximation holds. As we will discuss later on, this is not the case for the 2P e-bubble.

2. Time-resolved absorption spectrum

Within the OT functional plus adiabatic approximation scheme, we have studied the excitation of 1P bubbles by

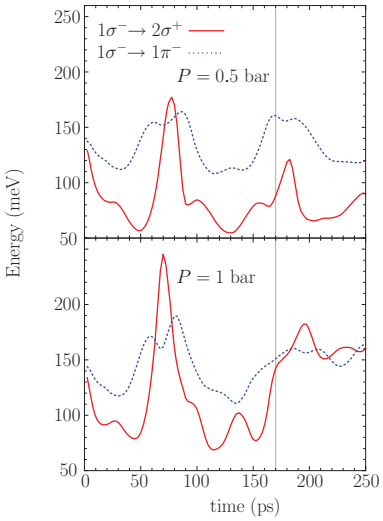

FIG. 9. Time-resolved absorption energies at $P = 0.5$ and 1 bar for the 1P e-bubble evolution. The thin vertical line at $t = 170$ ps indicates the time at which the bubble splits in the $P = 1$ bar case.

photoabsorption either to the $m = 0$ component ($2\sigma^+$), or to the $m = \pm 1$ components ($1\pi^-$), arising from the splitting of the originally spherical 1D state, see Fig. 2. In principle, this can be measured in a pump-probe experiment by which the e-bubble is excited by two consecutive laser pulses. The delay set between these pulses corresponds to the time interval between the excitation and the measurement, which is the same as the time defined in our calculations. The intensity of the absorption lines is characterized here by their oscillator strength calculated in the dipole approximation[34]

$$f_{ab} = \frac{2m_e}{3\hbar^2}(E_a - E_b)\left|\langle a|\boldsymbol{r}|b\rangle\right|^2 . \tag{7}$$

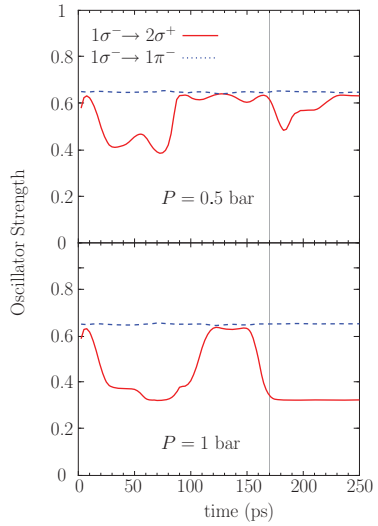

FIG. 10. Time-resolved absorption oscillator strengths at $P = 0.5$ and 1 bar for the 1P e-bubble evolution. The thin vertical line at $t = 170$ ps indicates the time at which the bubble splits at $P = 1$ bar.

We recall that this oscillator strength fulfills the sum rule $\sum_a f_{ab} = 1$, but is generally not positive definite. If the initial state is not the ground state, a partial sum may be greater than unity.

Starting from the 1P electron state $1\sigma^-$ ($m = 0$), the two possible photoexcitation transitions are $1\sigma^- \to 2\sigma^+$ and $1\sigma^- \to 1\pi^-$, see Fig. 2. The specularly asymmetric states have a nodal point on the $z = 0$ symmetry plane implying that they are rather insensitive to the presence of helium in that plane. Therefore, the transition energy for excitations between two asymmetric states should not depend much on whether the bubble has split or not. Contrarily, the specularly symmetric states do not have such a nodal point, and so are more sensitive to splitting. The lowest-lying transition connecting specularly asymmetric with specularly symmetric states may thus probe the topology of the bubble, since the absorption energy for this transition should increase by a sizeable amount when the bubble splits. The level structure at the right part of Fig. 2 may help understanding these issues.

The time-resolved absorption energies and oscillator strengths of the evolving 1P bubble for $P = 0.5$ and 1 bar are presented in Figs. 9 and 10. As shown by our calculations, the 1P bubble does not split for $P = 0.5$ bar, but it does for $P = 1$ bar at $t \simeq 170$ ps. The bubble splitting yields a clear signature in the energies and the oscillator strengths: the evolution of the transition energies is similar for $P = 0.5$ and 1 bar before the splitting, but when the bubble splits at $P = 1$ bar, the $1\sigma^- \to 2\sigma^+$ energy rapidly increases by ~ 70 meV, becoming comparable to the $1\sigma^- \to 1\pi^-$ energy. This is a consequence of the change in the bubble topology, which makes the final symmetric and antisymmetric states nearly degenerate.

A conspicuous pattern also appears in the evolution of the oscillator strength. The strength for the specularly asymmetric transition $1\sigma^- \to 1\pi^-$ remains nearly constant at $f \sim 0.65$, whereas the strength for the specularly symmetric transition $1\sigma^- \to 2\sigma^+$ oscillates when the bubble is simply connected but falls down to $f \sim 0.32$ when the bubble splits. This is again a consequence of the near degeneracy of symmetric and asymmetric states in the split-bubble regime. The oscillator strength for the antisymmetric transition is a factor of 2 larger than that of the symmetric transition in the split-bubble regime because the final state $1\pi^-$ is twofold degenerate.[35]

We thus conclude that time-resolved absorption energies are of practical interest because they bring rich information on the bubble shape and can be determined in experiments. This may shed light on the longstanding question about whether 1P e-bubbles under pressure do really "fission" into two baby bubbles as our calculations indicate, and how the electron wavefunction collapses into one of them, without violating the quantum measurement axiom.

B. 2P e-bubble dynamics: the breakdown of adiabaticity

Our previous analysis of the dynamics of the 1P e-bubble has shown that one does not need to use the accurate OT functional to describe this process. The much simpler ST approach already yields a fair description. This is particularly useful when we move to the study of the 2P e-bubble dynamics. An attempt to simulate this evolution has been made within the OT approach and the adiabatic approximation.[15] This could only be performed for a few picoseconds, as it was shown that the adiabatic approximation fails at $t \simeq 7.4$ ps. This failure is due to the approaching of the $3\sigma^-$ (arising from the spherical 2P level) and $2\sigma^-$ (arising from the spherical 1F level) energy levels. By using the efficient real-time ST scheme, we now relax the adiabatic approximation, following the evolution of the 2P e-bubble for several hundreds of picoseconds. We keep referring to this bubble as a "2P e-bubble," but should have in mind that once the adiabatic approximation breaks down, the electron is no longer in the original eigenstate. Generally, it is in a superposition of states that have the same quantum numbers as the initial state, here meaning that it can be in any superposition of σ^- states.

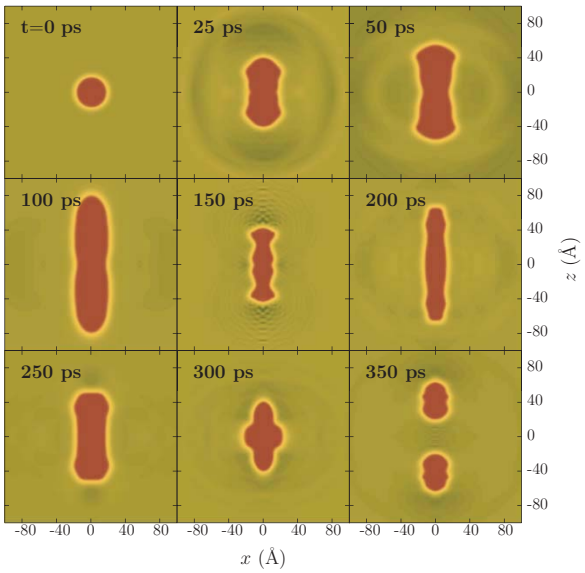

FIG. 11. Evolution of the 2P e-bubble at $P = 0$ bar using real-time dynamics and the ST zero-range functional.

The 2P bubble evolution is shown in Fig. 11. For the first 100 ps, the shape evolution of the 2P bubble is similar to that of the 1P bubble, as it expands along the symmetry z-axis while its waist shrinks in the perpendicular plane. From this point on, the bubble oscillates back and forth in a kind of four-lobe shapes quite different from those seen in the 1P bubble. We attribute these conspicuous shape variations to the breaking down of the adiabatic approximation as the electron moves from a eigenstate to a nontrivial superposition of those compatible with the symmetries of the system. After evolving for ~325 ps, the 2P bubble splits into two baby bubbles.

We present in Fig. 12(a) the evolution of the *instantaneous* eigenenergies of the first σ^- states. As can be seen in panel (b), the $2\sigma^-$ and $3\sigma^-$ states nearly meet at $t \simeq 7.4$ ps. In agreement with some well-known results from basic quantum mechanics,[36] we have found that this situation corresponds to an avoided crossing. Panel (c) shows the overlap of the evolving electron wavefunction with the relevant instantaneous eigenstates. The electron is initially in a $3\sigma^-$ state (the overlap is unity), but at the point of avoided crossing the

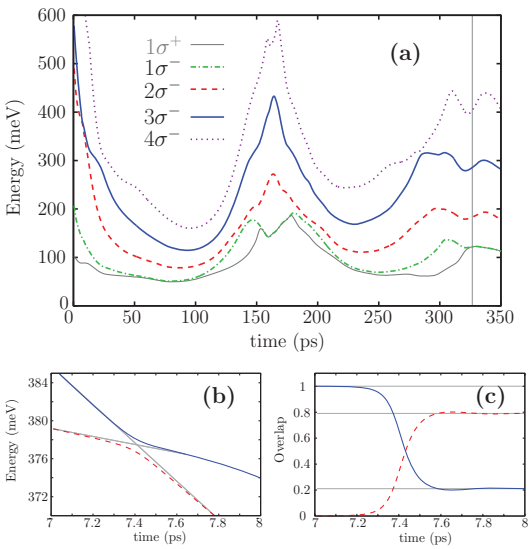

FIG. 12. (a): Lower-lying *instantaneous* σ^- eigenstates together with the $1\sigma^+$ eigenstate of the 2P e-bubble at $P = 0$ bar as a function of time. The thin vertical line at $t = 325$ ps indicates the time at which the bubble splits. (b) Enlarged view of the region where the $3\sigma^-$ and $2\sigma^-$ states repel each other. (c) Overlap of the time-evolving electron state onto the $3\sigma^-$ (solid line) and $2\sigma^-$ eigenstates (dashed line), $|\langle\Phi(\boldsymbol{r}, t)|n\sigma^-\rangle|^2$. The adiabatic approximation fails if the value of this overlap varies in time.

adiabaticity is lost: the electron state is a superposition of the $2\sigma^-$ ($\sim 80\%$) and $3\sigma^-$ ($\sim 20\%$) states.

We have also found a time interval between $\sim$155 and $\sim$180 ps when the 2P bubble at $P = 0$ bar has split but the emerging baby bubbles do not go away. When this happens, the $n\sigma^-$ and $n\sigma^+$ states should be degenerate. This is illustrated in panel (a) of Fig. 12 for the $n = 1$ states. Notice from Fig. 11 that in the 50 ps $\lesssim t \lesssim$ 100 ps interval the bubble is simply connected and the apparent degeneracy displayed in Fig. 12(c) is due to the energy scale. The same thing happens around $t \sim 230$ ps.

IV. SUMMARY

We have thoroughly studied the dynamical evolution of 1P and 2P excited electron bubbles in superfluid ^{4}He at zero temperature. To this end, we have resorted to zero- and finite-range density functionals, establishing how reliable the former is by comparing its results with those obtained with the latter.

Although the results obtained for the 1P bubble evolution from these two functionals show some quantitative differences, especially for long-time evolutions, they are qualitatively equivalent. In particular, both lead to the conclusion that 1P bubbles "fission" at pressures above 1 bar. The ST functional result is of particular relevance, as it has been obtained by a real-time evolution, without assuming the adiabaticity of the process. This confirms the previous results obtained using the finite-range OT functional and the adiabatic approximation for much shorter periods of time than in the present work.[15]

Some indirect experimental evidence indicates a change in the de-excitation behavior of the 1P e-bubble as pressure increases.[12,16] We have explored here the possibilities offered by the photoabsorption spectrum of the 1P e-bubble to disclose whether such a bubble de-excites by "fission" or by a more conventional radiative decay, and have obtained the signatures that would help distinguish between both decay channels. Although far from trivial, a pump-probe experiment may detect a change in the absorption spectrum of the 1P bubble associated with the appearance of the two baby bubble de-excitation channel.

Finally, we have studied the evolution of the 2P e-bubble in real-time within the ST functional approach. We have dynamically found that the adiabatic approximation does not hold at any positive pressure confirming the results obtained within the OT plus adiabatic approximation approach.[15] Negative pressures, as those attained in cavitation experiments, have not been studied. The physical realization of a relaxed, metastable 2P configuration is discarded.

ACKNOWLEDGMENTS

The authors wish to thank Humphrey Maris for helpful discussions. This work was performed under Grant Nos. FIS2008-00421/FIS from DGI, Spain (FEDER), and 2009SGR1289 from Generalitat de Catalunya. D.M. has been supported by the Spanish MEC-MICINN through the FPU fellowship program, Grant No. AP2008-04343. D.J. has been supported by the National Science Foundation of the United States through Grant No. DMR-0605355.

[1] J. Eloranta and V. A. Apkarian, J. Chem. Phys. **117**, 10139 (2002).
[2] A. Ghosh and H. J. Maris, Phys. Rev. Lett. **95**, 265301 (2005).
[3] V. Grau, M. Barranco, R. Mayol, and M. Pi, Phys. Rev. B **73**, 064502 (2006).
[4] M. Rosenblit and J. Jortner, J. Chem. Phys. **124**, 194505 (2006); *ibid.* **124**, 194506 (2006).
[5] M. Pi, R. Mayol, A. Hernando, M. Barranco, and F. Ancilotto, J. Chem. Phys. **126**, 244502 (2007).
[6] L. Lehtovaara and J. Eloranta, J. Low Temp. Phys. **148**, 43 (2007).
[7] H. J. Maris, J. Phys. Soc. Jpn. **77**, 1 (2008).
[8] W. Guo, D. Jin, G. M. Seidel, and H. J. Maris, Phys. Rev. B **79**, 054515 (2009).
[9] F. Ancilotto, M. Barranco, and M. Pi, Phys. Rev. B **80**, 174504 (2009).
[10] D. Mateo, A. Hernando, M. Barranco, and M. Pi, J. Low Temp. Phys. **158**, 397 (2010).
[11] D. Jin and H. J. Maris, J. Low Temp. Phys. **158**, 317 (2010).
[12] C. C. Grimes and G. Adams, Phys. Rev. B **41**, 6366 (1990).
[13] C. C. Grimes and G. Adams, Phys. Rev. B **45**, 2305 (1992).
[14] D. Jin, W. Guo, W. Wei, and H. J. Maris, J. Low Temp. Phys. **158**, 307 (2010).
[15] D. Mateo, M. Pi, and M. Barranco, Phys. Rev. B **81**, 74510 (2010).
[16] H. J. Maris, A. Ghosh, D. Konstantinov, and M. Hirsch, J. Low Temp. Phys. **134**, 227 (2004).
[17] F. Dalfovo, A. Lastri, L. Pricaupenko, S. Stringari, and J. Treiner, Phys. Rev. B **52**, 1193 (1995).
[18] See supplementary material at http://dx.doi.org/10.1063/1.3544216 for movies of the dynamical evolution of electron bubbles.
[19] E. Cheng, M.W. Cole, and M.H. Cohen, Phys. Rev. B **50**, 1136 (1994); Erratum Phys. Rev. B **50**, 16134 (1994).
[20] S. Stringari and J. Treiner, Phys. Rev. B **36**, 16 (1987); J. Chem. Phys. **87**, 5021 (1987).
[21] D. Mateo, J. Navarro, and M. Barranco, Phys. Rev. B **82**, 134529 (2010).
[22] R. J. Donnelly, J. A. Donnelly, and R. N. Hills, J. Low Temp. Phys. **44**, 471 (1981).

[23]M. Frigo and S. G. Johnson, Proc. IEEE **93**, 216 (2005).
[24]L. Giacomazzi, F. Toigo, and F. Ancilotto, Phys. Rev. B **67**, 104501 (2003).
[25]L. Lehtovaara, T. Kiljunen, and J. Eloranta, J. Comput. Phys. **194**, 78 (2004).
[26]A. Ralston and H. S. Wilf, *Mathematical Methods for Digital Computers* (John Wiley and Sons, New York, 1960).
[27]C. Cerjan, D. Kosloff, R. Kosloff, and M. Reshef, Geophysics **50**, 705 (1985).
[28]D. Neuhauser and K. Lopata, J. Chem. Phys. **129**, 134106 (2008).
[29]D. Jin and W. Guo, Phys. Rev. B **82**, 094524 (2010).
[30]J. Dupont-Roc, M. Himbert, N. Pavloff, and J. Treiner, J. Low Temp. Phys. **81**, 31 (1990).
[31]J. Harms, J. P. Toennies, and F. Dalfovo, Phys. Rev. B **58**, 3341 (1998).
[32]K. Penanen, M. Fukuto, R. K. Heilmann, I. F. Silvera, and P. S. Pershan, Phys. Rev. B **62**, 9621 (2000).
[33]L. Landau and E. Lifchitz, *Mécanique des Fluides* (Éditions Mir, Moscow, 1971).
[34]M. Weissbluth, *Atoms and Molecules* (Academic, New York, 1978).
[35]Fig. 10 displays the oscillator strength *per energy level* and not *per state*. π states are twofold degenerate due to the two possible l values, $l = \pm 1$, while σ states are nondegenerate as $l = 0$. For this reason, when these states become nearly degenerate in the split-bubble regime, one transition has $f \sim 0.32$ and the other $f \sim 0.65$, a factor of 2 larger.
[36]E. Teller, J. Phys. Chem. **41**, 1 (1937).

3.3 Translational dynamics of photoexcited atoms in ^{4}He nanodroplets: The case of silver

Resumen (Spanish)

La dinámica de translación seguida por átomos de plata en nanogotas de ^{4}He tras las transiciones $5p\,^2\mathrm{P}_{1/2} \leftarrow 5s^2\mathrm{S}_{1/2}$ y $5p\,^2\mathrm{P}_{3/2} \leftarrow 5s^2\mathrm{S}_{1/2}$ se ha investigado en una colaboración teórico-experimental. Experimentalmente, se ha observado que los átomos de Ag son expulsados tras la excitación al estado $^2\mathrm{P}_{1/2}$ con una distribución de velocidades cuyo máximo se encuentra hacia los 55 m/s. Cuando la plata se excita al estado $^2\mathrm{P}_{3/2}$ se encuentra una rica fenomenología: unas veces la impureza permanece solvatada y las veces que es expulsada lo hace o bien en forma de átomo de Ag o bien como exciplex de AgHe con una distribución de velocidad similar (aunque no idéntica) a la del estado $^2\mathrm{P}_{1/2}$.

Analizamos estos resultados mediante un esquema del funcional de la densidad tridimensional dependiente del tiempo. La dinámica del complejo Ag-$^4\mathrm{He}_{1000}$ se ha seguido durante varias decenas de picosegundos, tiempo suficiente para observar la formación en tiempo real de exciplexes en la gota y la expulsión de los átomos de Ag de la misma.

Translational dynamics of photoexcited atoms in ^{4}He nanodroplets: the case of silver

David Mateo,[1] Alberto Hernando,[2] Manuel Barranco,[1] Evgeniy Loginov,[3] Marcel Drabbels,[3] and Martí Pi[1]

[1] *Departament ECM, Facultat de Física, and IN^{2}UB, Universitat de Barcelona. Diagonal 645, 08028 Barcelona, Spain*

[2] *Laboratoire Collisions, Agrégats, Réactivité, IRSAMC, Université Paul Sabatier 118 route de Narbonne 31062 - Toulouse CEDEX 09, France*

[3] *Laboratoire de Chimie Physique Moléculaire, Swiss Federal Institute of Technology Lausanne (EPFL), CH-1015 Lausanne, Switzerland*

(Dated: March 13, 2013)

The dynamics following the photoexcitation of Ag atoms in ^{4}He nanodroplets via the $5p\,^2\mathrm{P}_{1/2} \leftarrow 5s^2\mathrm{S}_{1/2}$ and $5p\,^2\mathrm{P}_{3/2} \leftarrow 5s^2\mathrm{S}_{1/2}$ transitions has been investigated in a joint experimental and theoretical effort. It has been experimentally found that upon excitation to the $^2\mathrm{P}_{1/2}$ state, the Ag atoms are ejected with a speed distribution peaking at about 55 m/s. When Ag is excited to the $^2\mathrm{P}_{3/2}$ state, a rich phenomenology is found. While a fraction of the impurities remains solvated, the impurities that are ejected from the droplets either as Ag or AgHe have speed distributions similar, but not identical, to those found for excitation to the $^2\mathrm{P}_{1/2}$ state. The experiment findings are qualitatively analyzed within a three-dimensional, time-dependent density functional approach for the helium droplet. The dynamics of the Ag-$^4\mathrm{He}_{1000}$ system has been followed for several tens of picoseconds, long enough to observe AgHe exciplex formation and the departure of the photoexcited Ag atom from the helium droplet.

PACS numbers: 36.40.-c, 32.30.Jc, 78.40.-q, 67.25.-k

I. INTRODUCTION

The effect of the strong perturbations induced by electronic excitation of impurities in helium droplets is a subject of growing interest.[1–3] This is motivated by the idea that insight into the dynamical evolution of an electronically excited impurity in helium droplets is a first step towards a better understanding of chemical reactions in this quantum environment. With this goal in mind, we have recently undertaken a joint experimental and theoretical study of the desorption of alkali atoms from the surface of ^{4}He nanodroplets following excitation via the $(n+1)s \leftarrow ns$ transition.[4] The subsequent dynamical evolution of both the excited impurity and helium droplet was followed within a time-dependent density-functional (TDDF) approach. This has allowed us to characterize the physical observables and successfully compare them with experiment. Moreover, the calculations have disclosed the dramatic effect that the excitation of the impurity causes on the hosting droplet, generating density waves that propagate at supersonic velocities.[4]

The aim of the present work is to extend this work and gain insight into the dynamics of photoexcited atoms residing in the bulk of helium droplets. Silver atoms are especially appealing as probe for such studies. The spectroscopy and the photoinduced dynamics of silver atoms in both liquid helium and in helium droplets has been thoroughly investigated by a wide variety of experimental techniques.[5–10] The system has also been addressed theoretically. The solvation structure and absorption spectrum of a silver impurity in helium droplets have been calculated using methods and interaction potentials of different complexity and accuracy.[11–13] In addition, the photoexcitation dynamics of a silver atom embedded in a $^4\mathrm{He}_{200}$ cluster has been simulated up to 2.5 ps using a quantum molecular dynamics approach.[11]

These studies have revealed that the dynamical processes induced by the photoexcitation of the solvated silver atom are very complex and depend strongly on the character of the excited state. In the experiments involving helium droplets, it was found that the excited silver atoms are ejected from the helium droplets.[9,10] The underlying mechanism is not exactly known, but is expected to be related to the repulsive interaction between the excited silver atom and the helium at long-range. It has been speculated that as a result the excited silver atom is transported towards the surface of the helium droplet from which it then desorbs.[9] If correct, this mechanism allows to probe the translational dynamics of the excited silver atoms in helium and test for the possible existence of a critical velocity in helium droplets. In the current work we analyze the velocity distributions of the ejected silver atoms and compare them qualitatively with the results of simulations. Besides providing insight into the translational dynamics, the simulations also allow to have a first glimpse at exciplex formation. The underlying TDDFT-based model, which explicitly takes into account spin-orbit interactions in order to describe non-radiative transitions between excited ^{2}P states, is widely applicable. While here it is used to describe the dynamical evolution of the Ag@$^4\mathrm{He}_N$ complex after dipole excitation, the method can be readily adapted to other dopants and/or excitations.

This paper is organized as follows. In Sec. II we briefly recall the experimental findings of Ref. 10 complemented with some material recently obtained. Basic details of the theoretical approach are presented in Sec. III. In Sec. IV we present a semi-quantitative comparison of the numer-

ical results with the experimental data. A summary is presented in Sec V. For illustrative purposes, we present in the Appendix a discussion about the influence of the helium density profile on the absorption spectrum, by comparing two different density-functional approaches.

II. EXPERIMENTAL

A. Setup

Details of the experimental setup have been reported in previous publications.[10,14] In short, helium droplets consisting of several thousands of atoms are formed by expanding helium gas at a pressure of 30 bar into vacuum through a 5 μm orifice cooled to cryogenic temperatures. The size distribution of these droplets can be systematically varied by changing the source temperature.[15] As the helium droplets pass through an oven containing silver metal they on average pick up less than one silver atom. Via a differential pumping stage the doped droplets enter a velocity map imaging spectrometer. At the center of the spectrometer the droplet beam is crossed at right angles by two counter-propagating laser beams. The frequency-doubled output of a Nd:YAG pumped dye laser excites the embedded silver atoms to the 5p state. The excited silver atoms are subsequently ionized by the absorption of an additional photon provided by another Nd:YAG pumped dye laser. Both laser beams have their polarization parallel to the molecular beam axis. The generated ions are projected onto a position sensitive detector consisting of a pair of microchannel plates and a phosphor screen. A high-resolution CCD camera records images of the phosphor screen which are analyzed online to determine the centroids of the ion impacts. The velocity distributions of the ions are determined by performing an inverse Abel transform on the image constructed from the accumulated centroids.

B. Results

Most of the experimental results related to the dynamical evolution of excited silver atoms in helium nanodroplets have already been reported.[10] Hence, we will only briefly summarize those findings here. In addition, we will present recent results on the velocity distributions of the silver products ejected from the droplets.

The $5p \leftarrow 5s$ excitation spectrum of silver atoms in helium droplets consisting on average of 2700 helium atoms is shown in Fig. 1. It is characterized by two well-separated broad resonances that are significantly shifted with respect to the $5p\ ^2\mathrm{P}_{1/2} \leftarrow 5s\ ^2S_{1/2}$ (D1) and $5p\ ^2\mathrm{P}_{3/2} \leftarrow 5s\ ^2\mathrm{S}_{1/2}$ (D2) transitions in the free atom. It was found that the dynamical evolution of the system is very different when exciting the embedded silver atoms via the two resonances. Excitation at the nominal D1 transition leads to ejection of $^2\mathrm{P}_{1/2}$ excited silver atoms

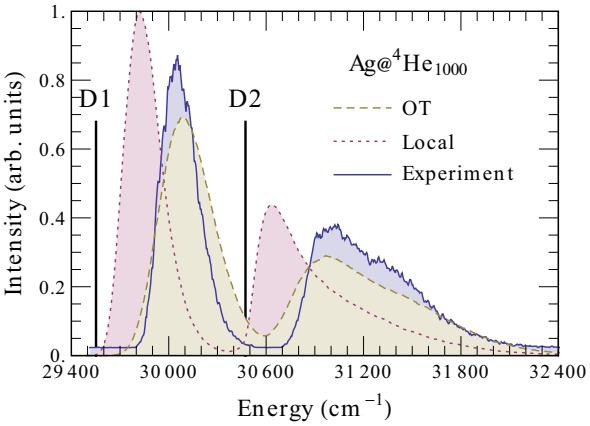

FIG. 1: (Color online) Experimental (solid line) absorption spectrum of Ag in a ^{4}He droplet with about 2700 atoms, compared with the calculated spectrum for Ag@^{4}He$_{1000}$. Dashed line, Orsay-Trento non-local functional; dotted line, local functional (see Appendix). The spectra have been normalized so that their integral is unity. The D1 and D2 transitions of the free Ag atom are also shown (vertical lines).

with an efficiency of nearly 100%. In contrast, when excited at the D2 transition only 58% of the excited atoms is ejected from the droplets. This implies that in order to compare the excitation spectrum presented in Fig. 1 with calculated absorbtion spectra, the intensity of D2 transitions has to be corrected accordingly. Whereas excitation via the D1 transition yields almost exclusively silver atoms as products, excitation via the D2 transition yields Ag, AgHe and $AgHe_2$, with a branching ratio of 0.82:0.17:0.01. The ejected Ag and AgHe products are found to mainly populate the $^2\mathrm{P}_{1/2}$ state, indicating the existence of an efficient relaxation pathway which most likely involves the $^2\mathrm{D}_{5/2}$ state. Based on photoelectron and ZEKE spectra it was concluded that the Ag that remains solvated populates both spin-orbit states.

To gain insight into the translational dynamics of the excited silver atoms, velocity distributions of the ejected atoms have been determined by recording velocity map images. Fig. 2 shows three ion images corresponding to Ag ($^2\mathrm{P}_{1/2}$) and AgHe products resulting from the excitation via the D1 and D2 bands of silver atoms embedded in helium droplets consisting on average of 2700 helium atoms. Inspection of the images reveals that they are all very similar and are characterized by an isotropic angular distribution. These observations are in strong contrast to what has been found for species residing on the surface of helium droplets. For these systems the images reveal anisotropic angular distributions and a strong dependence on the excitation frequency.[4,16–18] The isotropy observed in the present study is a direct consequence of the impurity being solvated inside the droplet, as a result of which no preferred axis can be defined on the length scale of the excitation and the electronic matrix element

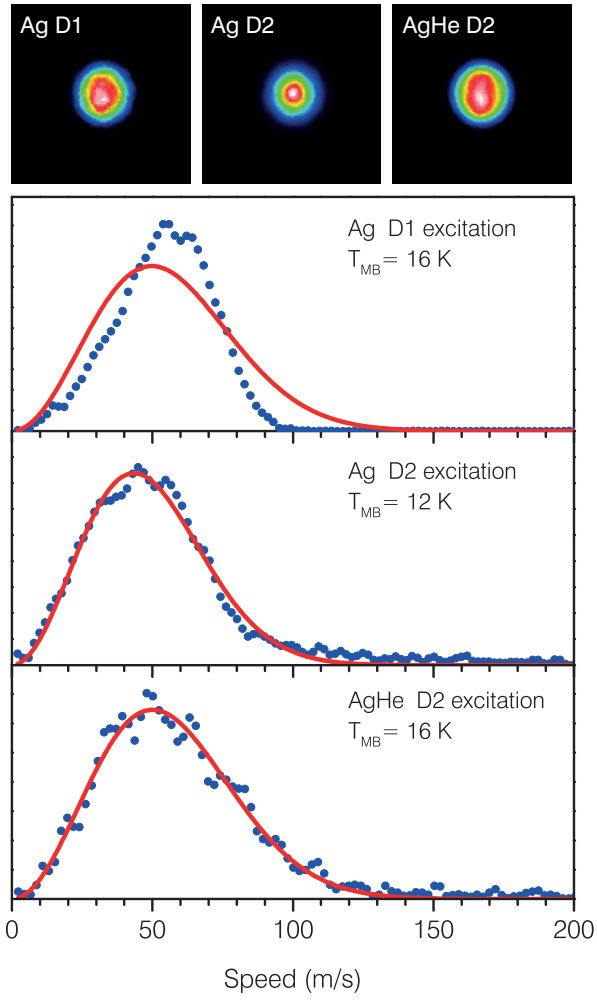

FIG. 2: (Color online) Velocity map images of Ag and AgHe products recorded following excitation via the D1 and D2 bands of Ag atoms in helium droplets consisting on average of 2700 atoms and the corresponding speed distributions. The solid lines are the results of fits to Maxwell-Boltzmann distributions.

becomes constant.[4]

More quantitative information on the translational motion of the excited silver atoms can be obtained from the speed distributions derived from these images. The speed distributions of the three different products shown in Fig. 2 are very similar. They all peak in the velocity range of 50-60 m/s, but there are noticeable differences in shape and width. This difference becomes especially obvious when trying to associate a translational temperature with these speed distributions by fitting them to a Maxwell-Boltzmann distribution. Those corresponding to excitation of the ^{2}P$_{3/2}$ state yield a good fit with translational temperatures of 12 K and 16 K for Ag and AgHe, respectively. In contrast, the speed distribution corresponding to excitation of the ^{2}P$_{1/2}$ state cannot be described by this functional form; it decreases much more rapidly than predicted by a Maxwell-Boltzmann distribution. It should be noted that the speed distribution of the ^{2}P$_{1/2}$ state is also noticeably different from those found for photofragments or ions escaping from helium droplets,[14,19–22] indicating that different process are underlying these speed distributions. Since the most probable speed is close to the Landau velocity $v_L \sim 60$ m/s at which rotons are created in the liquid,[23,24] it is tempting to relate the observed speed distributions to the existence of a critical velocity in the helium droplets. In an effort to establish whether such a relation actually exists, the dynamical evolution of the system has been modeled using a time-dependent density functional approach.

III. THEORETICAL APPROACH

Let us first recall that the basic approximations commonly made to address the impurity–^{4}He$_N$ complex are the Born-Oppenheimer (BO) approximation to factorize the electronic and nuclear wavefunctions, and the Franck-Condon (FC) approximation which assumes that the atomic nuclei do not change their positions or momenta during the electronic transition.[25] In addition, the use of Density Functional Theory (DFT) to describe the droplet-impurity complex allows factorizing the impurity and He nuclear components.[26,27]

Time-dependent density-functional theory has lend itself as a convenient tool to address the dynamics of helium interacting with confining surfaces[28,29] or atomic impurities in bulk[30–33] and in helium droplets.[4] It provides a fair compromise between accuracy and computational effort. So far it is the only practical method to dynamically address systems of experimental interest consisting of thousands of helium atoms.

A. Statics

As a starting point for the dynamics, we first obtain the structure of the system in its ground state as described *e.g.* in Ref. 26. Throughout this work we have used the Orsay-Trento (OT) density functional[27] neglecting the backflow term. This term has no effect on the statics and its influence on the dynamics will be discussed later.

The BO factorization of the electronic wavefunction allows the interaction between the helium moiety and the impurity to be represented by an effective interaction that is based on the AgHe pair-potential, $V_X^{5s}(r)$.[34] In view of the large mass of Ag, we neglect its zero-point motion and describe it as a classical particle by using an external field.[35] The validity of this approximation is checked *a posteriori*, see below.

From the variation of the resulting energy of the system

$$E[\rho] = \int d\mathbf{r}\,\frac{\hbar^2}{2m_{\rm He}}\left|\nabla\sqrt{\rho(\mathbf{r})}\right|^2 + \mathcal{E}_{\rm He}[\rho(\mathbf{r})] + \int d\mathbf{r}\rho(\mathbf{r})V_X^{5s}(|\mathbf{r}_{\rm Ag}-\mathbf{r}|)\,, \quad (1)$$

where $\mathcal{E}_{\rm He}$ is the OT potential energy density per unit volume[27] and ρ is the helium particle density, one obtains the Euler-Lagrange equation

$$\frac{\delta}{\delta\rho}\left(\frac{\hbar^2}{2m_{\rm He}}\left|\nabla\sqrt{\rho}\right|^2 + \mathcal{E}_{\rm He}\right) + V_X^{5s} = \mu\,, \quad (2)$$

where μ is the chemical potential corresponding to a droplet with a fixed number of He atoms, $\int d\mathbf{r}\rho(\mathbf{r}) = N$. Throughout this paper we have taken $N = 1000$.

Details on how the above equation is solved can be found in Ref. 35. In the present study we have worked in cartesian coordinates using a spatial grid of 0.4 Å and a $200 \times 200 \times 250$ box. The derivatives have been calculated with 13-point formulas. The density profile for the minimal energy configuration is shown in Fig. 3.

To check the validity of the approximation to describe the Ag atom classically, we have estimated the width of the ground state wavefunction of a quantum Ag atom in the mean-field potential

$$V(\mathbf{r}_{\rm Ag}) = \int d\mathbf{r}\rho(\mathbf{r})V_X^{5s}(|\mathbf{r}_{\rm Ag}-\mathbf{r}|). \quad (3)$$

Due to the large mass of Ag, we find a width of the wavefunction of less than 0.1 Å. This value is much smaller than the characteristic length scale of the mean field and V_X^{5s} potentials and of the helium density variations, see Fig. 4, thereby justifying our approach.

It will be useful to start the dynamics not from the equilibrium position of the Ag atom but rather from an arbitrary position on the z axis, $\mathcal{Z}_0$, that corresponds to a radial distance R_0. This can be achieved adding a constraint of the kind

$$\frac{\lambda_C}{2}[\mathcal{Z} - \mathcal{Z}_0]^2 \quad (4)$$

to the expression of the total energy,[36] where $\mathcal{Z}$ is the distance in the z direction between the impurity and the center of mass of the helium moiety, and λ_C is an arbitrary constant large enough to guarantee that, upon minimization of the constrained energy, $\mathcal{Z}$ equals the desired $\mathcal{Z}_0$ value. Typically, a value $\lambda_C \sim 1000$ K Å^{-2} ensures the obtention of $\mathcal{Z}_0$ with a $\lesssim 0.01$ % error.

The top panel of Fig. 4 shows $\Delta E = E(R_0) - E(\infty)$ as function of R_0 for $N = 1000$. It can be seen that the equilibrium position of Ag is at the center of the droplet. To better appreciate the meaning of ΔE as a function of R_0, the density profile of a pure $^4{\rm He}_{1000}$ droplet is also displayed. Taking for the radius of the droplet the expression $R_{1/2} = r_0 N^{1/3}$ with $r_0 = 2.22$ Å,[37] it can be seen from the figure that it requires about 45 K kinetic energy for Ag to reach the droplet surface. The bottom panel of the figure shows the classical turning point of Ag in the droplet, taking for the kinetic energy of the Ag impurity the classical expression $\frac{1}{2}m_{\rm Ag}v_{\rm Ag}^2$, *i.e.* neglecting the hydrodynamic mass of the helium bubble. This approximation is justified by the small bubble radius (about 5 Å, see Fig. 3) and the fact that $m_{\rm Ag} \gg m_{\rm He}$. It can be seen that only impurities having velocities above ~ 70 m/s can reach the surface region of the droplet. Note that this value is well above the Landau velocity and the critical velocity v_c for ring vortex nucleation in liquid He, $v_c \sim 50$ m/s.[38] This figure will be helpful for discussing the translational dynamics presented below.

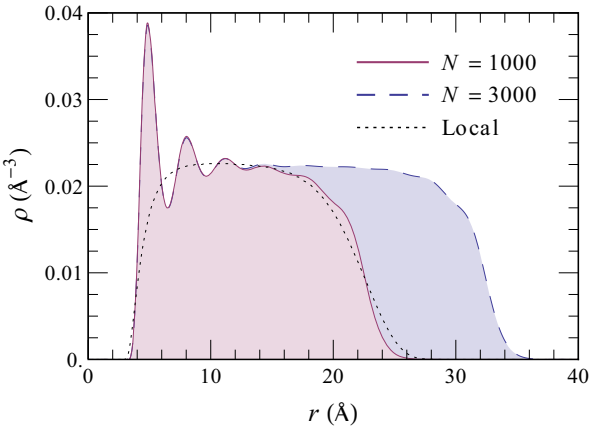

FIG. 3: (Color online) He density profiles of the Ag@$^4{\rm He}_{1000}$ and Ag@$^4{\rm He}_{3000}$ droplets obtained using the OT density functional. Also shown is the result for $N = 1000$ obtained with the local density of Ref. 58.

B. Dipole absorption spectrum

Since the dynamical evolution is initiated by the photoexcitation of the embedded Ag atom, the absorption spectrum of the $5p\,^2{\rm P}_{1/2} \leftarrow 5s\,^2{\rm S}_{1/2}$ (D1) and $5p\,^2{\rm P}_{3/2} \leftarrow 5s\,^2{\rm S}_{1/2}$ (D2) transitions has been calculated for the Ag@$^4{\rm He}_{1000}$ equilibrium configuration shown in Fig. 3. The presence of Ag in the droplet induces marked density oscillations. This, however, is a local effect, as a comparison of the density profiles for $N = 1000$ and 3000 shown in that figure reveals. Hence, for impurities fully solvated in large enough droplets the absorption spectrum is independent of the droplet size and the same as in bulk liquid helium.[8] This is of course not the case for droplets made of a few tens of atoms.[12,13]

The $^2\Sigma^+$ and $^2\Pi$ excited state Ag-He pair potentials required for the calculation of the spectra have been taken from Ref. 13, while the V_X^{5s} ground state potential, which

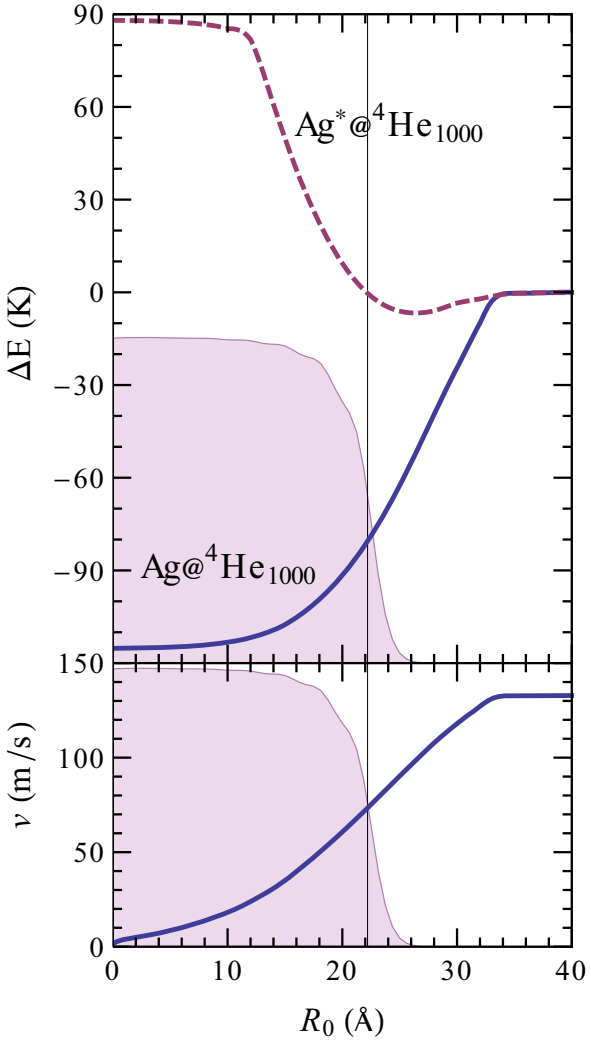

FIG. 4: (Color online) Top panel: Energy of the Ag@^{4}He$_{1000}$ complex for Ag in the ^{2}S$_{1/2}$ ground state (solid line) and the ^{2}P$_{1/2}$ excited state (dashed line) as a function of the distance of the impurity to the center of mass of the He moiety. The energy is measured with respect to the free Ag atom and helium droplet. Bottom panel: translational velocity of Ag for the ΔE values displayed in the solid line of top panel. In both panels the density profile of ^{4}He$_{1000}$ is represented in grey and the thin vertical line indicates the sharp density surface radius.

has also been used to obtain the equilibrium configuration, is taken from Ref. 34. The spin-orbit (SO) interaction has been included as described in Ref. 39. Writing the electron angular momentum in cartesian coordinates $i = x, y, z$ and the spin state as $s = \uparrow$ ($m_s = 1/2$), $\downarrow$ ($m_s = -1/2$), the spin-orbit operator V_{SO} has components

$$V_{SO}^{ijss'} = -\imath \frac{A_{ls}}{2} \sum_k \varepsilon^{ijk} \sigma_k^{ss'}$$

where ε^{ijk} is the Levi-Civita symbol, σ_k is the Pauli matrices and A_{ls} is 2/3 the SO splitting in the free atom. Shape fluctuations of the helium bubble have been explicitly taken into account using the atomic-like DFT sampling technique as described in Ref. 40. Since these methods are both well established, we do not consider it necessary to repeat their details here.

Figure 1 shows the calculated excitation spectrum. To account for the fact that in the experiment the transition to the the ^{2}P$_{3/2}$ state is detected with a reduced efficiency, as discussed in Sec. II B, we have renormalized the intensity of the calculated $5p\,^2$P$_{3/2} \leftarrow 5s\,^2$S$_{1/2}$ transition by the experimentally determined correction factor. It can be seen that the agreement between theory and experiment[10] is excellent. This should be contrasted to previous Monte Carlo (MC) calculations that yielded an appreciable overlap of the two absorption bands.[11,12] More recent MC calculations[13] employing the same He-Ag pair potentials as used in this work also yield clearly separated bands, albeit for much smaller droplets.[13,34] Hence, the agreement between the theory and experiment can be attributed to the high quality of the He-Ag pair potentials together with a correct description of the Ag@^{4}He$_N$ complex by the non-local density functional approach (see the Appendix).

C. Dynamics

Once a static configuration has been determined from DFT as discussed before, it may constitute a starting configuration for the dynamical evolution of the system upon photoexcitation of the Ag atom. To evolve the system, we proceed as follows.

- A complex effective wavefunction representing the He moiety is evolved following a TDDFT prescription.
- The displacement of the Ag atom is treated classically.
- The dynamical evolution of the electronic excited state within the ^{2}P manifold of the silver atom is taken into account by introducing an additional degree of freedom, $|\lambda\rangle$. Using the basis for angular momentum and spin previously described, the electronic state of Ag can be written as

$$|\lambda\rangle = \sum_{is} \lambda_{is} |i, s\rangle$$

with $|\langle\lambda\,|\lambda\rangle|^2 = 1$.

The complete set of dynamical variables characterizing the system thus consists of a complex effective wavefunction for helium $\Psi_{\rm He}(t,\mathbf{r})$ such that $\rho(t,\mathbf{r})=|\Psi_{\rm He}(t,\mathbf{r})|^2$, a vector position for the impurity, $\mathbf{r}_{\rm Ag}(t)$, and a 6-dimensional complex vector for its electronic state $|\lambda(t)\rangle$. The total energy of the Ag@^{4}He$_{1000}$ complex suddenly excited to the ^{2}P manifold is thus written as

$$\begin{aligned} E[\Psi,\mathbf{r}_{\rm Ag},\lambda] &= \int d\mathbf{r}\,\frac{\hbar^2}{2m_{\rm He}}|\nabla\Psi|^2+\frac{p_{\rm Ag}^2}{2m_{\rm Ag}} \\ &+ \int d\mathbf{r}\,\mathcal{E}_{\rm He}[\rho]+\langle\lambda|V_{SO}|\lambda\rangle \\ &+ \int d\mathbf{r}\rho(\mathbf{r})V_\lambda(\mathbf{r}-\mathbf{r}_{\rm Ag})\,. \end{aligned} \tag{5}$$

We have followed the prescription of Ref. 39 to write the pair potential as a direction-dependent combination of Π and Σ potentials

$$V_\lambda(\mathbf{r})=\langle\lambda|\mathcal{V}(\mathbf{r})|\lambda\rangle=\sum_{ijss'}\lambda_{is}^*\mathcal{V}^{ijss'}(\mathbf{r})\lambda_{js'} \quad , \tag{6}$$

where the six-dimensional matrix operator $\mathcal{V}$ has components

$$\mathcal{V}^{ijss'}(\mathbf{r})=\left[V_\Pi(r)\delta_{ij}+(V_\Sigma(r)-V_\Pi(r))\frac{r_ir_j}{r^2}\right]\delta_{ss'}\,. \tag{7}$$

To obtain the dynamical evolution, the coupled 3D time-dependent system resulting from the variation of the action

$$\begin{aligned} \mathcal{A}[\Psi_{\rm He},\mathbf{r}_{\rm Ag},\lambda] &= \int dt\,\{E[\Psi_{\rm He},\mathbf{r}_{\rm Ag},\lambda] \\ &- i\hbar\int d\mathbf{r}\,\Psi_{\rm He}^*(\mathbf{r})\frac{\partial}{\partial t}\Psi_{\rm He}(\mathbf{r}) \\ &- i\hbar\,\langle\lambda|\frac{\partial}{\partial t}|\lambda\rangle-\frac{1}{2}m_{\rm Ag}\dot{\mathbf{r}}_{\rm Ag}^2\Big\} \end{aligned} \tag{8}$$

has to be solved. This yields

$$\begin{aligned} i\hbar\frac{\partial}{\partial t}\Psi_{\rm He} &= \left[-\frac{\hbar^2}{2m_{\rm He}}\nabla^2+\frac{\delta\mathcal{E}_{\rm He}}{\delta\rho(\mathbf{r})}+V_\lambda(\mathbf{r}-\mathbf{r}_{\rm Ag})\right]\Psi_{\rm He} \\ i\hbar\frac{\partial}{\partial t}|\lambda\rangle &= \left[\int d\mathbf{r}\rho(\mathbf{r})\mathcal{V}(\mathbf{r}-\mathbf{r}_{\rm Ag})+V_{SO}\right]|\lambda\rangle \\ m_{\rm Ag}\ddot{\mathbf{r}}_{\rm Ag} &= -\nabla_{\mathbf{r}_{\rm Ag}}\left[\int d\mathbf{r}\rho(\mathbf{r})V_\lambda(\mathbf{r}-\mathbf{r}_{\rm Ag})\right] \end{aligned} \tag{9}$$

where the t-dependence of the dynamical variables is omitted for clarity. Notice that the equation for $|\lambda\rangle$ is a matrix equation.

To solve the above equations initial values for the variables are required. This bears some arbitrariness. We have followed a strategy based on physical plausibility and numerical expeditiousness. We have chosen a set of helium density $\rho_0(\mathbf{r})$ –or effective wavefunction $\Psi_0(\mathbf{r})$– and silver position $\mathbf{r}_{\rm Ag_0}$ determined from a static calculation carried out as indicated before, and we choose the initial velocity of the impurity to be zero. Thus, we start from the mimimum energy configuration for a given displacement R_0 or, in other words, from any point on the curve displayed in the top panel of Fig. 4 as if it was the classical turning point of the Ag atom in the ^{4}He$_{1000}$ droplet. It should be noted that although the silver atom spends considerable time at the classical turning points, these initial conditions are just a subset of those encountered in the experiment.

At any of these positions, the silver atom is photoexcited to the ^{2}P manifold and the remaining variable λ is chosen among one of the eigenstates resulting from the diagonalization of its Hamiltonian at $t=0$

$$H^{ijss'}=\int d\mathbf{r}\,\rho_0(\mathbf{r})\mathcal{V}^{ijss'}(\mathbf{r}-\mathbf{r}_{\rm Ag_0})+V_{SO}^{ijss'}\,. \tag{10}$$

If the helium density is spherically symmetric around the dopant atom, the first term in the matrix above is proportional to the identity and as a result of the diagonalization one obtains the usual $J=1/2$ and $J=3/2$ eigenvectors pertaining to the spin-orbit interaction. This occurs in liquid helium or when the impurity sits at the geometric center of a helium droplet. When the dopant is displaced off center, its environment is only axially symmetric. In this case, the potential matrix still has two of the V_{SO} eigenstates corresponding to $J=3/2$ as eigenvectors. However, the other four eigenstates are no longer eigenvectors of V_{SO} but a mixture of them. For the helium distributions considered here, this effect turns out to be a small perturbation and the mixed eigenvectors are such that they still have $\langle J\rangle\simeq 1/2$ and $\langle J\rangle\simeq 3/2$. This allows us to label the electronic states that we take as initial condition for the dynamics as $|\lambda\rangle=|{}^3\!/_2\rangle$ for the pure $J=3/2$ state, and $|\lambda\rangle=|\widetilde{{}^1\!/_2}\rangle$ and $|\lambda\rangle=|\widetilde{{}^3\!/_2}\rangle$ for the mixed states. Following a more conventional notation, the $|\widetilde{{}^1\!/_2}\rangle$ configuration will be referred to as $^2\mathrm{P}_{1/2}$ (D1), while the other two electronic states $|{}^3\!/_2\rangle$ and $|\widetilde{{}^3\!/_2}\rangle$ will be referred to as the $^2\mathrm{P}_{3/2}$ (D2) configuration.

The three potentials $V_{\widetilde{1/2}}$, $V_{\widetilde{3/2}}$ and $V_{3/2}$ obtained from these eigenvectors are shown in Fig. 5 for the ρ_0 density corresponding to $R_0=22.2$ Å. Because the Σ potential is purely repulsive and the Π potential has a deep attractive well, the resulting V_λ, see Eq. (7), have quite different shapes. $V_{\widetilde{1/2}}$ is spherically symmetric and largely repulsive, with a shallow minimum of less than 1 K at 7.2 Å. $V_{\widetilde{3/2}}$ is also largely repulsive with a shallow annular minimum of about 2 K. Note that this potential is not spherically symmetric. In contrast to these potentials, $V_{3/2}$ reveals two deep wells with depths of about 400 K that are localized along the symmetry axis of the complex. For all densities computed in this work we have found a similar phenomenology.

We finally mention that Eqs. (9) have been solved within the same box and using the same grid as for the static problem. The time step employed is 0.5 fs and the dynamics has been followed for up to 200 ps when needed. We have used a predictor-corrector method[41] fed by a few time steps obtained by a fourth-order Runge-Kutta algorithm. When needed, we have included an absorbing potential[33] to prevent some He density to bounce back when it reaches the box boundary. In these cases, the number of evaporated He atoms that leave the calculation box has been found to be rather small, ten atoms at most.

IV. NUMERICAL RESULTS

A. Ag ^{2}P$_{1/2}$ dynamics

We first discuss the dynamical evolution of the system following excitation of the silver atom to the ^{2}P$_{1/2}$ state. Figs. 6 and 7 show snapshots in 8 ps intervals of the helium density and Ag position as the system evolves. These results have been obtained by initially placing the silver atom at rest at a distance of $R_0 = 18$ and 22.2 Å, respectively.[42] The phase portrait of the motion of Ag following its dipole excitation to the ^{2}P$_{1/2}$ state is shown in Fig. 8 for several values of R_0. This figure is quite useful to understand and interpret the results we have obtained, relating them at least qualitatively to the experimental findings. It can be seen from the phase space trajectories displayed in Fig. 8 that Ag atoms photoexcited at a radial position $R_0 = 18$ Å and smaller are ejected from the droplet. One such evolution is shown in Fig. 6, and several others are shown in the supplementary material.[42] In contrast, Ag atoms photoexcited at $R_0 = 22.2$ Å and larger are not ejected, as shown in Fig. 7.

To gain more insight into the position dependence of the dynamics, the energy of Ag(^{2}P$_{1/2}$)@He$_{1000}$ has been calculated as a function of the distance of the Ag with respect to the center of mass of the helium moiety, analogous to what has been done for the ground state. The resulting energy curve, which can be considered as a first estimate of the effective interaction potential for the translational motion of the excited ^{2}P$_{1/2}$ Ag, $V_{1/2} = 2V_\Pi/3 + V_\Sigma/3$, is displayed in the upper panel Fig. 4. The curve helps to understand most of the results found in the dynamical calculations. First notice that due to the symmetry of the system excitation of Ag at rest at the center of the droplet will not cause a displacement of the impurity. As the potential is rather flat at small displacements from the center, the final velocities are largely insensitive to the exact initial position of the excited silver atom. In contrast, the potential changes strongly in the surface region and the final velocities vary significantly with position at the surface. Inspection of the ^{2}P$_{1/2}$ potential in Fig. 4 reveals a clear minimum at $R_0 = 26$ Å. As a result of this minimum, the excited Ag will get trapped at the surface if its kinetic energy

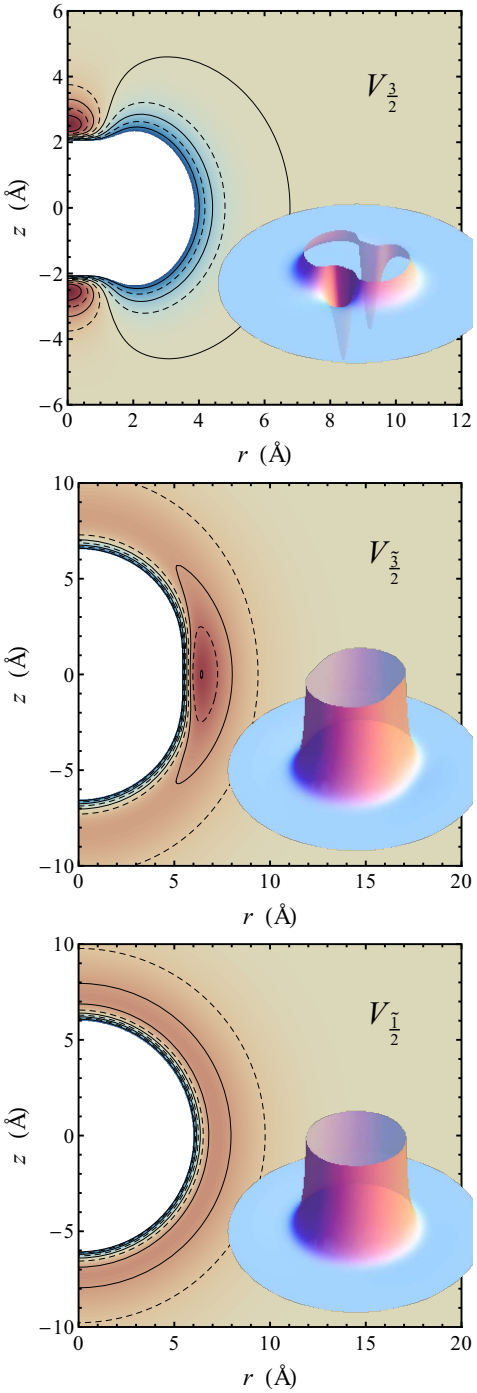

FIG. 5: (Color online) Top panel: Ag-He potential for the $J = 3/2$ state. Middle panel: Same for the $\langle J\rangle \simeq 3/2$ state. Bottom panel: Same for the $\langle J\rangle \simeq 1/2$ state. Nine contour lines are drawn in solid-dashed alternation dividing the energy display range in each panel, which is from −400 K to 400 K for the top one and from −2 K to 2 K for the rest.

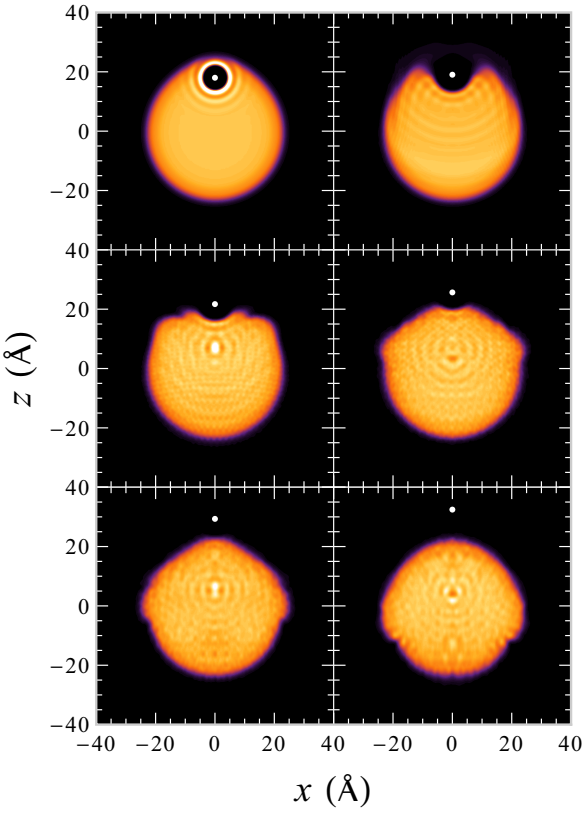

FIG. 6: (Color online) Starting from the top left frame, dynamic evolution of the Ag@^{4}He$_{1000}$ complex when the Ag atom initially at rest 18 Å off center of the droplet is suddenly excited to the ^{2}P$_{1/2}$ state. The time between frames is 8 ps.

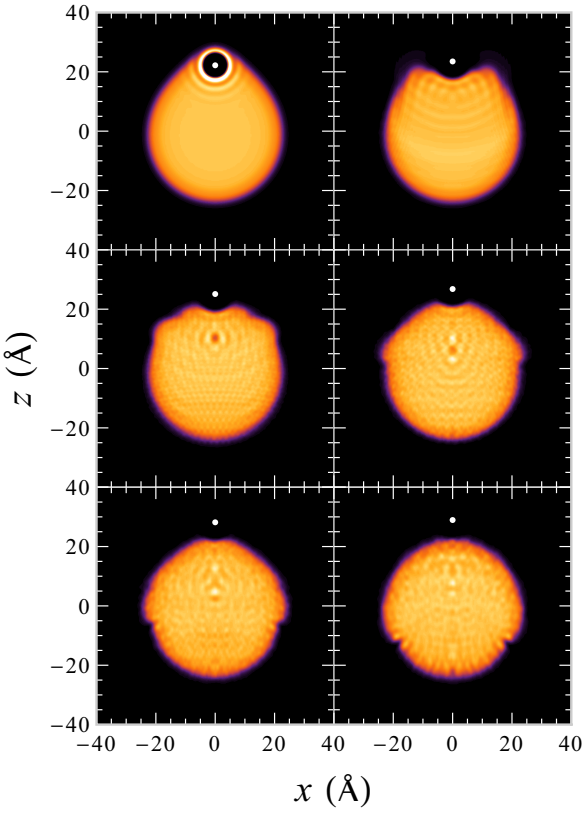

FIG. 7: (Color online) Starting from the top left frame, dynamic evolution of the Ag@^{4}He$_{1000}$ complex when the Ag atom initially at rest 22 Å off center of the droplet is suddenly excited to the ^{2}P$_{1/2}$ state. The time between frames is 8 ps.

is smaller than the well depth of ~ 6 K. Indeed, the dynamical evolution shown in Fig. 7 and the corresponding phase space trajectory shown in Fig. 8 reveal that Ag atoms photoexcited at $R_0 = 22.2$ Å are not ejected from the droplet.

This last theoretical result at first appears to contradict the experimental findings that following excitation of the ^{2}P$_{1/2}$ state nearly all of the Ag atoms are ejected. The bottom panel of Fig. 4 helps to reconcile this apparent disagreement. Since He droplets are expected to be superfluid at the experimental temperature of 0.4 K,[43,44] configurations that start at, *e.g.,* 22.2 and 25 Å are nonphysical, as the velocity of Ag in the droplet that would permit the impurity to arrive at these classical turning points is above the Landau critical velocity. Hence, before getting to these positions the motion of Ag would likely cause roton creation or ring vortex nucleation, thereby slowing down the silver atom.[45,46]

Closer inspection of Fig. 8 reveals some straggling of the phase space trajectories. The effect is most marked for small Ag velocities, *i.e.*, in the first stages of its displacement. This is best seen in calculations starting from $R_0 = 1$ Å.[42] In this case, it takes the silver atom some 150 ps to travel up to about 10 Å, and a very marked straggling is observed. During this phase of the evolution the spherical helium bubble is also found to "breath", displaying distinct monopole oscillations with a period of about 20 ps, which corresponds to an energy of 2.3 K. At the same time strong density oscillations can be observed just above the geometrical center of the droplet, see also Fig. 6. It is at this point where the density waves launched by the excitation of the Ag atom are roughly focused after being reflected from the droplet surface. We have not tried to characterize the properties of these waves, as they have already been discussed in Ref. 4. The complex interference pattern produced by these density waves persist for quite long times[47] during which the droplet has a clear tendency to recover its spherical symmetry. We attribute the observed straggling in the motion of the excited Ag to its interaction with these interfering density waves. Inspection of Figure 8 further reveals that the final velocity for Ag excited in the bulk

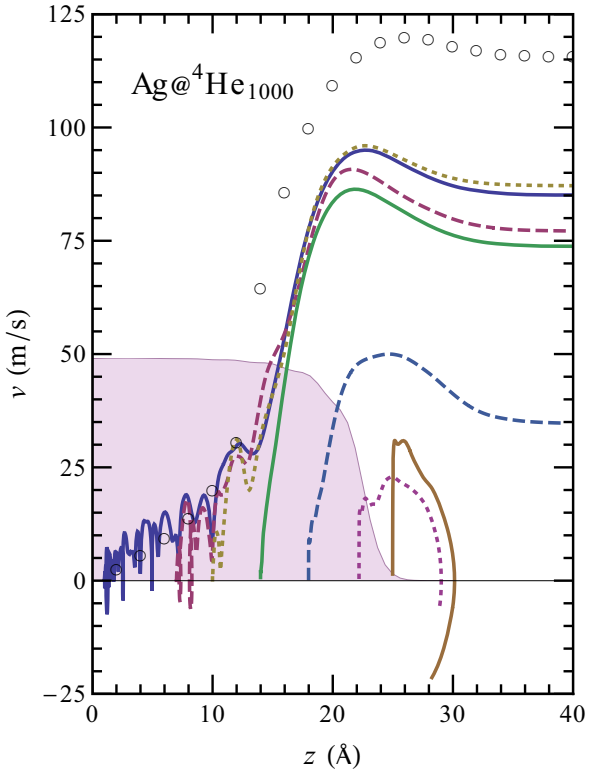

FIG. 8: (Color online) Phase portrait of the motion of Ag in a ^{4}He$_{1000}$ droplet after its dipole excitation to the ^{2}P$_{1/2}$ state at the classical turning point. Results for R_0 = 1, 10, 14, 18, 22, and 25 Å are shown. The empty circles follow the Ag trajectory as a free particle moving in the ^{2}P$_{1/2}$ potential shown in Fig. 4.

of the droplets exhibits a small and unsystematic variation of a few m/s as function of the initial position. Since the interaction potential is a smooth function, see Fig. 4, we attribute this variation to the strangling motion of the Ag in the initial phase of the trajectory and the non-adiabatic energy transfer between the impurity and the surrounding helium.

The most interesting feature of Fig. 8 is the appearance of a limiting velocity for Ag of about 87 m/s, which matches closely the range of velocities detected in the experiment, see Fig. 2. It is instructive to compare this value with the final speed calculated from the interaction potential assuming that the silver atom experiences no drag during its motion through the superfluid helium. This is equivalent to describing the motion of Ag as that of a free particle. Assuming a hydrodynamic mass of 107 amu, one finds a final speed of 116 m/s, a value significantly higher than that found both by the dynamical calculations and the experiments. One could argue that this difference is due to the hydrodynamic mass used. In order to bring the two results into agreement a hydrodynamic mass of 192 amu would be required, a value judged too large for Ag in a bubble of only 5 Å radius. Insight into the origin of the different final speeds can be obtained from the phase space trajectories. The trajectory for R_0 = 1 Å calculated for a free particle using the interaction potential shown in Fig. 8 matches very well that of the dynamical calculations for low speeds, except for the straggling discussed above. This indicates that the Ag during the first part of the evolution experiences no drag and that the helium droplets are indeed superfluid. It is at higher speeds that a deviation between the two results is observed. This raises the question whether this difference is related to the existance of a critical velocity. The limiting speed of 87 m/s in the dynamical calculations is noticeably larger than the experimental Landau velocity of $\sim$ 60 m/s. However, it is close to the Landau velocity of v_L = 94 m/s calculated from the OT density functional neglecting the term that mimics backflow effects.[48] We recall that the complete OT functional has been adjusted to reproduce the experimental value of v_L but that in the present work we have not considered the backflow term term as its evaluation requires unaffordable small time-steps. In spite of the excellent agreement between the expected and calculated maximum velocity, it is not evident to attribute the limiting velocity to the existence of a critical Landau velocity in the droplets because before achieving this velocity the bubble bursts open and the interaction potential becomes attractive. Nonetheless, the above results clearly demonstrate that dynamical calculations are essential to correctly determine the velocity of the ejected Ag.

These theoretical results and conclusions are expected to be largely independent of the helium droplet size. The rationale for this claim is the "universality" of the Ag@^{4}He$_N$ energies as function of the distance from the droplet surface, $R_0 - R_{1/2}$. This universality has been found to be nearly perfect for very weakly interacting impurities like Mg.[36] For the stronger interacting Ag investigated in the present study, we have also found that the difference in the ^{2}S$_{1/2}$ and ^{2}P$_{1/2}$ energy curves for N = 1000 and 3000 is very small, *i.e.* less than 6 K, at the surface region. Consequently, the classical turning points of ground silver measured with respect to the droplet surface, $R_{1/2}$, will be largely independent of droplet size and therefore also the dynamical evolution of the system after excitation to the ^{2}P$_{1/2}$ state.

B. Ag ^{2}P$_{3/2}$ dynamics

The most characteristic experimental findings for excitation to the ^{2}P$_{3/2}$ state are the efficient relaxation of the system to the lower spin-orbit state, the detection of AgHe and AgHe$_2$ exciplexes and the significant fraction of excited silver atoms that remain solvated.[10] The formation of AgHe$_2$ exciplexes had already been observed before in bulk He and dense helium gas.[5,49] These studies indicate that that the ^{2}D$_{5/2}$ state, which lies between the ^{2}P$_{3/2}$ and ^{2}P$_{1/2}$ states, plays an important role in

the complex formation and the decay of the $^2P_{3/2}$ state. Like in previous work that used a quantum molecular dynamics approach[11], the $^2D_{5/2}$ state is not included in the present theoretical treatment. Hence, it is unclear to what extend the calculations can correctly describe the relaxation dynamics of the $^2P_{3/2}$ excited state. In addition, it is *a priori* not obvious that the present TDDF calculations can correctly describe exciplexes formation, as the OT functional was not devised for addressing configurations requiring an atomic-like description for a part of the system. Inhomogeneous configurations as these may be addressed by adding extra terms to the functional which, however, come at a significant computational cost.[53,54] Having these shortcomings in mind, we present next some exploratory calculations pushing the present formalism to its very limit and leaving a more realistic description of exciplexes formation within TDDF theory to a forthcoming study.

We start our discussion by considering the mixed $^2P_{3/2}$ configuration. As the $V_{\widetilde{3/2}}$ potential is very similar to the $V_{\widetilde{1/2}}$ potential, see Fig. 5, excitation to the mixed $^2P_{3/2}$ state is expected to yield similar dynamics as found for the $^2P_{1/2}$ state. The most noticeable difference between the two potentials is the slightly more profound ring well for the $V_{\widetilde{3/2}}$ potential. One might therefore expect that excitation to the mixed state leads to the ejection of Ag carrying along some helium atoms, *i.e.* the ejection of AgHe exciplexes. Fig. 9 displays the evolution of Ag@^{4}He$_{1000}$ when Ag, initially at rest at $R_0 = 18$ Å, is suddenly excited to this mixed state.[42] As expected, the Ag is ejected from the helium droplet with a phase space trajectory, and thus also a final velocity, very similar to that of Ag $^2P_{1/2}$ when excited at the same initial position. Closer inspection of Fig. 9 reveals the appearance of a high helium density in the close proximity of the silver atom, which might be interpreted as the dynamical appearance of an AgHe exciplex. It should be noted that the number of He atoms corresponding to the helium density is fractional and smaller than one. In view of the limitations of the current TDDF method, this number should be interpreted with care. Since within TDDF theory He is continuously drawn into the well of the $^2P_{3/2}$ potential, it is not evident to determine the time for exciplex formation. Inspecting Fig. 9 we conclude that it takes about 20 ps.

Excitation of the Ag to the pure $^2P_{3/2}$ state is expected to yield very different results, as the corresponding $V_{3/2}$ potential, shown in the top panel of Fig. 5, is characterized by two deep potential wells. Excitation to this state is expected to give rise to exciplex formation. However, in view of the attractive character of this potentials it is not obvious that these exciplexes will be ejected from the droplets. Fig. 10 shows the dynamical evolution of the system after exciting the silver atom to the pure $^2P_{3/2}$ configuration at a distance of $R_0 = 18$ Å. The results for excitation at $R_0 = 25$ Å can be found in the supporting information.[42] Inspection of the figures reveals the

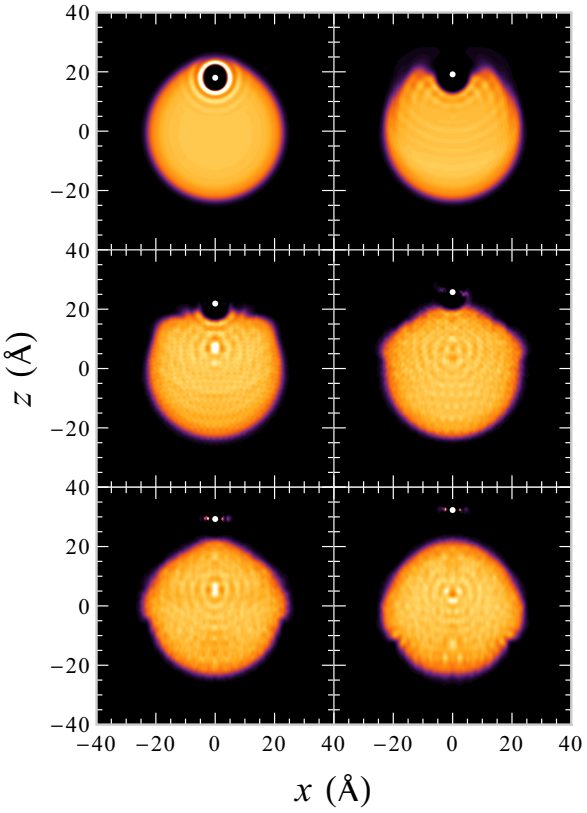

FIG. 9: (Color online) Starting from the top left frame, dynamic evolution of the Ag@^{4}He$_{1000}$ complex when the Ag atom initially at rest 18 Å off center of the droplet is suddenly excited to the mixed $^2P_{3/2}$ state. The time between frames is 8 ps.

formation of a high helium density in the close proximity of the silver atom, which again can be interpreted as the dynamical appearance of an AgHe exciplex. Also in this case the number of He atoms corresponding to the helium density is fractional and smaller than one. It is worth recalling, as Fig. 5 shows, that the exciplex pertaining to the mixed state grows as a ring around the waist of the mixed $^2P_{3/2}$ electronic state whereas the exciplex pertaining the pure $^2P_{3/2}$ electronic state discussed here consists of two localized He density spots. The time scale for the exciplex formation is estimated to be less than 4 ps, which is significantly faster than found for the mixed $^2P_{3/2}$ state. The fast exciplex formation can be attributed to the depth of the wells for the $V_{3/2}$ potential. The calculations furthermore reveal that in neither of the two examples discussed here the exciplex is ejected from the droplets. This could be expected for the $R_0 = 25$ Å case, but is at variance with the observed ejection for the $^2P_{1/2}$ and mixed $^2P_{3/2}$ configurations at $R_0 = 18$ Å, see Figs. 6 and 9. Analysis of the excited state evolution reveals that the systems remains a pure $^2P_{3/2}$ configura-

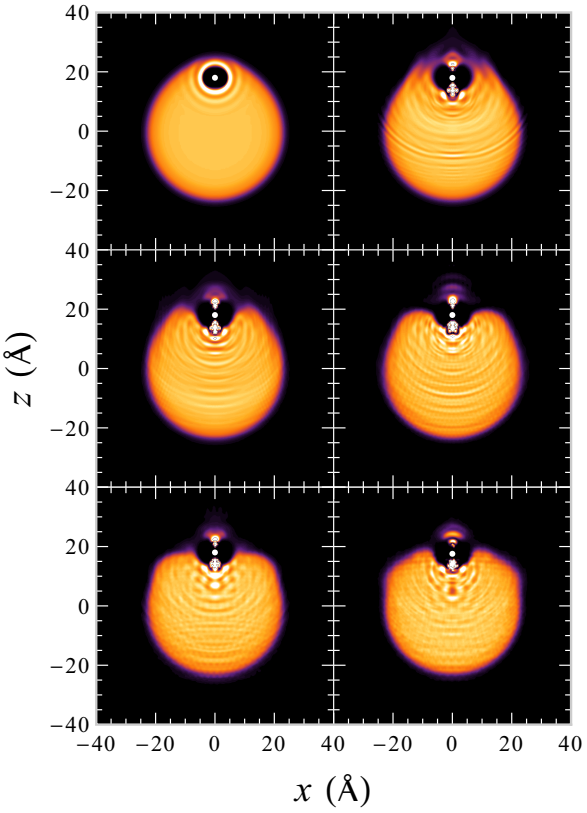

FIG. 10: (Color online) Starting from the top left frame, dynamic evolution of the Ag@^{4}He$_{1000}$ complex when the Ag atom initially at rest 18 Å off center of the droplet is suddenly excited to the pure ^{2}P$_{3/2}$ state. The time between frames is 4 ps.

tion at all times. As this configuration is characterized by a strong attractive interaction with the helium, the silver atom is not expected to leave the droplet.

Summarizing we find that the Ag atom is ejected from the droplets with a small quantity of ^{4}He –less than one atom– attached when excited to the $|\widetilde{^3/_2}\rangle$ but remains solvated when excited to the $|^3/_2\rangle$ state. Overall, these results compare well with experiment where it was found that 42% of the ^{2}P$_{3/2}$ excited Ag atoms remain solvated and a significant fraction is ejected as AgHe exciplexes. Whereas the calculations indicate that the ejected species are ^{2}P$_{3/2}$ excited, experiment reveals that most of them have relaxed to the ^{2}P$_{1/2}$ state. This discrepancy might be attributed to the absence of the ^{2}D$_{5/2}$ state in the calculations. Its inclusion would introduce an additional decay channel that could result in efficient relaxation before ejection from the droplets.

Photoelectron and ZEKE spectra revealed that a large fraction of the excited Ag atoms remains solvated in the droplets.[10] The experiments did not provide conclusive evidence on the state distribution of the solvated atoms

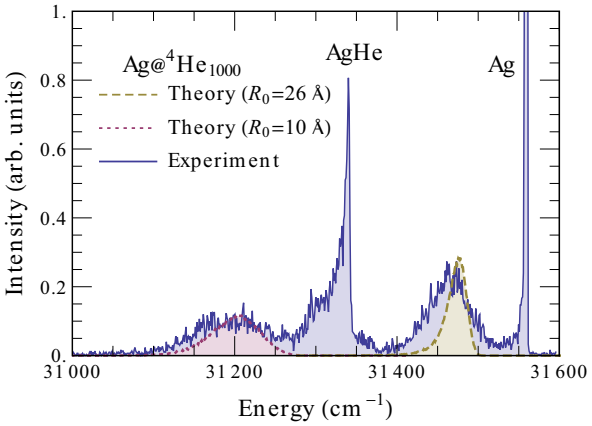

FIG. 11: (Color online) Experimental ZEKE spectrum of Ag recorded following excitation via the D2 transition of Ag atoms in helium droplets consisting on average of 2750 atoms and the theoretical ZEKE spectrum for Ag(^{2}P$_{1/2}$)@He$_{1000}$ calculated with the helium density profile corresponding to the energy minimum at $R_0 = 26$ Å and at $R_0 = 10$ Å.

nor did they allow to determine whether these atoms are located on the surface or in the bulk of the droplets. The present calculations on the Ag ^{2}P$_{1/2}$ energy as function of position, see Fig. 4, reveal that the minimum energy configuration for this state corresponds to a Ag atom located in a dimple on the surface of the droplet at about a distance $R_0 \sim 26$ Å. Using this configuration we have computed the corresponding ZEKE spectrum by substituting the He-Ag V$_{1/2}$ potential by the He-Ag$^+$ ground state potential[10,50] and then proceeding as in the calculation of the dipole absorption spectrum.[39] This approach fully takes into account the three-dimensional character of the problem and shape fluctuations of the helium bubble around the impurity.[40] A comparison of the calculated and experimental ZEKE spectrum is presented in Fig. 11. The agreement between the spectra is excellent, which indicates that there are indeed ^{2}P$_{1/2}$ Ag atoms located on the surface of the droplets. Only the experimental width turns out to be slightly larger than the theoretical prediction, even though density fluctuations –the main mechanism underlying the width of the line[40]– are included. The broad feature in the experimental ZEKE spectrum at about 31200 cm^{-1} has tentatively been assigned to Ag ^{2}P$_{3/2}$.[10] Unfortunately, it is not possible to accurately calculate ZEKE spectra for the ^{2}P$_{3/2}$ state. As mentioned before, the OT functional used in the present calculations is not well adapted to describe configurations requiring an atomistic description, like that resulting from the interaction of ^{2}P$_{3/2}$ with the helium. In spite of this, we have used some of the dynamic configurations shown in Fig. 10 to estimate the ZEKE transition for Ag ^{2}P$_{3/2}$. In this way we find a transition frequency of about 30300 cm^{-1}, *i.e.*, 1200 cm^{-1} to the red of the ^{2}P$_{1/2}$ transition. Although only an estimate, this

result clearly rules out that experimental feature at 31200 cm^{-1} originates from Ag $^2P_{3/2}$. Photoionization studies on doped helium droplets have found that the ionization threshold generally is several 100 cm^{-1} lower in energy for solvated species than for those located at the surface of helium droplets.[51,52] Hence, it is very likely that the 31200 cm^{-1} feature corresponds to solvated Ag $^2P_{1/2}$. This suggestion is confirmed by calculations where Ag is located at $R_0 = 10$ Å, *i.e.*, in the bulk of the droplet. As can be seen in Fig. 11, the agreement between the calculated and experimentally observed ZEKE transition is excellent. This assignment implies that the $^2P_{3/2}$ excited Ag atoms relax very efficiently to the $^2P_{1/2}$ state. The fact that the dynamical calculations do not reveal such a relaxation process can be attributed to the simplification not to include the $^2D_{5/2}$ state in the simulations. This assignment raises the question as why Ag $^2P_{1/2}$ is observed in the bulk of the droplets even though the interaction of Ag $^2P_{1/2}$ with helium is repulsive, see Fig. 5. One possible explanation would be that the ionization rate is sufficiently high that the Ag atoms are ionized before they have been ejected from the droplets. This would also explain why the fraction of solvated Ag $^2P_{1/2}$ was found to increase with droplet radius.[10]

V. SUMMARY AND OUTLOOK

We have carried out a combined experimental and theoretical investigation of the translational dynamics of Ag atoms in helium droplets photoexcited to the ^2P manifold. An analysis of the experimental results has been carried out within a full dynamical, three dimensional approach that combines a time-dependent DFT description of the droplet with a classical dynamics description of the impurity. Our theoretical approach has a broad applicability. In particular, it is well suited to describe the solvation and desolvation of Ba^+ cations in helium droplets.[21]

The experiments have revealed that the $5p\,^2P_{1/2} \leftarrow 5s\,^2S_{1/2}$ (D1) and $5p\,^2P_{3/2} \leftarrow 5s\,^2S_{1/2}$ (D2) transitions are significantly blue-shifted with respect to the corresponding gas phase transitions, and that they do not overlap. These observations are quantitatively reproduced by the static calculations, which allows us to have confidence in the theoretical model.

In qualitative agreement with experiment, the dynamical calculations reveal the existence of a limiting velocity for silver atoms ejected from the droplets following excitation to the $^2P_{1/2}$ state. The calculations furthermore reveal that at low velocities the Ag does not experience any drag by the surrounding helium, which can be taken as evidence of superfluidity of the helium droplets. At higher velocities, a clear deviation from this behavior is observed. The limiting velocity attained by the silver atom is close to the Landau velocity associated with the used OT density functional. However, we cannot conclusively attribute the limiting velocity to the critical Landau velocity because, by the time the Ag atom has accelerated enough to potentially excite rotons or nucleate vortices in the liquid, the bubble has already burst open. Nonetheless, we would like to stress that the employed method makes use of a dynamical framework that allows for roton excitation and ring vortex nucleation, albeit at velocities about 50 % larger than found experimentally. The observed maximum speed could therefore well be related to the critical velocity associated with these processes. In this respect it is worth noting that ring vortex nucleation by neutral impurities or cations moving in liquid helium has never been addressed by realistic methods. The huge structural changes neutral impurities induce in the surrounding liquid at small length scales will render the development of any vorticity around a neutral impurity very difficult. Hence, before considering the possibility of ring vortex nucleation as a dissipation mechanism of the translational energy of impurities in droplets, a realistic attempt to generate them in liquid helium is called for.

The calculations indicate that excitation of Ag via the D2 transition leads to exciplexes formation. Those excited to the mixed $|\widetilde{^3/_2}\rangle$ state are found to be ejected from the droplets, whereas those excited to the pure $|^3/_2\rangle$ state remain solvated. Although these results qualitatively agree with the experimental findings, experimentally a strong relaxation to the $^2P_{1/2}$ state is observed. This discrepancy likely comes from the absence of the $^2D_{5/2}$ state in the calculations. Although evidence for exciplex formation is found in the calculations, an accurate description of the dynamical exciplex formation is still a challenge. Within TDDFT, a possible way to achieve this is to use a test particle description of the helium droplet, generalizing the approach of Ref. 4. Alternatively, one might use the solid-like density functional approach of Refs. 53,54 that allows to describe localized bunches of He atoms while the rest of the cluster is still delocalized.

Acknowledgments

We would like to thank Fausto Cargnoni and Massimo Mella for supplying us with the Ag-He pair potentials, and Francesco Ancilotto for useful discussions. This work has been performed under Grants No. FIS2011-28617-C02-01 from DGI, Spain (FEDER), 2009SGR1289 from Generalitat de Catalunya, and 200020-129623 from the Swiss National Science Foundation. AH has been supported by the ANR (France), Grant No. ANR-08-BLAN-0146-01. DM has been supported by the ME (Spain) FPU program, Grant No. AP2008-04343.

Appendix

It is interesting to see the effect on the spectrum of the solvation structure surrounding the impurity, which is always overlooked within the standard bubble model

approach, see *e.g.* Refs. 55–57 and Refs. therein. To this end, we have repeated the calculation of the ground state of Ag@^{4}He$_{1000}$ using the original local density functional of Stringari and Treiner.[58] This functional includes a $(\nabla\rho)^2$ term whose intensity was adjusted to reproduce the surface tension of the liquid free surface; it also reproduces the equation of state of liquid ^{4}He at zero temperature. Solving for this functional the corresponding Euler-Lagrange equation constitutes a more elaborate way of determining the structure of the liquid around the solvated impurity than the standard bubble model, which also implies an energy minimization but uses instead a simple trial function as density profile.

Figure 3 shows that the local functional yields a helium bubble around the Ag impurity with a radius similar to that of the Orsay-Trento functional, but fails to describe the oscillations of the helium density profile, even underestimating their average. One thus would expect that it yields a less blueshifted absorption spectrum, and this is what Fig. 1 shows. Since the Ag-He pair potentials are the same in both OT and local density functional calculations, one should conclude that the standard bubble model cannot quantitatively account for the atomic shifts in the absorption spectrum of the impurity, in spite of being conceptually and qualitatively correct. The case of electrons in liquid He is an interesting exception in this respect. As the e-He interaction is very repulsive, the electron bubbles are large and they hardly display any shell structure. Consequently, the description of the absorption spectrum of electron bubbles by the standard bubble model yields similar results, yet worse than density functional calculations.[59]

[1] O. Birer, P. Moreschini, and K. K. Lehmann, Phys. Chem. Chem. Phys. **10**, 1648 (2008).
[2] N. Portner, J. P. Toennies, A. F. Vilesov, and F. Stienkemeier, Mol. Phys. **110**, 1767 (2012).
[3] D. Pentlehner and A. Slenczka, Mol. Phys. **110**, 1933 (2012).
[4] A. Hernando, M. Barranco, M. Pi, E. Loginov, M. Langlet, and M. Drabbels, Phys. Chem. Chem. Phys. **14**, 3996 (2012)
[5] J. L. Persson, Q. Hui, Z. J. Jakubek, M. Nakamura, and M. Takami, Phys. Rev. Lett. **76**, 1501 (1996).
[6] Q. Hui, J. L. Persson, J. H. M. Beijersbergen, and M. Takami, Z. Phys. B: Condens. Matter 98, 353 (1995).
[7] Z. J. Jakubek and M. Takami, Chem. Phys. Lett. **265**, 653 (1997).
[8] A. Bartelt, J. D. Close, F. Federmann, N. Quaas, and J. P. Toennies, Phys. Rev. Lett. **77**, 3525 (1996).
[9] F. Federmann, K. Hoffmann, N. Quaas, and J. D. Close, Phys. Rev. Lett. **83**, 2548 (1999).
[10] E. Loginov and M. Drabbels, J. Phys. Chem. A **111**, 7504 (2007).
[11] A. Wada, T. Takayanagi, and M. Shiga, J. Chem. Phys. **119**, 5478 (2003).
[12] M. Mella, M. C. Colombo, and G. Morosi, J. Chem. Phys. **117**, 9695 (2002).
[13] F. Cargnoni and M. Mella, J. Phys. Chem. A **115**, 7141 (2011).
[14] A. Braun, and M. Drabbels, J. Chem. Phys. **127**, 114303 (2007); *ibid.* **127**, 114304 (2007); *ibid.* **127**, 114305 (2007).
[15] M. Lewerenz, B. Schilling, and J. P. Toennies, Chem. Phys. Lett. **206**, 381 (1993).
[16] E. Loginov, C. Callegari, F. Ancilotto, and M. Drabbels, J. Phys. Chem. A **115**, 6779 (2011).
[17] L. Fechner, B. Gruner, A. Sieg, C. Callegari, F. Ancilotto, F. Stienkemeier, and M. Mudrich, Phys. Chem. Chem. Phys. **14**, 3843 (2012).
[18] E. Loginov and M. Drabbels, J. Chem. Phys. **136**, 154302 (2012).
[19] A. Braun and M. Drabbels, Phys. Rev. Lett. **93**, 253401 (2004).
[20] S. Smolarek, N. B. Brauer, W. J. Buma, and M. Drabbels, J. Am. Chem. Soc. **132**, 14086 (2010).
[21] X. Zhang and M. Drabbels, J. Chem. Phys. **137**, 051102 (2012).
[22] X. Zhang, N. B. Brauer, G. Berden, A. M. Rijs, and M. Drabbels, J. Chem. Phys. **136**, 044305 (2012).
[23] R. J. Donnelly, J. A. Donnelly, and R. N. Hills, J. Low Temp. Phys. **44**, 471 (1981).
[24] R. J. Donnelly, *Quantized Vortices in Helium II* (Cambridge University Press, Cambridge, 1991).
[25] M. Weissbluth, *Atoms and molecules* (Academic Press, New York, 1980).
[26] M. Barranco, R. Guardiola, S. Hernández, R. Mayol, J. Navarro, and M. Pi, J. Low Temp. Phys. **142**, 1 (2006).
[27] F. Dalfovo, A. Lastri, L. Pricaupenko, S. Stringari, and J. Treiner, Phys. Rev. B **52**, 1193 (1995).
[28] L. Giacomazzi, F. Toigo, and F. Ancilotto, Phys. Rev. B **67**, 104501 (2003).
[29] N. F. Aguirre, D. Mateo, A. O. Mitrushchenkov, M. Pi, and M. P. de Lara-Castells, J. Chem. Phys. **136**, 124703 (2012).
[30] J. Eloranta and A. Apkarian, J. Chem. Phys. **117**, 10139 (2002).
[31] L. Lehtovaara, T. Kiljunen, and J. Eloranta, J. Comput. Phys. **194**, 78 (2004)
[32] D. Mateo, M. Barranco, and M. Pi, Phys. Rev. B **81**, 174510 (2010).
[33] D. Mateo, D. Jin, M. Barranco, and M. Pi, J. Chem. Phys. **134**, 044507 (2011).
[34] F. Cargnoni, T. Kuś, M. Mella, and R. J. Bartlett, J. Chem. Phys. **129**, 204307 (2008).
[35] A, Hernando, R. Mayol, M. Pi, M. Barranco, F. Ancilotto, O. Bünermann, and F. Stienkemeier, J. Phys. Chem. A **111**, 7303 (2007).
[36] A. Hernando, M. Barranco, R. Mayol, M. Pi, and F. Ancilotto, Phys. Rev. B **78**, 184515 (2008)
[37] The radius of the droplet is usually defined as that at which the density is half its saturation value. The expression used here complies with this definition only for large enough droplets where the local perturbation caused by the impurity is negligible in the outer region of the droplet.
[38] G. G. Nancolas, T. Ellis, P. V. E. McClintock, and R. M. Bowley, Nature **316**, 797 (1985).
[39] A. Hernando, M. Barranco, R. Mayol, M. Pi, and M. Kros-

nicki, Phys. Rev. B **77**, 024513 (2008).
[40] D. Mateo, A. Hernando, M. Barranco, R. Mayol, and M. Pi, Phys. Rev. B **83**, 174505 (2011).
[41] A. Ralston and H. S. Wilf, *Mathematical methods for digital computers* (John Wiley and Sons, New York, 1960).
[42] See supplementary material at `http://www.ecm.ub.es/famn/share/quantum_liquids/helium4/Ag/` for the continuous movies corresponding to Figs. 6-7 and 9-10 and other results.
[43] D. M. Brink and S. Stringari, Z. Phys. D **15**, 257 (1990).
[44] J. Harms, M. Hartmann, J. P. Toennies, A. F. Vilesov, and B. Sartakov, J. Mol. Spectrosc. **185**, 204 (1997).
[45] F. Ancilotto, M. Barranco, and M. Pi, Phys. Rev. B **82**, 014517 (2010).
[46] D. Jin and W. Guo, Phys. Rev. B **82**, 094524 (2010)
[47] Notice that the time elapsed between the first two frames in Fig. 6 is 8 ps, whereas the dynamics of Na was followed in Ref. 4 for just 5 ps.
[48] D. Mateo, M. Barranco, and J. Navarro, Phys. Rev. B **82**, 134529 (2010).
[49] Z. J. Jakubek, Q. Hui, and M. Takami, Phys. Rev. Lett. **79**, 629 (1997).
[50] The He-Ba^+ pair potential has been calculated at the CCSD(T) level of theory[10] using the same basis set as in Z. J. Jakubek and M. Takami, Chem. Phys. Lett. **265**, 653 (1997).
[51] E. Loginov and M. Drabbels, Phys. Rev. Lett. **106**, 083401 (2011).
[52] E. Loginov, D. Rossi, and M. Drabbels, Phys. Rev. Lett. **95**, 163401 (2005).
[53] F. Ancilotto, M. Barranco, F. Caupin, R. Mayol, and M. Pi, Phys. Rev. B **72**, 214522 (2005)
[54] F. Ancilotto, M. Pi, R. Mayol, M. Barranco, and K. K. Lehmann, J. Phys. Chem. A **111**, 12695 (2007)
[55] B. Tabbert, H. Günther, and G. zu Putlitz, J. Low Temp. Phys. **109**, 653 (1997).
[56] Y. Moriwaki and N. Morita, Eur. Phys. J. D **13**, 11 (2001).
[57] Y. Moriwaki, K. Inui, K. Kobayashi, F. Matsushima, and N. Morita, J. Mol. Struct. **786**, 112 (2006).
[58] S. Stringari and J. Treiner, Phys. Rev. B **36**, 16 (1987); J. Chem. Phys. **87**, 5021 (1987).
[59] V. Grau, M. Barranco, R. Mayol, and M. Pi, Phys. Rev. B **73**, 064502 (2006).

Chapter 4

Summary and Conclusions

This thesis presents a collection of four papers published in peer-reviewed scientific journals plus a manuscript yet to be submitted, all of them in the field of low temperature physics and quantum fluids. Each of these works reports a step forward in the ever-developing theoretical description of helium systems by means of density functional theory.

The first two papers [11, 12] are labelled as "structure" and deal with questions related to the groundstate description of helium complexes around atomic impurities. We have computed such structure and determined its effect on the dipole absorption spectrum of Na in ^{3}He–^{4}He clusters and of Mg in the homogeneous, isotopically mixed liquid. For the case of Na in clusters we have found that even though a large amount of ^{3}He is needed for the density in the outer shell of the mixed droplet to reach the bulk liquid ^{3}He value, the spectrum of the impurity is very insensitive to the isotopic composition and it rapidly saturates to the value of pure ^{3}He droplets when the quantity of ^{3}He is increased. For Mg in the mixed liquid, the presence of ^{3}He in the liquid induces shifts in the spectrum much smaller than its typical width so we have found the spectroscopic effect of the isotopic composition to be minor.

We have also explored the limits of density functional calculations for a small number of helium atoms interacting with a linear carbonyl sulfide (OCS) molecule. To this end we have implemented a Kohn-Sham scheme for ^{3}He and computed the structure of OCS@^{3}He$_N$ clusters for N up to to 40. We have compared the results for ^{4}He clusters with the same N value and found that the high anisotropy of the OCS molecule magnifies the effect of the different statistics of each isotope. Our estimate of the moments of inertia for these clusters is consistent with the interpretation of experimental data[13] suggesting an 11 atoms shell structure rigidly rotating with the OCS molecule.

The next three papers [10, 14, 15], labelled as "dynamics", deal with the real-time description of dynamical processes in helium systems of experimental interest. While the publications on statics are a steady completion of a well established line of work, the papers of this section open a new front for theoretical exploration of dynamical processes with picosecond resolution. We present an efficient and quantitatively accurate

procedure to compute the dynamics of an excited electron bubble and of an excited silver impurity, following a time-dependent density functional theory (TDDFT) approach for helium coupled to the appropiate dynamics for the impurity. The "appropiate" dynamics depends on the properties of the impurity: for the 1P electron bubble one can use a purely quantum mechanical description of the electron within an adiabatic approximation, whereas for the 2P bubble the adiabatic approximation must be lifted. For a heavy impurity such as Ag a classical description of its motion is enough, but its spin-orbit strength is large enough for the electronic state of the atom to be taken into account as a quantized degree of freedom. Our work shows that the use of TDDFT provides a good compromise between quantitative accuracy and computational efficiency, allowing to carry on the dynamical evolution of drops with thousand He atoms for hundred picoseconds.

In the case of the electron bubble, we have related the experimental disappearance of 1P bubbles at high pressures[9] with the existence of a nonradiative de-excitation path involving the bubble splitting about 20 picoseconds after the excitation. Our claim is sustained by the fact that our calculation predicts the splitting only for pressures above 1 bar, which is the same pressure threshold of the experimental disappearance. This agreement shows the remarkable accuracy of the calculations, as increasing the liquid pressure by 1 bar increases its density by a mere 1%. We have also found a marked change in the behavior of the time-resolved absorption spectrum of the 1P bubble depending on whether the bubble fissions or not, i.e., on the liquid pressure. This change is in principle an experimentally accessible observable whose determination may complement the information obtained from cavitation and photoconductivity experiments.

In the case of the desorption of a silver atom from a He drop, our dynamical calculations predict a range of velocities for the ejected impurity consistent with the experimental velocity distribution. This velocity is the result of how much energy is transferred from the impurity to the droplet, which depends on the accesible excitation modes. Our description of helium only allows for collective excitations such as density waves and surface oscilaltions, thus the agreement in the impurity velocity can be taken as indirect evidence of the superfluidity of helium nanodroplets. Besides, we have also ruled out vortex nucleation as a likely mode for energy transfer in such small drops doped with Ag. The huge structural changes in the surrounding liquid at the nanoscale induced by attractive impurities (neutral atoms or cations for instance) will render the development of any vorticity extremely difficult in such small systems. In this respect it is worth noting that ring vortex nucleation by attractive impurities moving in liquid helium has never been addressed by realistic methods.

In the course of our research we have developed and implemented several numerical tools, to mention a few: a Kohn-Sham implementation for ^{3}He clusters that fully takes into account the symmetries of the system while still using the power of Fast Fourier Transform techniques to compute convolution integrals,[12] the coupling of two wavefunctions evolving at very different time-scales through an adiabatic approach,[14]

the implementation of an efficient damping scheme to prevent bouncing waves from spoiling the calculation,[15] and the inclusion of a time-evolving electronic configuration (limited to the P manifold) of an impurity moving through helium.[10]

4.1 Outlook

There are dynamical processes in doped helium systems at the picosecond scale where the methodology presented here could be applied after some further developments are introduced. Situations where highly-localized structures appear –such as exciplexes[31] or snowballs[32]– are particularly challenging as they push the TDDFT formalism to its limits of application. How many atoms conform the snowball around an ion? When and how does the exciplex appear? How long does it take to form these structures? These are examples of open questions calling for improvements in the present implementation of TDDFT. It is worth mentioning the existence of methods to handle solid-like configurations within DFT,[33] and test particle-like methods[34] that could be tried in dynamical situations involving these very localized structures. Work along these lines is in progress in the group.

Appendix A

List of publications

2009

- *Spectrum of a* ^{3}He *atom in a* Ca@^{4}He$_{50}$ *droplet.* David Mateo, Manuel Barranco, Ricardo Mayol, Jesús Navarro, and Martí Pi. J. Phys.: Conf. Ser. **150**, 032051 (2009)
- Ca *impurity in small mixed* ^{3}He–^{4}He *clusters.* Rafael Guardiola, Jesús Navarro, David Mateo, and Manuel Barranco. J. Chem. Phys. **131**, 174110 (2009)
- *Solvation onset of* Ca *in mixed helium droplets.* David Mateo, Manuel Barranco, Ricardo Mayol, and Martí Pi. Eur. Phys. J. D **52**, 63 (2009)

2010

- *Evolution of the excited electron bubble in liquid* ^{4}He *and the appearance of fission-like processes.* David Mateo, Martí Pi, and Manuel Barranco. Phys. Rev. B **81**, 174510 (2010)
- *Elementary excitations in superfluid* ^{3}He–^{4}He *mixtures.* David Mateo, Manuel Barranco, and Jesús Navarro. Phys. Rev. B **82**, 134529 (2010)
- *Infrared Absorption and Emission Spectrum of Electron Bubbles Attached to Linear Vortices in Liquid* ^{4}He. David Mateo, Alberto Hernando, Manuel Barranco, and Martí Pi. J. Low Temp. Phys. **158**, 397 (2010)

2011

- *Absorption spectrum of atomic impurities in isotopic mixtures of liquid helium.* David Mateo, Alberto Hernando, Manuel Barranco, Ricardo Mayol, and Martí Pi. Phys. Rev. B **83**, 174505 (2011)
- *Excited electron-bubble states in superfluid* ^{4}He*: A time-dependent density functional approach.* David Mateo, Dafei Jin, Manuel Barranco, and Martí Pi. J. Chem. Phys. **134**, 044507 (2011)

2012

- Mg *impurity in helium droplets.* Jesús Navarro, David Mateo, Manuel Barranco, and Antonio Sarsa. J. Chem. Phys. **136**, 054301 (2012)

- *Helium mediated deposition: Modeling the* He−TiO_2(110)-(1×1) *interaction potential and application to the collision of a helium droplet from density functional calculations.* Néstor F. Aguirre, David Mateo, Alexander O. Mitrushchenkov, Martí Pi, and María Pilar de Lara-Castells. J. Chem. Phys. **136**, 124703 (2012)

- *Theoretical modeling of ion mobility in superfluid* ^{4}He. Steven L. Fiedler, David Mateo, Tatevik Aleksanyan, and Jussi Eloranta. Phys. Rev. B **86**, 144522 (2012)

2013

- *A density functional study of the structure of small* OCS@^{3}He$_N$ *clusters.* David Mateo, Martí Pi, Jesús Navarro, and J. Peter Toennies. J. Chem. Phys. **138**, 044321 (2013)

- *Electron Photo-ejection from Bubble States in Liquid* ^{4}He. Julián Barragán, David Mateo, Martí Pi, Francesc Salvat, Manuel Barranco, and Humphrey J. Maris. J. Low Temp. Phys. DOI: 10.1007/s10909-012-0730-4 (2013)

In progress

- *Existence of a critical Landau velocity in finite size helium systems*, Nils B. Brauer, Szymon Smolarek, Evgeniy Loginov, David Mateo, Alberto Hernando, Martí Pi, Manuel Barranco, Wybren J. Buma, and Marcel Drabbels. To be submitted (2013).

- *Translational dynamics of photoexcited atoms in* ^{4}He *nanodroplets: The case of silver*, David Mateo, Alberto Hernando, Manuel Barranco, Evgeniy Loginov, Marcel Drabbels, and Martí Pi. To be submitted (2013).

Bibliography

[1] Pitaevskii, L. and Stringari, S. *Bose-Einstein Condensation*, volume 116 of *International Series of Monographs on Physics*. Claredon Press, (2003).

[2] Toennies, J. P. and Vilesov, A. F. *Angewandte Chemie International Edition* **43**(20), 2622–2648 (2004).

[3] Stienkemeier, F. and Lehmann, K. K. *Journal of Physics B: Atomic, Molecular and Optical Physics* **39**(8), R127 (2006).

[4] Barranco, M., Guardiola, R., Hernández, S., Mayol, R., Navarro, J., and Pi, M. *Journal of Low Temperature Physics* **142**, 1–81 (2006).

[5] Tiggesbaumker, J. and Stienkemeier, F. *Phys. Chem. Chem. Phys.* **9**, 4748–4770 (2007).

[6] Choi, M. Y., Douberly, G. E., Falconer, T. M., Lewis, W. K., Lindsay, C. M., Merritt, J. M., Stiles, P. L., and Miller, R. E. *International Reviews in Physical Chemistry* **25**(1-2), 15–75 (2006).

[7] Szalewicz, K. *International Reviews in Physical Chemistry* **27**(2), 273–316 (2008).

[8] Ancilotto, F., Cheng, E., Cole, M., and Toigo, F. *Zeitschrift für Physik B Condensed Matter* **98**, 323–329 (1995).

[9] Maris, H. J., Ghosh, A., Konstantinov, D., and Hirsch, M. *J. Low Temp. Physics* **134**, 227 (2004).

[10] Mateo, D., Hernando, A., Barranco, M., Loginov, E., Drabbels, M., and Pi, M. to be submitted, (2013).

[11] Mateo, D., Hernando, A., Barranco, M., Mayol, R., and Pi, M. *Phys. Rev. B* **83**, 174505 May (2011).

[12] Mateo, D., Pi, M., Navarro, J., and Toennies, J. P. *The Journal of Chemical Physics* **138**(4), 044321 (2013).

[13] Sartakov, B. G., Toennies, J. P., and Vilesov, A. F. *The Journal of Chemical Physics* **136**(13), 134316 (2012).

[14] Mateo, D., Pi, M., and Barranco, M. *Phys. Rev. B* **81**, 174510 May (2010).

[15] Mateo, D., Jin, D., Barranco, M., and Pi, M. *The Journal of Chemical Physics* **134**(4), 044507 (2011).

[16] van Delft, D. *Physics Today* **61**(3), 36–42 (2008).

[17] Leggett, A. J. *Rev. Mod. Phys.* **47**, 331–414 Apr (1975).

[18] Krotscheck, E. *Microscopic Quantum Many-Body Theories and their applications*, volume 510 of *Lecture Notes in Physics*, 187–250. Springer (1998).

[19] Boronat, J. *Microscopic Approaches to Quantum Liquids in Confined Geometries*, volume 4 of *Series on Advances in Quantum Many-Body Theory*, chapter 2, 21–86. World Scientific (2002).

[20] Saarela, M., Apaja, V., and Halinen, J. *Microscopic Approaches to Quantum Liquids in Confined Geometries*, volume 4 of *Series on Advances in Quantum Many-Body Theory*, chapter 4, 129–193. World Scientific (2002).

[21] Apaja, V. and Krotscheck, E. *Microscopic Approaches to Quantum Liquids in Confined Geometries*, volume 4 of *Series on Advances in Quantum Many-Body Theory*, chapter 5, 197–258. World Scientific (2002).

[22] Bishop, R. F. *Microscopic Quantum Many-Body Theories and their applications*, volume 510 of *Lecture Notes in Physics*, 1–70. Springer (1998).

[23] Padmore, T. C. and Cole, M. W. *Phys. Rev. A* **9**, 802–807 Feb (1974).

[24] Ebner, C. and Saam, W. F. *Phys. Rev. B* **12**, 923–939 Aug (1975).

[25] Kohn, W. and Sham, L. J. *Phys. Rev.* **140**, A1133–A1138 Nov (1965).

[26] Hernández, E. S. and Navarro, J. *Microscopic Approaches to Quantum Liquids in Confined Geometries*, volume 4 of *Series on Advances in Quantum Many-Body Theory*, chapter 6, 261–312. World Scientific (2002).

[27] Hohenberg, P. and Kohn, W. *Phys. Rev.* **136**, B864–B871 Nov (1964).

[28] Dalfovo, F., Lastri, A., Pricaupenko, L., Stringari, S., and Treiner, J. *Phys. Rev. B* **52**, 1193–1209 Jul (1995).

[29] Barranco, M., Pi, M., Gatica, S. M., Hernández, E. S., and Navarro, J. *Phys. Rev. B* **56**, 8997–9003 Oct (1997).

[30] Ralston, A. and Wilf, H. S. *Mathematical methods for digital computers*, volume 1, 95–120. John Wiley and Sons (1960).

[31] Loginov, E. and Drabbels, M. *The Journal of Physical Chemistry A* **111**(31), 7504–7515 (2007). PMID: 17569515.

[32] Muller, S., Mudrich, M., and Stienkemeier, F. *The Journal of Chemical Physics* **131**(4), 044319 (2009).

[33] Ancilotto, F., Barranco, M., Caupin, F., Mayol, R., and Pi, M. *Phys. Rev. B* **72**, 214522 Dec (2005).

[34] Hernando, A., Barranco, M., Pi, M., Loginov, E., Langlet, M., and Drabbels, M. *Phys. Chem. Chem. Phys.* **14**, 3996–4010 (2012).